

Wavelet based OFDM with V-BLAST Virtual MIMO for
Wireless Multimedia Sensor Networks

Zimran Rafique

A thesis submitted to
Auckland University of Technology
in fulfilment of the requirements for the degree of
Doctor of Philosophy (Ph.D.)

2014

School of Engineering

DECLARATION

I declare that this thesis is my own work and has not been submitted in any form for any degree or diploma at any other university. Information derived from published or unpublished work of others has been acknowledged in the text and a list of references is given.



Zimran Rafique

November, 2014

ACKNOWLEDGEMENT

I am grateful to Almighty Allah for His guidance and infinite blessings to complete this intricate task. The research work presented in this thesis was carried out under the supervision of Dr. Boon-Chong Seet. His valuable and priceless guidance made it possible to finish this job. I would like to express my heartiest gratitude to Dr. Boon-Chong Seet for his keen interest and technical support throughout my study period. I would also like to thank my co-supervisor Professor Dr. Adnan Al-Anbuky for his very useful guidance during my research work.

I would express deepest gratitude to my parents for their supportive and valiant role in every affair of my life. Balmy gratitude goes to my spouse who always takes care of my needs and whenever I got anxious during my work, she enhanced my guts. Modest recognition goes to my brothers and sisters for all their prayers and concerns about my study and tough time during my student life.

I would also thank to my colleagues for their technical and moral support.

TABLE OF CONTENTS

CHAPTER 1.....	1
1: INTRODUCTION	1
1.1 Motivation and Scope of Research	2
1.2 Contributions.....	3
1.3 Thesis Organisation	4
CHAPTER 2.....	6
2: BACKGROUND.....	6
2.1 Wireless Sensor Networks	6
2.1.1 Multimedia Communication in WSNs	8
2.2 MIMO Techniques	9
2.2.1 True MIMO Architecture.....	10
2.2.2 Virtual MIMO Architecture	10
2.2.3 V-BLAST System	13
2.3 OFDM.....	15
2.3.1 OFDM and Orthogonality Principle	15
2.3.2 Fourier based OFDM (FOFDM)	17
2.3.3 Wavelet based OFDM (WOFDM)	18
2.3.3.1 Quadrature Mirror Filters (QMF)	19
A. Basic Definitions.....	19
A.1 UpSampling	19
A.2 DownSampling.....	21
A.3 ReSampling.....	21
A.4 Interpolation	22
A.5 Decimation.....	24
B. Two-Channel Multirate Filter Bank	25
B.1 Perfect Reconstruction Quadrature Mirror Filters (PR-QMF).....	28
B.2 Delay Free Perfect Reconstruction Quadrature Mirror Filters (PR-QMF)	29
C. Multilevel Filter Banks.....	31
C.1 Symmetric Synthesis Filter Bank.....	31
C.2 Symmetric Analysis Filter Bank.....	32
C.3 Asymmetric Synthesis Filter Bank.....	34
C.4 Asymmetric Analysis Filter Bank.....	35
CHAPTER 3.....	37
3: REVIEW OF THE STATE OF THE ART.....	37
3.1 Multiple Antenna Systems	37
3.1.1 Spatial Multiplexing Techniques.....	39
3.1.1.1 D-BLAST.....	40
3.1.1.2 V-BLAST.....	42
A. Detection Algorithms	43
A.1 Zero-Forcing Detection Algorithm.....	43
A.2 MMSE Detection Algorithm.....	45
A.3 QR Decomposition Detection Algorithm.....	45
3.1.1.3 Turbo-BLAST	46
3.1.2 Space-Time Coding (STC) Techniques	48
3.1.2.1 Alamouti Space-Time Coding Technique	49
3.1.2.2 Space-Time Trellis Coding (STTC) Technique	50
3.1.2.3 Orthogonal Space-Time Block Coding (OSTBC) Technique.....	52

3.1.2.4 Space-Time Vector Coding (STVC) Technique	53
3.1.3 Beam-Forming.....	55
3.1.4 Multi-Functional MIMO Systems	57
3.1.5 Virtual MIMO Systems	58
3.1.6 MIMO Techniques for WSNs.....	58
3.2 FOFDM and MIMO-FOFDM	59
3.2.1 FOFDM.....	59
3.2.2 MIMO-FOFDM	61
3.3 WOFDM and MIMO-WOFDM	64
3.3.1 WOFDM.....	64
3.3.2 MIMO-WOFDM.....	67
CHAPTER 4.....	69
4: VIRTUAL MIMO WSN	69
4.1 True MIMO DGN.....	69
4.1.1 System Model	69
4.1.2 Energy Consumption Analysis.....	71
4.1.2.1 RF (Analogue) Energy Consumption.....	71
4.1.2.2 Base Band (Digital) Energy Consumption	75
4.1.3 Spectral Efficiency	76
4.1.4 Time Delay	76
4.2 Virtual MIMO DGN.....	78
4.2.1 System Model	78
4.2.2 Energy Consumption Analysis.....	80
4.2.2.1 RF (Analogue) Energy Consumption.....	80
4.2.2.2 Base Band (Digital) Energy Consumption	82
4.2.3 Spectral Efficiency	82
4.2.4 Time Delay	83
4.3 Evaluation Results	84
CHAPTER 5.....	97
5: MIMO CHANNEL EQUALISATION	97
5.1 MIMO Channel Equalisation with QMF Bank Architecture.....	98
5.2. Evaluation Results	102
CHAPTER 6.....	111
6: PHASE OFFSET COMPENSATION	111
6.1 System Model.....	112
6.2 Phase Offset Compensation.....	115
6.3 Evaluation Results	117
CHAPTER 7.....	123
7: CONCLUSION AND FUTURE WORK	123
7.1 Conclusion	123
7.2 Future Work	125
REFERENCES	127
APPENDIX	136
A.1 Genetic Algorithm	136
A.2 Genetic Algorithm Matlab Solver.....	137

LIST OF FIGURES

Figure 2.1: Wireless Sensor Network	6
Figure 2.2: A Flood Monitoring System	7
Figure 2.3: Wireless Multimedia Sensor Network	8
Figure 2.4: A WMSN with its application in battle field [19]	9
Figure 2.5: MIMO wireless communication system	10
Figure 2.6: Virtual-MIMO system models	12
Figure 2.7: V-BLAST system with N_t transmitting and N_r receiving antennas	14
Figure 2.8: Comparison of the bandwidth utilisation for FDM and OFDM	16
Figure 2.9: A basic FOFDM based communication system	17
Figure 2.10: Complex values for the waveform samples of FOFDM and WOFDM	18
Figure 2.11: UpSampling	20
Figure 2.12: Spectrum of the Signal before & after Up Sampling	20
Figure 2.13: DownSampling	21
Figure 2.14: Spectrum of the Signal before & after DownSampling	22
Figure 2.15: Interpolation	23
Figure 2.16: Magnitude Response of Interpolated Signal ($L=2$) at Different Stages	23
Figure 2.17: Decimation	24
Figure 2.18: Magnitude Response of Decimated Signal ($M = 2$) at Different Stages	25
Figure 2.19: Two-Channel QMF Filter Bank	26
Figure 2.20: Low pass and High pass Analysis Filters Frequency Response using Haar Coefficients	27
Figure 2.21: Symmetric Synthesis Two Level Filter Bank	31
Figure 2.22: Equivalent Structure of Symmetric Synthesis Two Level Filter Bank using Noble Identities	32
Figure 2.23: Symmetric Analysis Two Level Filter Bank	33
Figure 2.24: Equivalent Structure of Symmetric Analysis Two Level Filter Bank using Noble Identities	33
Figure 2.25: Asymmetric Synthesis Two Level Filter Bank	34
Figure 2.26: Equivalent Structure of Asymmetric Synthesis Two Level Filter Bank using Noble Identities	35
Figure 2.27: Asymmetric Analysis Two Level Filter Bank	36
Figure 2.28: Equivalent Structure of Asymmetric Synthesis Two Level Filter Bank using Noble Identities	36
Figure 3.1: Spatial multiplexing system architecture with N_t transmitting and N_r receiving antennas	39
Figure 3.2: Space-time coding system architecture with N_t transmitting and N_r receiving antennas	48
Figure 3.3: 4-PSK 4-state space-time code with two transmitting antennas	51
Figure 3.4: A beam-former with N_t transmitting and N_r receiving antennas	55
Figure 3.5: A simple delay-sum beamformer	55
Figure 3.6: V-BLAST MIMO system with beamformer	56
Figure 3.7: Multi-functional MIMO system	57
Figure 3.8: FOFDM modulator and demodulator with filter bank structure	60
Figure 3.9: Co-operative communication in a multi user scenario using FOFDM	61
Figure 3.10: MIMO-FOFDM system with N_t transmitting and N_r receiving antennas	62
Figure 3.11: WOFDM modulator and demodulator using symmetric QMF filter bank structure	66
Figure 3.12: Equivalent structure of WOFDM modulator and demodulator using noble identities	67
Figure 3.13: MIMO-WOFDM system with N_t transmitting and N_r receiving antennas	68
Figure 4.1: Communication between DSNs (Virtual MIMO node) and DGN	70
Figure 4.2: Transmitter and receiver architecture for ASK-WOFDM and BPSK-WOFDM	73
Figure 4.3: Transmitter and receiver architecture (In-Phase/Quadrature-Phase) for ASK-FOFDM, BPSK-FOFDM, QAM, DPSK, and OPSK (analogue)	75
Figure 4.4: Communication between Transmitting and Receiving Side Virtual MIMO Nodes	78
Figure 4.5: BER performance over transmission distance of 20 m with True MIMO DGN Architecture	86

Figure 4.6: BER performance over transmission distance of 20 m with Virtual MIMO DGN Architecture	87
Figure 4.7: Total energy per bit per antenna over transmission distance of 1 to 100 m with True MIMO DGN Architecture	89
Figure 4.8: Total energy per bit per antenna over transmission distance of 1 to 100 m with Virtual MIMO DGN Architecture	89
Figure 4.9: Energy Efficiency versus Spectral Efficiency for True MIMO DGN Architecture	96
Figure 4.10: Energy Efficiency versus Spectral Efficiency for Virtual MIMO DGN Architecture.....	96
Figure 5.1: MIMO Channel Equalisation Block.....	99
Figure 5.2: Filter Bank Structure (F_U)	100
Figure 5.3: Filter Bank Structure (F_V)	101
Figure 5.4: BER performance over transmission distance of 20 m with True MIMO DGN using QR and QMF Bank detection process	103
Figure 5.5: BER performance over transmission distance of 20 m with Virtual MIMO DGN using QR and QMF Bank detection process	103
Figure 5.6: Total energy per bit per antenna over transmission distance of 1 to 100 m with True MIMO DGN using QR and QMF Bank detection process	104
Figure 5.7: Total energy per bit per antenna over transmission distance of 1 to 100 m with Virtual MIMO DGN using QR and QMF Bank detection process	105
Figure 5.8: Energy Efficiency versus Spectral Efficiency over transmission distance of 20 m with True MIMO DGN using QR and QMF Bank detection process	109
Figure 5.9: Energy Efficiency versus Spectral Efficiency BER over transmission distance of 20 m with Virtual MIMO DGN using QR and QMF Bank detection process	109
Figure 6.1: Communication between transmitting side and receiving side Virtual MIMO nodes.....	113
Figure 6.2: DSN and DGN architectures	114
Figure 6.3: BER performance of BPSK-16FOFDM over transmission distance of $d = 20$ m in the presence of phase offset with Virtual MIMO DGN Architecture using QR detection process	118
Figure 6.4: BER performance of BPSK-16WOFDM over transmission distance of $d = 20$ m with Haar and Optimised Wavelets in the presence of phase offset with Virtual MIMO DGN Architecture using QR detection process	118
Figure 6.5: BER performance of BPSK-16WOFDM over transmission distance of $d = 20$ m with Haar and Optimised Wavelets in the presence of phase offset with Virtual MIMO DGN Architecture using QMF bank detection process	119
Figure 6.6: Polar Plots for BPSK-16FOFDM	120
Figure 6.7: Polar Plots for BPSK-16WOFDM.....	121
Figure A.1: GA process	136

LIST OF TABLES

Table 3.1: Time-delay diversity with 2 antennas.....	51
Table 4.1: Base Band (Digital) Energy Consumption with True MIMO DGN Architecture	90
Table 4.2: Base Band (Digital) Energy Consumption with Virtual MIMO DGN Architecture	91
Table 4.3: RF (Analogue) Energy Consumption and Total Energy Consumption with True MIMO DGN Architecture..	93
Table 4.4: RF (Analogue) Energy Consumption and Total Energy Consumption with Virtual MIMO DGN Architecture	93
Table 4.5: Total Time Delay for True MIMO DGN Architecture	94
Table 4.6: Total Time Delay for Virtual MIMO DGN Architecture	94
Table 5.1: Base Band (Digital) Energy Consumption with True MIMO DGN Architecture	106
Table 5.2: Base Band (Digital) Energy Consumption with Virtual MIMO DGN Architecture	106
Table 5.3: RF (Analogue) Energy Consumption and Total Energy Consumption with True MIMO DGN Architecture	107
Table 5.4: RF (Analogue) Energy Consumption and Total Energy Consumption with Virtual MIMO DGN Architecture	107
Table 5.5: Total Time Delay for True MIMO DGN Architecture	108
Table 5.6: Total Time Delay for Virtual MIMO DGN Architecture	108

ABSTRACT

Wireless sensor networks (WSNs) are finding their place in many real life applications because low power and small-size sensor nodes can be inexpensively and easily deployed in the areas of interest for different applications. Wireless multimedia sensor networks (WMSNs) consist of wireless nodes capable of producing multimedia (image/video) data streams that will enable a new generation of WSN applications. The transmission of multimedia content involves high volume data communication that may require significant bandwidth and energy resources. Hence, supporting high data rate while maintaining energy efficiency is a key challenge of WMSNs.

Multi-Input Multi-Output (MIMO) techniques can be used to increase the data rate for a given bit error rate (BER) and transmission power. Due to the small form factor, energy and processing constraints of WSN nodes, sometimes it is not feasible to equip the nodes with multiple antennas. Virtual MIMO as opposed to True MIMO system architecture is considered more feasible for WSN applications. In this thesis, we analyse the performance of WSN with Virtual MIMO system architecture at transmitter side, and True or Virtual MIMO system architecture using Vertical Bell Laboratories Layered Space Time (V-BLAST) signal processing technique at receiver side. We investigated for the first time, the impact of different modulation techniques on the performance of a Virtual MIMO system based on V-BLAST architecture with multi-carrier modulation techniques in the context of WMSNs. Through analytical models and simulations using real hardware and environment settings, both communication and processing energy consumptions, BER, spectral efficiency, and total time delay performances have been analysed. The results show that Virtual MIMO system with Binary Phase Shift Keying-Wavelet based Orthogonal

Frequency Division Multiplexing (BPSK-WOFDM) modulation is a promising solution for future high data-rate and energy-efficient WMSNs.

This research also proposes a new channel equalisation technique which uses Quadrature Mirror Filter (QMF) bank architecture that is also found in WOFDM modulator and demodulator. The proposed technique is found to perform better in terms of BER, energy efficiency, and total time delay as compared to QR detection process.

In this thesis, we also present a novel method to mitigate the problem of phase offset, which is a major issue affecting the performance of Virtual MIMO systems. We optimise the wavelet bases of BPSK-WOFDM technique using genetic algorithm (GA) to compensate for unwanted phase differences between sensor nodes in a Virtual MIMO WSN. Results show that the optimised BPSK-WOFDM technique can effectively mitigate the phase offset issue.

Chapter 1

Introduction

A WSN is a network of sensor nodes each of these equipped with a wireless transceiver and is usually powered by an exhaustible energy source such as a battery. The sensor nodes are deployed in an outdoor or indoor environment to be monitored. WSNs are being used in many real life applications such as environmental (temperature, humidity, light) monitoring, home automation, traffic control, precision agriculture and health care [1].

A WMSN consists of standard data sensors along with audio and video sensors to enhance existing WSN applications but they will also enable several new multimedia applications such as traffic avoidance, enforcement and control systems, advanced health care delivery, automated assistance for the elderly and family monitors, environmental monitoring, person locator services and industrial process control [2].

Multiple antenna systems are capable of achieving higher data rates and smaller BER with the same transmit power and bandwidth as required by single antenna systems [3]. MIMO schemes have good spectral efficiency but with more circuit complexity that consumes energy. In long distance transmission, circuit energy consumption is much less than transmission energy consumption, but in short distance transmission circuit energy consumption is comparable with transmission energy. MIMO techniques have been proposed for WSNs where mostly nodes operate on batteries and are expected to work for a long period of time. To

evaluate the performance of MIMO techniques in energy-limited WSNs, one must take into account of both the circuit and transmission power consumption [4].

Fourier based OFDM (FOFDM) is a multicarrier modulation technique which has the capability to mitigate the effect of inter-symbol-interference (ISI) at the receiver side [5]. Wavelet based OFDM (WOFDM) is another multicarrier modulation technique and its properties are being explored in the field of high data rate communication systems [6]. In this modulation technique, the orthogonal subcarriers are generated using symmetric/asymmetric multilevel QMF bank structure. A QMF bank is a multirate digital filter bank with interpolators and decimators [7]. WOFDM has been recently adopted by the new IEEE 1901 standard (IEEE Standard-1901, January, 2010) as one of the two physical layer modulation techniques for broadband over power line networks [8].

1.1 Motivation and Scope of Research

The scope of the research and solution approaches proposed in this thesis have been primarily motivated by the following observations:

- Power consumption and high bandwidth requirement are fundamental issues in WMSNs. For multimedia applications, more bandwidth and excessive signal processing is required for high data rate transmission and reception along with more power consumption for battery constrained multimedia sensor nodes.
- Due to the small form factor and limited energy of some wireless nodes, it is often not realistic to equip each node with multiple antennas to implement MIMO. Instead, a cluster of single-antenna nodes can cooperate to form a virtual antenna array (VAA) to achieve virtual MIMO communication. In virtual MIMO systems, nodes are physically located in different places within

the range, and thus phase, frequency and timing asynchronism can be a major problem for such systems.

- By using the properties of WOFDM such as one dimensional constellation, simpler radio frequency (RF) section can also be designed for energy-efficient and high data-rate WMSNs. WOFDM also has the strong advantage of being generic modulation technique whose characteristics can be tailored according to the communication system conditions and requirements unlike FOFDM where the bases are static sine/cosine signals.

1.2 Contributions

The research undertaken in this thesis has made the following three important contributions to advance the current state of the field:

- This thesis proposes BPSK-WOFDM as a primary modulation technique for WMSNs based on Virtual MIMO V-BLAST architecture. The BER, energy performance, spectral efficiency, time delay efficiency of BPSK-WOFDM is analysed and compared with other well-known modulation techniques by using the concept of VAA to form a cluster of sensor nodes on transmitting and receiving side for Virtual MIMO communication. Real hardware settings are also used to calculate baseband signal processing energy consumption and processing time delay of proposed models.

- MIMO channel has also been equalised by using QMF bank structure and the system performance parameters have been compared with QR-detection algorithm. This technique further enhances the performance of BPSK-WOFDM in term of BER and energy efficiency and time delay.
- The BER performance of Virtual MIMO systems in the presence of phase-offset using BPSK-FOFDM and BPSK-WOFDM has been compared. Phase-offset effect has also been minimised by optimising the wavelet bases using GA. The simulation results show Virtual MIMO systems perform better in the presence of phase-offset with optimised wavelet bases.

This thesis has resulted in the following list of publications:

1. Z. Rafique, and B.-C. Seet, “Energy efficient Wavelet based OFDM for V-BLAST MIMO Wireless Sensor Networks”, *IEEE Online Conference on Green Communication*, Oct., 2011.
2. Z. Rafique and B.-C.Seet, “Energy efficient MIMO-OFDM systems,” in *Handbook of Green Information and Communication Systems*, M.S. Obaidat, A. Anpalagan, and Isaac Woungang, Eds. Waltham,USA: Elsevier, pp. 393–419, Jan. 2013.
3. Z. Rafique, B.-C. Seet, and A. Al-anbuky, “Performance analysis of cooperative virtual MIMO system for WSNs”, *MDPI Sensors Journal*, vol. 16, no.3, pp. 7033–7052, 2013.

1.3 Thesis Organisation

The remaining of the thesis is organised as follows:

Chapter 2 discusses WSNs and WMSNs with their existing and future real life applications. This chapter also describes True and Virtual MIMO receiver architecture along with V-BLAST and basic concept of OFDM.

Chapter 3 gives the review of multi-antenna systems and also MIMO techniques usage for WSNs. This chapter also discusses FOFDM and WOFDM with single and multi-antenna systems.

Chapter 4 describes energy consumption, spectral efficiency, time delay with True and Virtual MIMO DGN architecture along with different modulation techniques.

Chapter 5 discusses MIMO channel equalisation. This chapter further describes MIMO channel equalisation with QMF bank structure using True and Virtual MIMO DGN architecture.

Chapter 6 provides the performance comparison of FOFDM and WOFDM with virtual MIMO in the presence of phase-offset. This chapter further discusses the phase-offset compensation with Wavelet based filter coefficients optimization using GA to minimise phase-offset effect for virtual MIMO systems.

Chapter 7 concludes the work and suggests some future directions of research.

Chapter 2

Background

2.1 Wireless Sensor Networks

In WSN, the sensor nodes sense the environment or event, process and transmit the data wirelessly to the data gathering node (DGN) usually called a sink. A sink is connected to another network such as internet through a gateway [9] as shown in Figure 2.1. A sensor node can be stationary or moveable with or without awareness of its physical location.

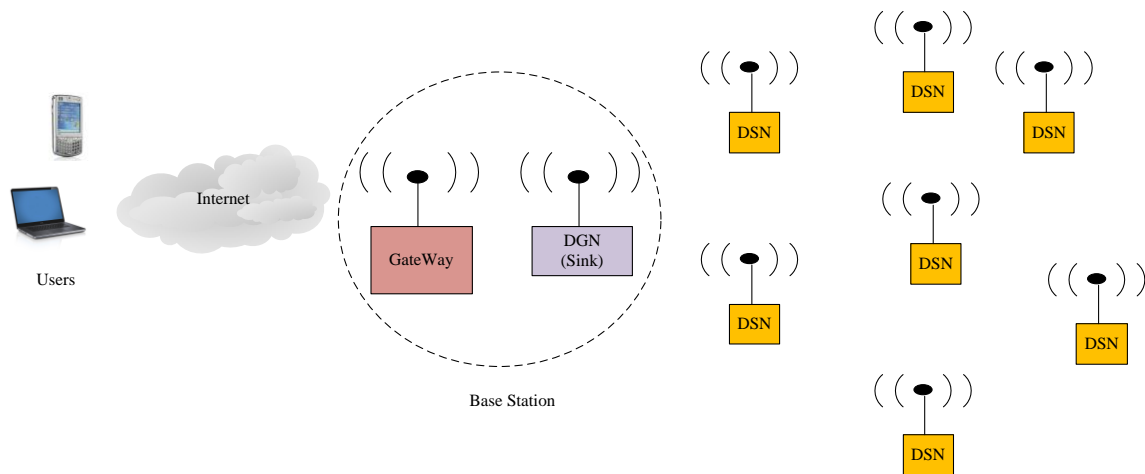


Figure 2.1: Wireless Sensor Network

Due to advancement in Micro-Electro-Mechanical Systems (MEMS) technology, low power, low cost sensor nodes can be deployed in the area of interest for various application [10, 11]. Most of the applications of WSNs can be divided into two main categories: event detection and

spatial process estimation. Some applications could be a combination of event detection and spatial process estimation [9].

The examples of event detection are bush/forest fires [12], flooding [13, 14] and earth quake [15]. In [13], a real time flood monitoring system was designed and implemented on an island that has 14 rivers. In each river, one WSN was installed which included two sensor nodes and one base station. A base station consists of a sink node and gateway [13]. The data from each river was transmitted to WSN disaster management server as shown in Figure 2.

A physical spatial process can also be estimated by deploying sensors to obtain samples for estimating spatial processes such as atmospheric pressure, ground temperature variations in volcanic sites [9], biological or chemical contaminating source identification [16]. Energy efficient buildings with WSNs have been proposed for event detection and spatial estimation process. The operating state of electrical appliances can be sensed and therefore their energy consumption can also be estimated as a spatial estimation process [17].

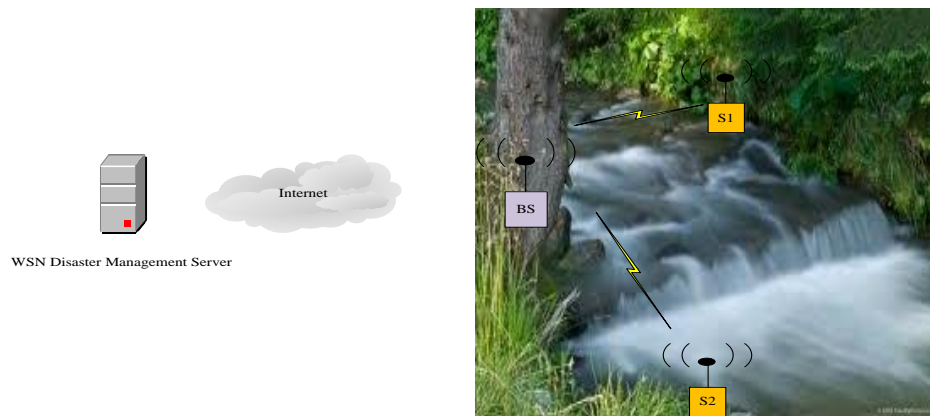


Figure 2.2: A Flood Monitoring System

2.1.1 Multimedia Communication in WSNs

A wireless network with sensor nodes capable of producing different media streams (audio, video, image, textual, and scalar sensor data) is usually referred to as a WMSN [17]. As shown in Figure 2.3, WMSNs are an emerging type of sensor networks which can facilitate

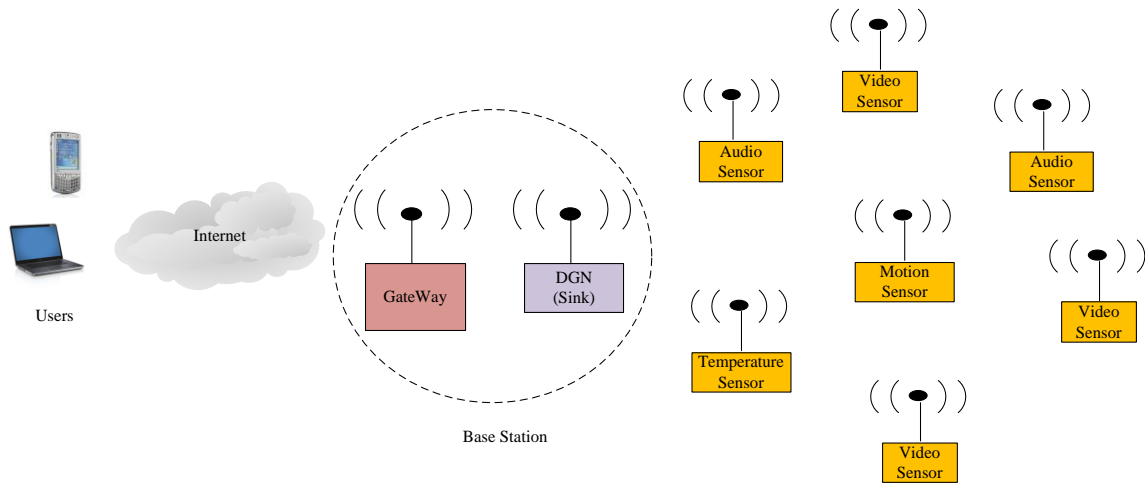


Figure 2.3: Wireless Multimedia Sensor Network

automated real-time interpretation of situations in the monitored environment. Potential applications of such sensor networks include country borders and public spaces surveillance, wildlife habitat and seismic monitoring, in-home emergency detection for the sick and elderly, health care, mixed reality networked gaming, and quality control of manufacturing processes [18]. An example of WMSN with its application in a battle field is shown in Figure 2.4 [19]. However, multimedia contents such as image or video streams require data rates that are orders of magnitude higher than what can be supported by current sensor networks. Embedded sensors are also constrained in terms of energy as they are typically battery-powered [20]. Thus, high data rates and high energy efficiency are key issues to be addressed in such networks.

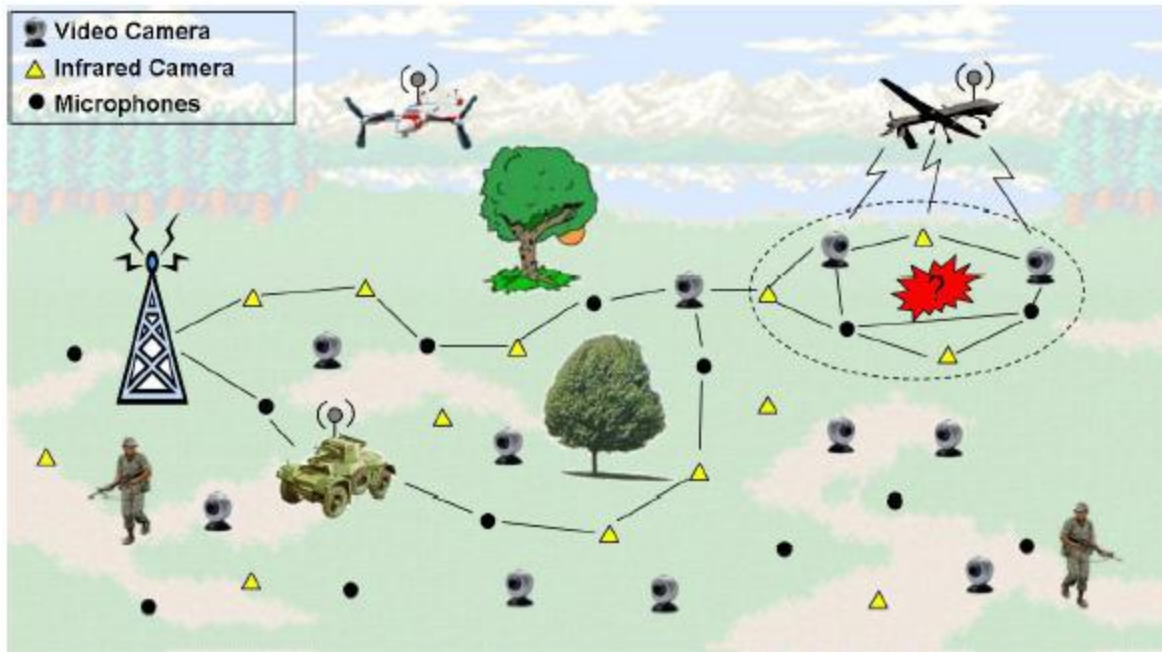


Figure 2.4: A WMSN with its application in battle field [19]

2.2 MIMO Techniques

In late 1990s, MIMO techniques were proposed to achieve higher data rates and smaller BER with the same transmit power and bandwidth required by single antenna systems [3]. In multiple antenna systems, more than one antennas are used on transmitting and/or receiving side as shown in Figure 2.5. MIMO techniques can be used to increase data rate using spatial multiplexing and BER can be improved by using spatial diversity. MIMO techniques can also be used to increase SNR at the receiver and to mitigate co-channel interference (CCI) along with beam forming techniques.

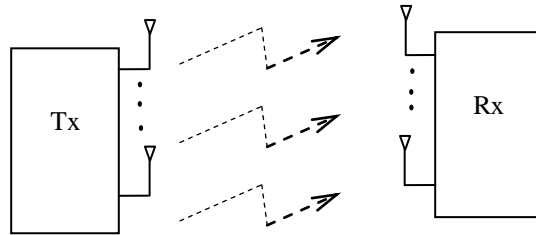


Figure 2.5: MIMO wireless communication system

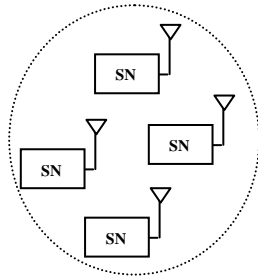
2.2.1 True MIMO Architecture

In true/co-located MIMO architecture, multiple antennas are connected to a single transmitter/receiver node as shown in Figure 2.5. This architecture can be used for space division multiplexing (SDM) as well as space time coding (STC). The signal processing can be done at transmitter or/and receiver side.

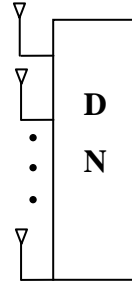
However, due to small form factor of some wireless nodes (e.g. mobile phones, sensor nodes), less energy availability, and the need to maintain a minimum distance among the antennas to avoid correlated fading in order to achieve independent fading, it can be difficult to realise the advantages of MIMO techniques for such wireless nodes [21].

2.2.2 Virtual MIMO Architecture

MIMO techniques are capable of providing high system performance without additional transmission power and bandwidth. However, sometimes it is not possible to equip nodes with multiple antennas. Hence, multiple nodes, each with single antenna can cooperate in a cluster to

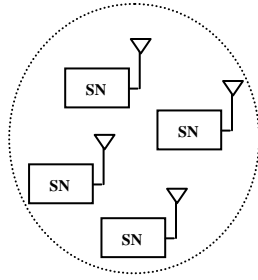


Transmitting side Virtual
MIMO with N_t SNs

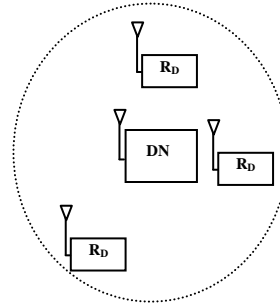


DN with N_r Antennas

(Model-a)

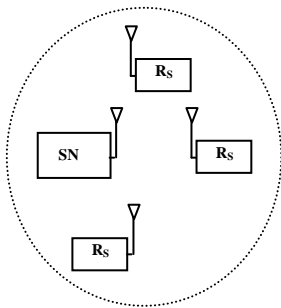


Transmitting side Virtual
MIMO with N_t SNs

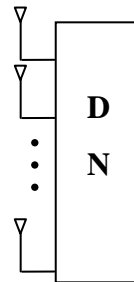


Receiving side Virtual MIMO with 1 DN and
 N_r-1 Relay Nodes (R_D)

(Model-b)



Transmitting side Virtual MIMO with 1 SN and
 N_t-1 Relay Nodes (R_s)



DN with N_r Antennas

(Model-c)

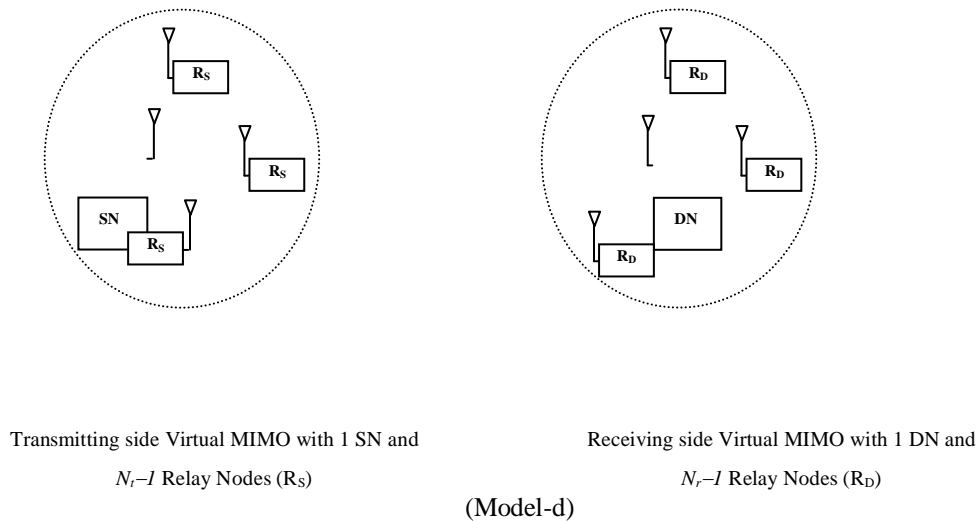


Figure 2.6: Virtual-MIMO system models

form one Virtual MIMO node that can offer some advantages of a true MIMO system. Thus, the concept of Virtual MIMO (also known as cooperative MIMO) can be used for energy and physically constrained wireless nodes [4]. In Figure 2.6, four different V-MIMO models are shown.

In *Model-a*, each source node is equipped with one antenna and transmitting data simultaneously without sharing any information among themselves. The destination node is equipped with multiple antennas with the assumption that it has no energy and physical dimension constraints.

In *Model-b*, there are N_t source nodes, one destination node, and $N_r - 1$ relay nodes (R_D) at destination side each with one antenna. The source nodes transmit their data simultaneously without any local communication and at the destination side, local communication is involved between destination node and the set of relay nodes. The transmission delay of *Model-b* is greater than transmission delay of *Model-a*.

In *Model-c*, there is one source node, $N_t - 1$ relay nodes (R_S) each with one antenna, and one destination node with N_r receiving antennas. The local communication is involved between source node and the set of relay nodes at transmitter side.

In *Model-d*, there is one source node, one destination node, the set of relay nodes (R_S) at transmitting (or sending) as well as destination side (R_D), and each node is with single antenna. The transmission delay of this model is greater than other models because local communication is involved at transmitter as well as receiver side.

2.2.3 V-BLAST System

BLAST stands for Bell Laboratories Layered Space Time, and V stands for Vertical which relates to the blocking structure [22]. V-BLAST is a wireless communication technique which uses multi-element antennas at both transmitter and receiver. It is a highly bandwidth efficient approach for wireless networks. Its spectral efficiency ranges from 20 to 40 bps/Hz [22] while that of traditional wireless communication techniques ranges from 1 to 5 bps/Hz (mobile cellular) to around 10 to 12 bps/Hz (point-to-point fixed microwave system).

In V-BLAST, a single user's data stream is split into multiple sub-streams or multiple users can transmit their data simultaneously. An array of transmitter antennas is used concurrently to launch the parallel sub-streams as shown in Figure 2.7. All the sub-streams are transmitted in the same frequency band, thus spectrum is used very efficiently. Since the user's data is being sent in parallel over multiple antennas, the effective transmission rate is increased roughly proportional

to the number of transmit antennas used. In this system, the number of receivers is greater than or equal to the number of transmitters. The transmitted sub-streams are independent of one another. Individual transmitter power is scaled by $1/N_t$. Therefore, the total power remains constant, independent of the number of transmitters (N_t). After going through the channel, the received signal vector Rec will be:

$$Rec = HS + \zeta \quad (2.1)$$

where Rec is an $N_r \times 1$ vector, S is $N_t \times 1$ transmitted signal vector, ζ is an $N_r \times 1$ noise vector whose elements are complex Gaussian random variables with zero mean and variance N_o , and H is an $N_r \times N_t$ channel matrix.

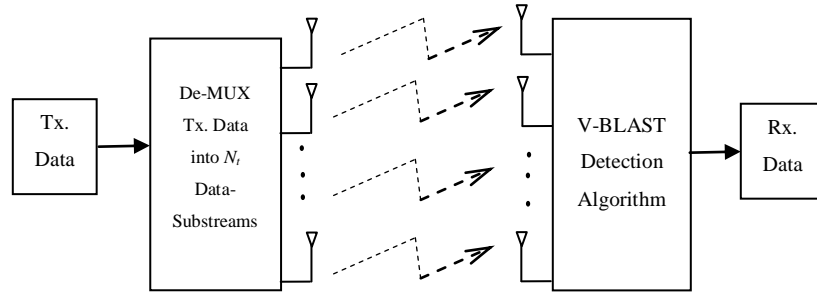


Figure 2.7: V-BLAST system with N_t transmitting and N_r receiving antennas

At receiver side, a V-BLAST detection algorithm is used for detecting the transmitted signal. V-BLAST detection algorithm is the heart of the system and it can be implemented at receiver side using Digital Signal Processor (DSP). Different algorithms have been developed to reduce the computational cost.

2.3 OFDM

OFDM is an attractive multicarrier technique for mitigating the effects of multipath delay spread of radio channel. OFDM is a well-proven technique in applications such as Digital Audio Broadcasting (DAB) and Asymmetric Digital Subscriber Line (ADSL). Furthermore, OFDM is a candidate for the Digital Video Broadcasting (DVB) and high data rate bandwidth efficient wireless networks [5]. In conventional OFDM, complex exponential Fourier bases are used to generate orthogonal subcarriers consist of a series of orthogonal sine/cosine functions. In WOOFDM, wavelet bases are used to generate orthogonal carriers. These bases are generated using symmetric or asymmetric QMF structure of delay or delay-free type [23].

OFDM exhibits robustness against various kinds of interferences and also enables multiple access. In OFDM, the available spectrum B is divided into numerous narrowband sub-channels. A data stream is transmitted by frequency division multiplexing (FDM) using N carriers with frequencies $f_1, f_2, f_1, \dots, f_N$ in parallel. Each sub-channel has a bandwidth of $\Delta f = B/N$. The narrowband property of the sub-channel justifies the assumption that attenuation and group delay are constant within each channel, allowing equalisation to be performed easily.

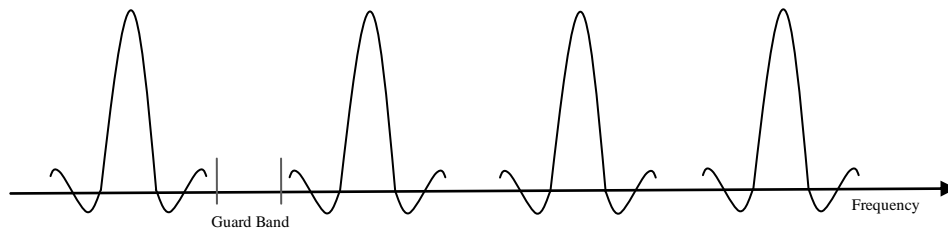
2.3.1 OFDM and Orthogonality Principle

In a typical FDM system, many carriers are spaced apart in such a way that the signals can be received using conventional filters and demodulators. In such receivers, guard bands have to be introduced between the different carriers (Figure 2.8) and the introduction of these guard bands in the frequency domain results in a lower spectrum efficiency.

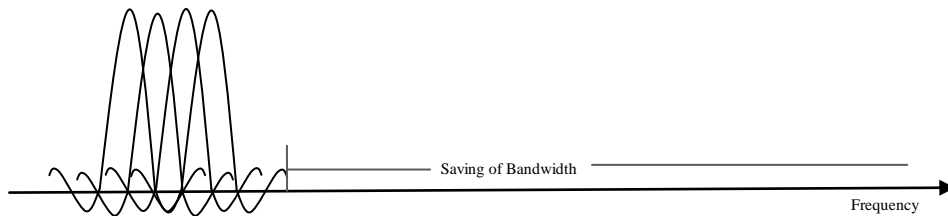
It is possible, however, to arrange the carriers in an OFDM signal so that the sidebands of the individual carriers overlap (Figure 2.8.(b)) while the signals can still be received without adjacent carrier interference. In order to do this, the carriers must be mathematically orthogonal i.e. if given a set of signals Ψ , where Ψ_p and Ψ_q is the p th, and q th element in the set, respectively, and K is some constant, the signals are orthogonal if:

$$\int_a^b \Psi_p(t)\Psi_q^*(t)dt = \begin{cases} K & \text{for } p = q \\ 0 & \text{for } p \neq q \end{cases} \quad (2.2)$$

where * indicates the complex conjugate and interval $[a, b]$ is the symbol period.



(a) Conventional Frequency Division Multiplex (FDM) Multicarrier Modulation Technique



(b) Orthogonal Frequency Division Multiplexing (OFDM) Multicarrier Modulation Technique

Figure 2.8: Comparison of the bandwidth utilisation for FDM and OFDM

2.3.2 Fourier based OFDM (FOFDM)

In FOFDM, a high data rate sub-stream is demultiplexed into lower data rate sub-streams to increase the duration of each sub-stream so that ISI can be reduced. The orthogonal subcarriers are generated using sine/cosine bases and orthogonality is achieved in a time window of width equal to the symbol duration. Therefore, FOFDM is not band limited. Each subcarrier produces side lobes that in turn create ICI, which can be increased due to multipath channel effect that also cause an increase in ISI. Cyclic prefix (CP)/Guard Interval (GI) is added to each FOFDM symbol to avoid this problem at the cost of transmission efficiency degradation.

A basic FOFDM based communication system is shown in Figure 2.9. The FOFDM symbol before transmission without CP can be obtained by taking the Inverse Fast Fourier Transform (IFFT) of the input signal $x_i(n)$:

$$y(n) = IFFT [x_i(n)] = \sum_{i=0}^{N-1} x_i(n) e^{j2\pi i n / N} \quad (2.3)$$

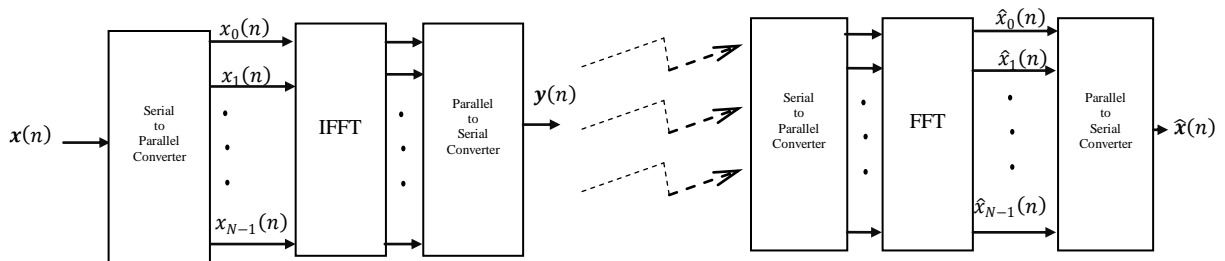


Figure 2.9: A basic FOFDM based communication system

The serial data stream $x(n)$ is converted into N parallel substreams by using serial-to-parallel converter. After passing through the channel, FFT is performed at receiver side to retrieve the signal.

2.3.3 Wavelet based OFDM (WOFDM)

WOFDM is another multicarrier modulation that has only real value samples while FOFDM has real and also imaginary value samples as shown in Figure 2.10. It does not use raised cosine filtering (excess bandwidth=0) and does not use a cyclic prefix. WOFDM modulator is implemented by taking Inverse Discrete Wavelet transform (IDWT). In IDWT, the synthesis part of the delay free Perfect Reconstruction (PR)-QMF with symmetric or asymmetric structure is used. For WOFDM demodulator, DWT (analysis part of the delay free PR-QMF with symmetric or asymmetric structure) is used.

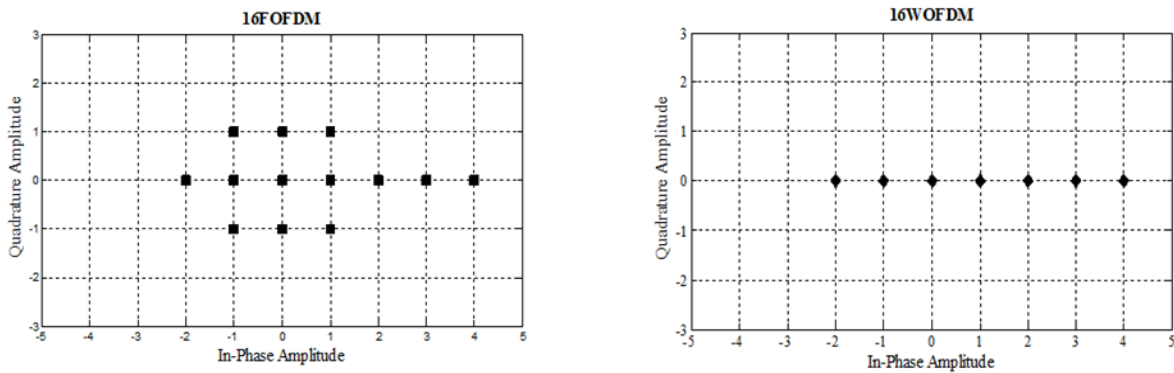


Figure 2.10: Complex values for the waveform samples of FOFDM and WOFDM

Cost and performance optimisation can be better facilitated in WOFDM due to several factors [24]:

- One dimensional real value samples (real modulation) simplifies RF
- High stop-band simplifies RF/IF design
- High stop-band makes design for multi-national standards easier

- Low sensitivity to timing offset
- Simple and accurate frequency tracking from the data itself

The WOFDM modulation uses a wavelet filter for both the transmitter and receiver. These filters are implemented digitally using poly-phase techniques which significantly reduce the computational requirements. Channel interference can arise from several sources in a wireless network such as narrow-band (NB) and co-channel interference. For NB noise, the high stop-band (~ 50 dB) of wavelets provides a significant advantage over other modulations. As the high stop-band applies to each sub-band without additional filtering, frequency selectivity is greater than that obtained from adding notch filters to non-wavelet modulations. Due to this reason, the physical layer overhead for WOFDM is less than that of FOFDM modulation. For wireless communications, FOFDM typically has guard intervals of 20% or more, thus giving WOFDM a corresponding advantage of approximately 20% in bandwidth efficiency [24]. As the bandwidth of the customer's service is a large fraction of the available frequency allocation, the re-use of frequencies can cause severe (i.e. -11 dB) co-channel interference in a cellular system.

As discussed above, the wavelet bases are used to generate orthogonal carriers. These bases are generated using symmetric or asymmetric QMF structure of delay or delay-free type [23].

2.3.3.1 Quadrature Mirror Filters (QMF)

A. Basic Definitions

A.1 UpSampling

The operation of **upsampling** by factor L describes the insertion of $L - 1$ zeros between every sample of the input signal. It is denoted by " $\uparrow L$ " as shown in Figure 2.11.

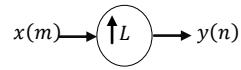


Figure 2.11: UpSampling

Formally, up-sampling can be expressed in the time domain as:

$$y(n) = x(n/L) \quad (2.4)$$

In Z-domain:

$$Y(z) = X(z^L) \quad (2.5)$$

In frequency domain:

$$Y(e^{j\omega}) = X(e^{j\omega L}) \quad (2.6)$$

UpSampling compresses the DTFT by a factor of L along the frequency axis as shown in Figure 2.12.

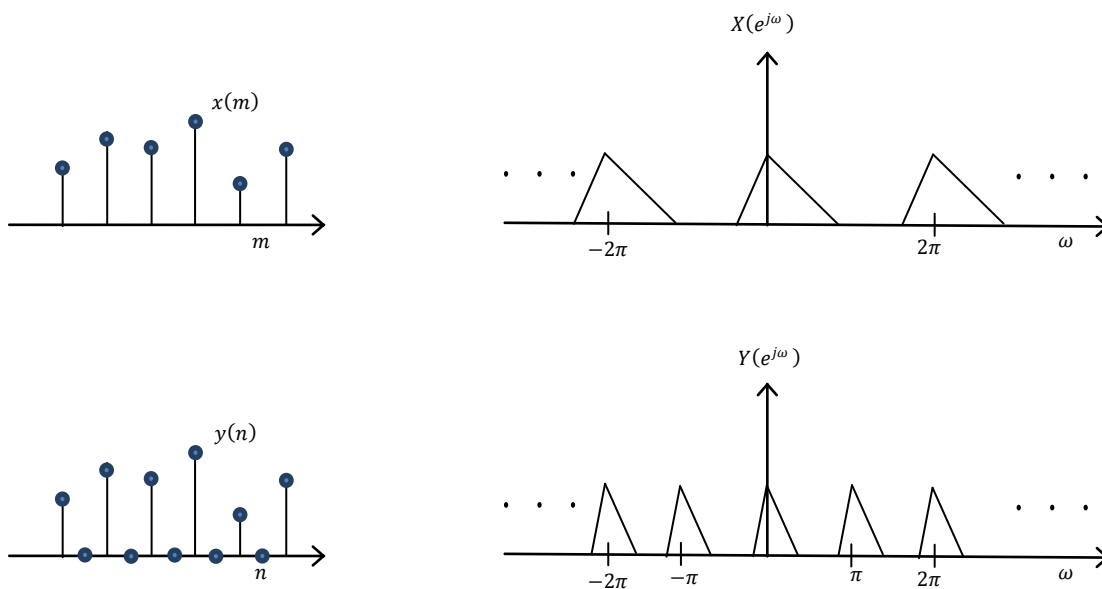


Figure 2.12: Spectrum of the Signal before & after UpSampling

A.2 DownSampling

The operation of **downsampling** by factor M describes the process of keeping every M th sample and discarding the rest. This is denoted by “ $M\downarrow$ ”, as shown in Figure 2.13.

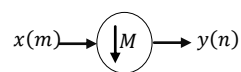


Figure 2.13: DownSampling

In time domain:

$$y(n) = x(nM) \quad (2.7)$$

In Z-domain:

$$Y(z) = \frac{1}{M} \sum_{p=0}^{M-1} X(W_p^M z^{1/M}) \quad (2.8)$$

where $W_M = e^{-j2\pi/M}$

In frequency domain:

$$Y(e^{j\omega}) = \frac{1}{M} \sum_{p=0}^{M-1} \left(X(e^{j(\omega - 2\pi p/M)}) \right) \quad (2.9)$$

As shown in Figure 2.14, downsampling expands each 2π -periodic repetition of $X(e^{j\omega})$ by a factor of M along the ω axis, and reduces the gain by a factor of M . If $x(m)$ is not bandlimited, aliasing may result from spectral overlap.

A.3 ReSampling

Resampling is the process of combining upsampling and downsampling in order to change the sampling rate by a fractional value that can be expressed as a ratio. For example, to resample by

a factor of 1.5, you will upsample by a factor of 3, and then decimate by a factor of 2 (to change the sampling rate by a factor of $\frac{3}{2} = 1.5$).

A.4 Interpolation

Interpolation is the process of upsampling followed by filtering as shown in Figure 2.15. The filtering removes the undesired spectral images. As a linear process, the DSP sense of interpolation is somewhat different from the mathematical sense of interpolation, but the result is conceptually similar: to create in-between samples from the original samples. The primary reason

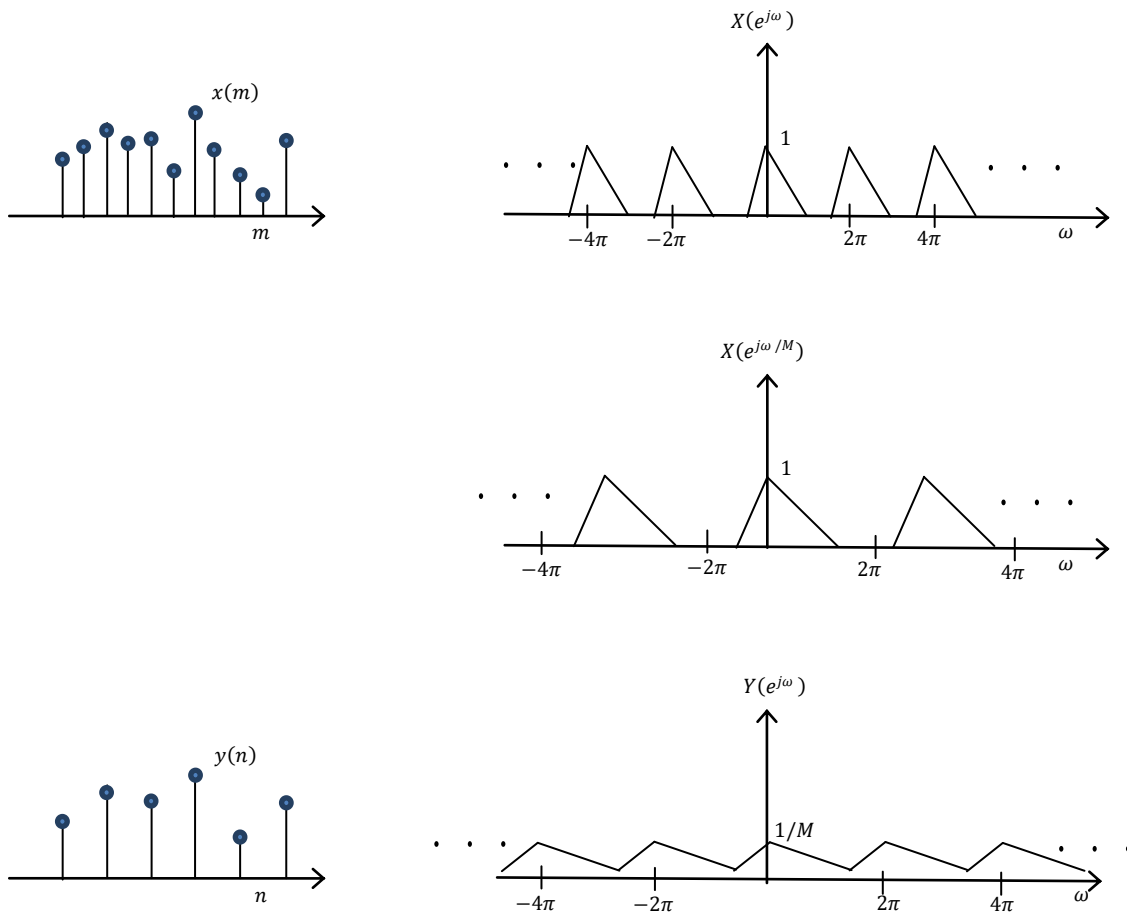


Figure 2.14: Spectrum of the Signal before & after DownSampling

to interpolate is simply to increase the sampling rate at the output of one system so that another system operating at a higher sampling rate can input the signal.

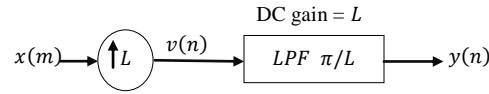


Figure 2.15: Interpolation

The interpolation factor is simply the ratio of the output rate to the input rate. It is usually symbolized by $L = \frac{\text{output rate}}{\text{input rate}}$. Interpolation relies on zero stuffing; therefore interpolation can be done by integer factors, not by fractional factors. However, by combining interpolation and decimation, rational factor can be achieved.

Upsampling adds undesired spectral images to the signal at multiples of the original sampling rate, thus these undesired images are removed by filtering because the upsampled signal is not the same as the original.

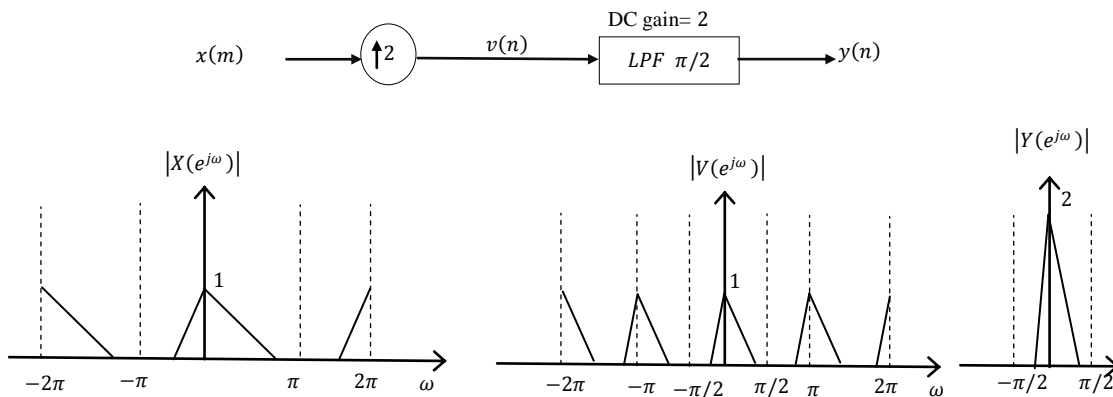


Figure 2.16: Magnitude Response of Interpolated Signal ($L=2$) at Different Stages

Let $x(m)$ be the unaliased T -Sampled version of $x_c(t)$, and $v(n)$ be the upsampled version of $x(m)$. Then $v(n)$ is filtered with an ideal low pass filter of bandwidth π/L and DC gain L to obtain $y(n)$. The magnitude response of signal at different stages is shown in Figure 2.16 for $L = 2$.

If the interpolation ratio L is a prime number, multistage interpolation can be done. For example, to interpolate by a factor of 15, first interpolate by 3, then interpolate by 5.

A.5 Decimation

Decimation is the process of filtering and downsampling a signal to decrease its effective sampling rate. Filtering is employed to prevent aliasing that might otherwise result from downsampling. The decimation factor is simply the ratio of the input rate to the output rate. It is usually symbolised by $M = \frac{\text{input rate}}{\text{output rate}}$. The most immediate reason to decimate is to reduce the sampling rate at the output of a system so that another system operating at a lower sampling rate can process this signal. However, a much more common motivation for decimation is to reduce the cost of processing: the calculation and/or memory required to implement a DSP system generally is proportional to the sampling rate, thus the use of a lower sampling rate usually results in a less costly implementation. Almost anything can be done with the signal with fewer operations at a lower sample rate, and the workload is almost always reduced by more than a factor of M . The process of decimation is shown in Figure 2.17

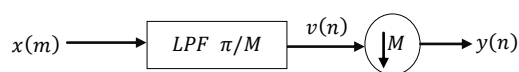


Figure 2.17: Decimation

Let

$$x_c(t) = x_l(t) + x_b(t) \quad (2.10)$$

where $x_l(t)$ is a low frequency component bandlimited to $1/2MT$ Hz, and $x_b(t)$ is a band pass component with energy between $1/2MT$ and $1/2T$ Hz. If sampling $x_c(t)$ with interval T yields an unaliased discrete signal $x(m)$, then decimating $x(m)$ by a factor M will yield $y(n)$, an unaliased sampled representation of low pass component $x_l(t)$. The magnitude response of signal at different stages is shown in Figure 2.18 for $M = 2$.

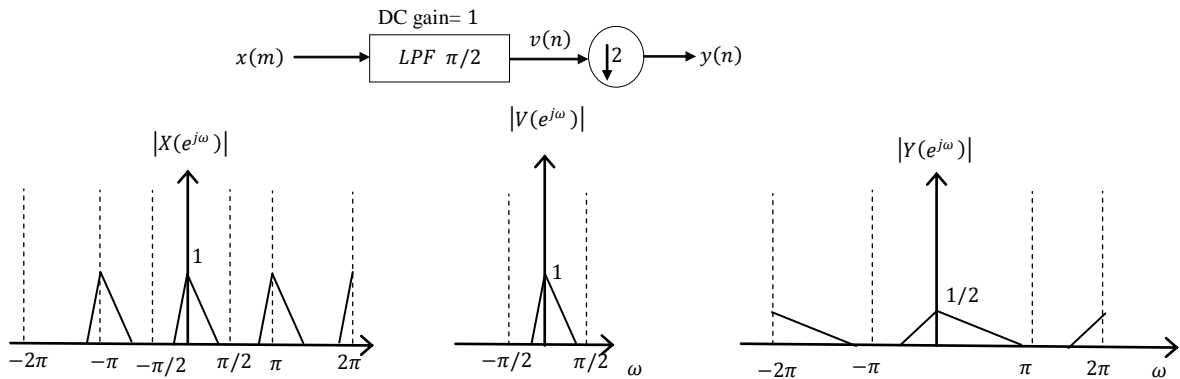


Figure 2.18: Magnitude Response of Decimated Signal ($M = 2$) at Different Stages

B. Two-Channel Multirate Filter Bank

A two channel multirate filter bank is shown in Figure 2.19. Multirate filter banks are so named because they effectively alter the sampling rate of a digital system, as indicated by the decimators (downsamplers) following the analysis filters $G_L(z)$ and $G_H(z)$, and the expanders (upsamplers) preceding the synthesis filters, $F_L(z)$ and $F_H(z)$.

Properly designed analysis and synthesis filters combined with the properties of decimation and expansion allow filter banks to partition a wideband input signal into multiple frequency bands (often called sub-bands or channels) and to recombine these sub-band signals back into

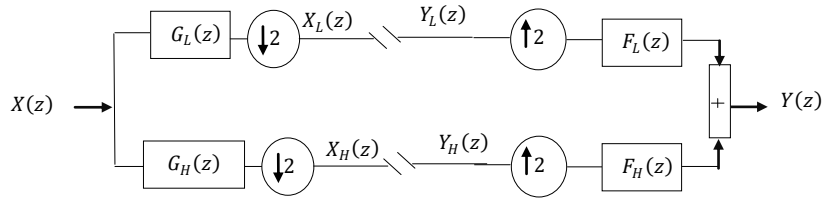


Figure 2.19: Two-Channel QMF Filter Bank

the original signal. In the case of Figure 2.19, the analysis filters $G_L(z)$, and $G_H(z)$, are typically complementary lowpass, and highpass filters, respectively [25] that mirror each other at about $\frac{\omega}{\pi} = 0.5$ as shown in Figure 2.20. Such filters are often called QMF bank. As a result of decimation, a certain amount of aliasing will be introduced in the decimated signals since the filters are non-ideal. The beauty of QMF bank is that the synthesis filters can be chosen so that the aliasing can be canceled in reconstruction process.

Denote the lowpass and highpass outputs of the decimators as $X_L(z)$, and $X_H(z)$, respectively. It then follows that:

$$X_L(z) = \frac{1}{2} [X(z^{1/2})G_L(z^{1/2}) + X(z^{-1/2})G_L(z^{-1/2})] \quad (2.11)$$

$$X_H(z) = \frac{1}{2} [X(z^{1/2})G_H(z^{1/2}) + X(z^{-1/2})G_H(z^{-1/2})] \quad (2.12)$$

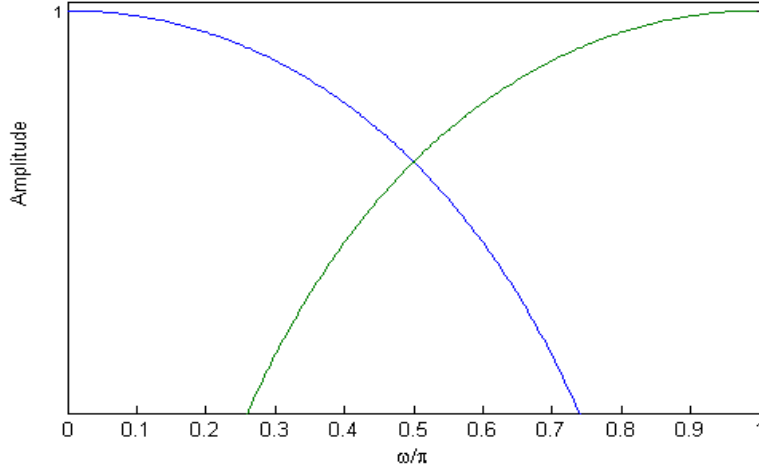


Figure 2.20: Lowpass and Highpass Analysis Filters Frequency Response using Haar Coefficients

Next, let $Y_L(z)$ and $Y_H(z)$ denote the lowpass, and highpass input, respectively, to upsamplers. The outputs of upsampler are then given by $Y_L(z^2)$, and $Y_H(z^2)$, respectively. The output of QMF bank is hence given by:

$$Y(z) = F_L(z)Y_L(z^2) + F_H(z)Y_H(z^2) \quad (2.13)$$

Suppose that the outputs of the analysis section are fed to the inputs of the synthesis section, i.e. $X_L(z) = Y_L(z)$, and $X_H(z) = Y_H(z)$. Then substituting Equations 2.11 and 2.12 into Equation 2.13 gives:

$$Y(z) = \frac{1}{2}[G_L(z)F_L(z) + G_H(z)F_H(z)]X(z) + \frac{1}{2}[G_L(-z)F_L(z) + G_H(-z)F_H(z)]X(-z) \quad (2.14)$$

The first term in Equation 2.14 is the desired output of the QMF bank. The second term is aliasing term which is to be removed. This is accomplished by requiring that:

$$G_L(-z)F_L(z) + G_H(-z)F_H(z) = 0 \quad (2.15)$$

This is satisfied by choosing:

$$F_L(z) = G_H(-z) \text{ and } F_H(z) = -G_L(-z)$$

With the aliasing term eliminated, the output of QMF bank is then given by:

$$Y(z) = \frac{1}{2} [G_L(z)G_H(-z) - G_H(z)G_L(-z)]X(z) \quad (2.16)$$

The transfer function of QMF bank is given by:

$$T(z) = \frac{1}{2} [G_L(z)G_H(-z) - G_H(z)G_L(-z)] \quad (2.17)$$

where

$$G_H(z) = G_L(-z)$$

B.1 Perfect Reconstruction Quadrature Mirror Filters (PR-QMF)

The output of a perfect reconstruction QMF is equal to its input with some time delay.

If $G_H(z)$ is taken as given in Equation 2.18,

$$G_H(z) = (-1^{N-1})z^{-(N-1)}G_L(-z^{-1}) \quad (2.18)$$

Then the transfer function will become:

$$T(z) = \beta z^{-(N-1)} \quad (2.19)$$

for some constant β . Thus, the output of PR-QMF is simply a delayed and scaled version of the input.

Let

$$G_L(z) = 1 + z^{-1}$$

Then $N = 2$ and from Equation 2.18, $G_H(z)$ will become,

$$G_H(z) = (-1^{2-1})z^{-(2-1)}G_L(-z^{-1})$$

$$G_H(z) = (-1)z^{-1}(1 - z) = 1 - z^{-1}$$

Substituting into Equation 2.17, $T(z)$ becomes:

$$T(z) = \frac{1}{2}[(1 + z^{-1})(1 + z^{-1}) - (1 - z^{-1})(1 - z^{-1})]$$

$$T(z) = 2 z^{-1}$$

B.2 Delay Free Perfect Reconstruction Quadrature Mirror Filters (PR-QMF)

By making the synthesis side lowpass and highpass filter non-causal (time reversal of the analysis side lowpass and highpass filters), it will simply make the transfer function of QMF delay-free without affecting perfect reconstruction properties.

$$F_L(z) = G_L(z^{-1}) \tag{2.20}$$

$$F_H(z) = G_H(z^{-1}) \tag{2.21}$$

$$T(z) = \beta \tag{2.22}$$

Thus, the output of PR-QMF is a delay-free and scaled version of the input.

Let

$$G_L(z) = 1 + z^{-1}$$

$$G_H(z) = 1 - z^{-1}$$

$$F_L(z) = 1 + z$$

$$F_H(z) = 1 - z$$

Then Equation 2.14 becomes:

$$Y(z) = \frac{1}{2} [(1 + z^{-1})(1 + z) + (1 - z^{-1})(1 - z)]X(z) \\ + \frac{1}{2} [(1 - z^{-1})(1 + z) + (1 + z^{-1})(1 - z)]X(-z)$$

$$Y(z) = \frac{1}{2} [2 + 2]X(z) + \frac{1}{2} [(z - z^{-1}) + (-z + z^{-1})]X(-z)$$

$$Y(z) = 2 X(z) + \frac{1}{2} [0]X(-z)$$

$$Y(z) = 2 X(z)$$

where

$$T(z) = 2$$

C. Multilevel Filter Banks

Multilevel Filter Banks are developed by iterating a two- or more channel QMF bank. If the two-band QMF is a PR-QMF or delay-free PR-QMF, then the generated multiband structure also exhibits the same properties. The orthonormal wavelets are generated using multilevel QMF bank.

C.1 Symmetric Synthesis Filter Bank

In the symmetric structure, both the low- and high-frequency sub-band inputs to each level are the outputs from the previous level as shown in Figure 2.21.

It is a two level structure with four inputs. Thus, if the number of levels is p , then the number of inputs is 2^p . The low-frequency sub-band input to each level (except the first) is the output of the previous level. The low frequency sub-band input to the first level, and the high frequency sub-band input to each level, are inputs to the filter bank. All inputs sub-bands have bandwidth $BW/2^p$ and $N/2^p$ samples, where the output has bandwidth BW and N samples.

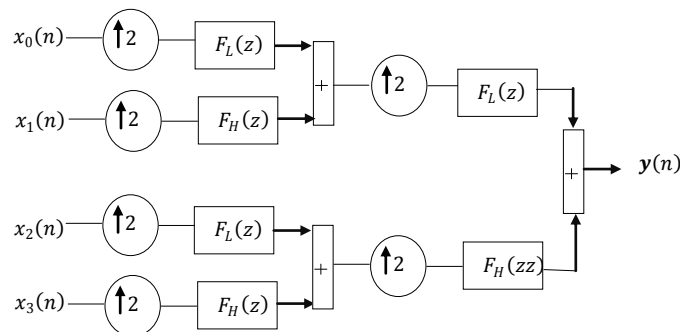


Figure 2.21: Symmetric Synthesis Two Level Filter Bank

Its equivalent structure using noble identities is shown in Figure 2.22:

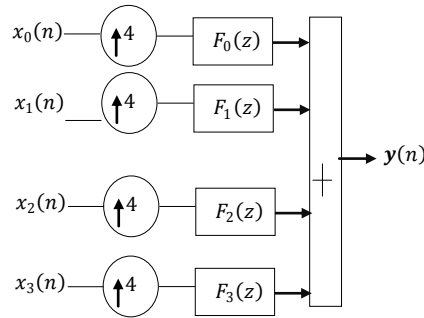


Figure 2.22: Equivalent Structure of Symmetric Synthesis Two Level Filter Bank using Noble Identities

where

$$F_0(z) = F_L(z^2)F_L(z)$$

$$F_1(z) = F_H(z^2)F_L(z)$$

$$F_2(z) = F_L(z^2)F_H(z)$$

$$F_3(z) = F_H(z^2)F_H(z)$$

C.2 Symmetric Analysis Filter Bank

Symmetric analysis filter bank is generated by inserting QMF analysis filter bank to each branch of QMF analysis filter bank as shown in the Figure 2.23.

It is a two level structure with four outputs. Thus, if the number of levels is p , then the number of outputs is 2^p . All the low-frequency and high-frequency sub-bands in a level are decomposed in the next level. For an input with bandwidth BW and N samples, all outputs have bandwidth $BW/2^p$ and $N/2^p$ samples. All output sub-bands have a sample period of $Tsi/2^p$ where Tsi is the sample rate of the input signal. Its equivalent structure using noble identities is shown in

Figure 2.24:

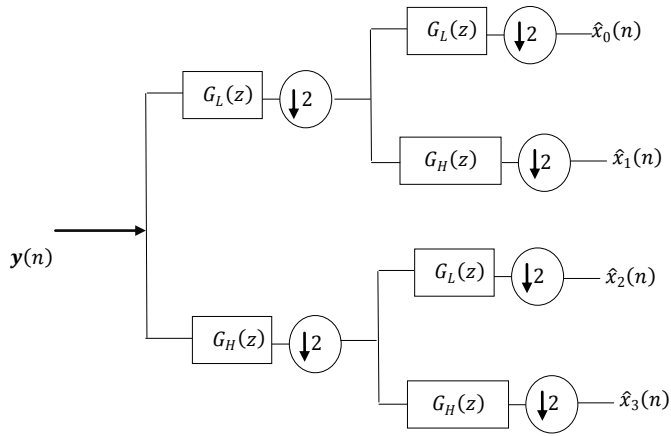


Figure 2.23: Symmetric Analysis Two Level Filter Bank

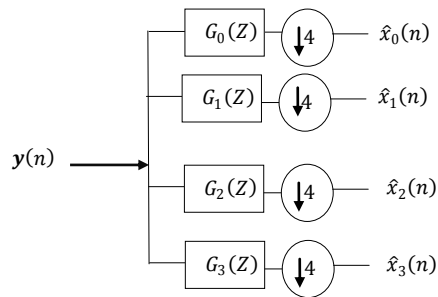


Figure 2.24: Equivalent Structure of Symmetric Analysis Two Level Filter Bank using Noble Identities

where

$$G_0(z) = F_0(z^{-1})$$

$$G_1(z) = F_1(z^{-1})$$

$$G_2(z) = F_2(z^{-1})$$

$$G_3(z) = F_3(z^{-1})$$

The analysis filter bank is the time reversal of synthesis filter bank which gives delay free perfect reconstruction.

C.3 Asymmetric Synthesis Filter Bank

In the asymmetric structure, the low-frequency sub-band input to each level is the output of the previous level, while the high-frequency sub-band input to each level is an input to the filter bank as shown in Figure 2.25.

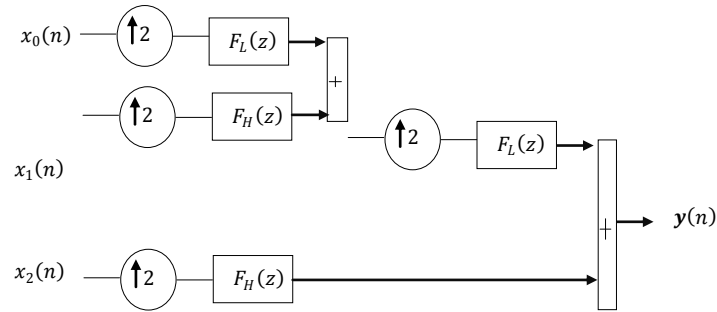


Figure 2.25: Asymmetric Synthesis Two Level Filter Bank

It is a two level structure with three inputs. Thus, if the number of levels is p , then the number of inputs is $p + 1$. For a bandwidth BW and N samples, the k th input sub-band has the following bandwidth and number of samples.

$$BW_k = \frac{BW}{2^k} \quad 1 \leq k \leq p \quad (2.21)$$

$$BW_k = \frac{BW}{2^k} \quad k = p + 1 \quad (2.22)$$

similarly,

$$N_k = \frac{N}{2^k} \quad 1 \leq k \leq p \quad (2.23)$$

$$N_k = \frac{N}{2^k} k = p + 1 \quad (2.24)$$

Its equivalent structure using noble identities is shown in Figure 2.26.

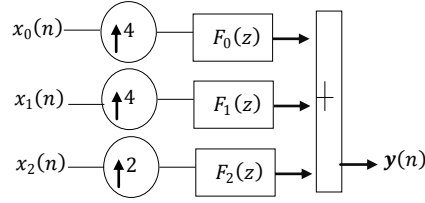


Figure 2.26: Equivalent Structure of Asymmetric Synthesis Two Level Filter Bank using Noble Identities

where

$$F_0(z) = F_L(z^2)F_L(z)$$

$$F_1(z) = F_H(z^2)F_L(z)$$

$$F_2(z) = F_H(z)$$

C.4 Asymmetric Analysis Filter Bank

The asymmetric structure decomposes only the low-frequency output from each level. Each level's low-frequency sub-band is decomposed in the next level, and each level's high-frequency sub-band is an output of the filter bank as shown in Figure 2.27.

It is a two level structure with three outputs. Thus, if the number of levels is p , then the number of outputs is $p + 1$. Its equivalent structure using noble identities is shown in Figure 2.28.

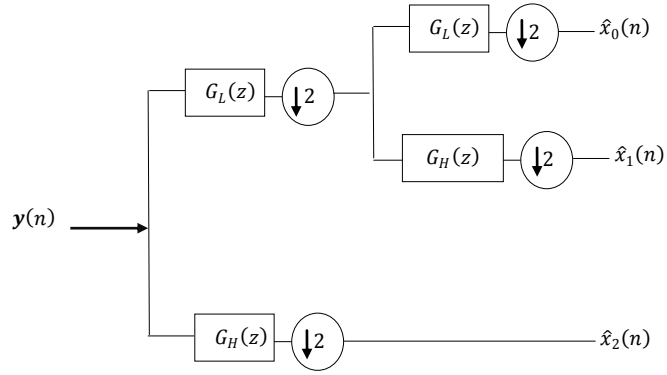


Figure 2.27: Asymmetric Analysis Two Level Filter Bank

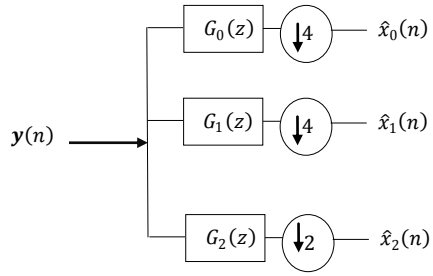


Figure 2.28: Equivalent Structure of Asymmetric Synthesis Two Level Filter Bank using Noble Identities

where

$$G_0(z) = F_0(z^{-1})$$

$$G_1(z) = F_1(z^{-1})$$

$$G_2(z) = F_2(z^{-1})$$

The analysis filter bank is the time reversal of synthesis filter bank which gives delay free perfect reconstruction.

Chapter 3

Review of the State of the Art

3.1 Multiple Antenna Systems

Due to the advent of multimedia applications such as mobile video on-demand or multimedia surveillance using WMSN, high data rate wireless communication systems are required. However, higher data rates necessitate more energy per bit for a given bit error rate (BER), which in turn increases the overall system energy consumption and the production of CO₂emission that is a threat to global warming. Thus, researching energy efficient designs for high data-rate wireless communication systems is a burning issue. Due to escalating expansion of wireless network infrastructures and exponential growth in traffic rate, a considerable amount of worldwide energy is consumed by information and communication technology (ICT) of which more than 70% is being used by radio access part/radio frequency (RF) section [26].

Capacity and reliability of wireless communication systems can be improved by using multiple antennas with the same transmit power and bandwidth as required by single antenna systems [22].Diagonal Bell Labs Layered Space-Time (D-BLAST), a spatial multiplexing technique, was proposed in [27] to transmit independent information sequences using multiple antennas to increase the overall data rate as compared to single antenna system without additional bandwidth or power. Due to implementation complexity of D-BLAST, a simplified version known as

Vertical BLAST (V-BLAST) was proposed by Wolniansky et al. [22], and a prototype implementation of V-BLAST architecture with Zero Forcing detection algorithm was discussed. The results showed high spectral efficiency as compared to traditional single-input single-output (SISO) communication system. D-BLAST and V-BLAST systems work efficiently if the number of receiving antennas N_r is equal or greater than the number of transmitting antennas N_t ($N_t \leq N_r$). A Turbo-BLAST technique was later proposed by Sellathurai & Haykin [28], which can perform well even if N_r is less than N_t ($N_r < N_t$).

A well-known STC technique was devised by Alamouti [29] to improve BER performance of the multi antenna setup by transmitting and/or receiving redundant copies of the information signals without decreasing the data rate as compared to single antenna system. Space-time trellis coding (STTC) technique was invented by Tarokh et al. [30] which performed better than Alamouti coding technique but with more decoding complexity. Orthogonal space-time block codes (OSTBC) were proposed to further maximise the possible spatial diversity and allow simple decoding algorithms based on linear processing [31]. A spatio-temporal vector coding (STVC) communication structure was suggested by Raleigh & Cioffi [32] as a means for achieving high MIMO channel capacity using singular value decomposition (SVD) and Eigen value decomposition. However, for this technique, channel state information (CSI) is required at transmitter as well as receiver side.

Multi antenna systems can also be used for beamforming to increase signal-to-noise ratio (SNR) at the receiver and to suppress co-channel interference in multi user networks [33]. A multi-functional MIMO system design was proposed in [34] to attain multiplexing gain, diversity gain

and beamforming gain. To exploit the advantages of MIMO systems, the concept of virtual or cooperative/distributive MIMO is used for resource limited and small size nodes [35, 21].

3.1.1 Spatial Multiplexing Techniques

By using spatial multiplexing techniques, the number of users or data rate of a single user can be increased by the factor of number of transmitting antennas (N_t) for the same transmission power and bandwidth. Since the user's data is being sent simultaneously in parallel over multiple antennas, the effective transmission rate is increased roughly in proportion to the number of transmit antennas used. All the sub-streams are transmitted in the same frequency band, thus the spectrum is used very efficiently. The transmitted sub-streams are also independent of one another. Individual transmitter antenna power is scaled by $1/N_t$, thus the total power remains constant and independent of N_t . At the receiver, the transmitted signals are retrieved from received sequences (layers) by using detection algorithms. The basic spatial multiplexing system architecture is shown in Figure 3.1.

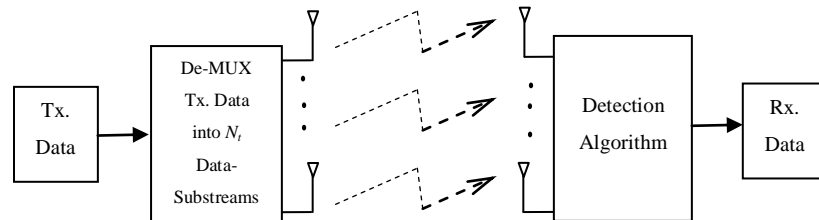


Figure 3.1: Spatial multiplexing system architecture with N_t transmitting and N_r receiving antennas

3.1.1.1 D-BLAST

D-BLAST is a spatial multiplexing technique designed to achieve spectral efficiency for a given bit rate and transmission power [27]. For this technique, CSI is required at receiver side but not at transmitter side. For N_t transmitting antennas and N_r receiving antennas, the i_{th} codeword is made up “diagonally” with N_t transmitted signals.

Assume that at time $t = t_1$, only antenna a_1 transmits its data and all other transmitting antennas remains silent. At time $t = t_2$, antennas a_1 and a_2 transmit their data. At time $t = t_{N_t}$, all transmitting antennas (a_1, a_2, \dots, a_{N_t}) transmit their data. At time $t = t_{N_t} + 1$, again all transmitting antennas transmit their data, and so on. The code block in time-space dimension for $N_t = 4$ is shown below:

$$S = \begin{bmatrix} s_{11}^1 & s_{12}^2 & s_{13}^3 & s_{14}^4 & \dots \\ 0 & s_{22}^1 & s_{23}^2 & s_{24}^3 & \dots \\ 0 & 0 & s_{33}^1 & s_{34}^2 & \dots \\ 0 & 0 & 0 & s_{44}^4 & \dots \end{bmatrix} \quad (3.1)$$

where s_{jk}^i is the symbol transmitted from j_{th} antenna at k_{th} time slot of i_{th} code word. The received signal at the receiver with N_r receiving antennas, when s_{11}^1 was transmitted, can be expressed as follows:

$$Rec = Hs_{11}^1 + \zeta \quad (3.2)$$

where Rec is an $N_r \times I$ vector, ζ is an $N_r \times I$ noise vector whose elements are complex Gaussian random variables with zero mean and variance N_o , and H is an $N_r \times I$ channel matrix. At receiver side, s_{11}^1 can be estimated using maximal ratio combining (MRC) with the help of following equation:

$$s_{11}^{\hat{1}} = \frac{H^* Rec}{H^* H} \quad (3.3)$$

where $*$ represents hermitian of H (transpose and complex conjugate). Symbol s_{22}^1 can be calculated using minimum mean square error (MMSE). The received signal vector can be expressed as:

$$Rec = HX + \zeta \quad (3.4)$$

where $X = \begin{bmatrix} s_{12}^2 \\ s_{22}^1 \end{bmatrix}$ and $H = \begin{bmatrix} h_{11} & h_{12} \\ h_{21} & h_{22} \\ h_{31} & h_{32} \\ \vdots & \vdots \\ h_{N_r 1} & h_{N_r 2} \end{bmatrix}$ and ζ is an $N_r \times I$ noise vector whose elements are

complex Gaussian random variables with zero mean and variance N_o . During this time slot, only antennas a_1 and a_2 transmitted the signals.

The symbol s_{22}^1 transmitted at second time slot from antenna a_2 (i.e. $n_t = 2$) is estimated by using the following steps [36]:

- Replace first column (all $n_t - 1$ columns) of H by null column so that $H_{new} = \begin{bmatrix} 0 & h_{12} \\ 0 & h_{22} \\ 0 & h_{32} \\ \vdots & \vdots \\ 0 & h_{N_r 2} \end{bmatrix}$

- Calculate $G_{MMSE} = H_{new}^* \left[H_{new} H_{new}^* + \frac{1}{SNR} I_{N_r} \right]^{-1}$ where $\frac{1}{SNR}$ is the noise power to signal power ratio, and I_{N_r} is the identity matrix of size N_r
- Select the second ($n_t = 2$) row of G_{MMSE}
- Estimate s_{22}^1 : $s_{22}^{\hat{1}} = G_{MMSE_2} Rec$
- Subtract the effect of $s_{22}^{\hat{1}}$ ($Rec - \begin{bmatrix} h_{12} \\ h_{22} \end{bmatrix} s_{22}^{\hat{1}}$) such that s_{12}^2 sees again an interference-free channel and MRC can be used to detect s_{12}^2

By using D-BLAST, there is wastage of space and time in the initial phase of transmission and error will propagate in the event of wrong signal detected.

3.1.1.2 V-BLAST

As introduced in Section 2.2.3, V-BLAST is a highly bandwidth efficient approach to spatial multiplexing for a given bit rate and transmission power. This technique enables simpler encoding on transmitter side than D-BLAST [22] and there is no resource (space and time) wastage during initialisation phase of transmission. In this technique, CSI is required at receiver side but not at transmitter side. For N_t transmitting antennas and N_r receiving antennas, the i_{th} codeword is made up “vertically” with N_t transmitted signals.

Assume that at time $t = t_1$, all transmitting antennas transmit their data, and at time $t = t_2$, again all transmitting antennas transmit their data, and so on. The code block in time-space dimension for $N_t = 4$ is shown below:

$$S = \begin{bmatrix} s_{11}^1 & s_{12}^2 & s_{13}^3 & s_{14}^4 & \dots \\ s_{21}^1 & s_{22}^2 & s_{23}^3 & s_{24}^4 & \dots \\ s_{31}^1 & s_{32}^2 & s_{33}^3 & s_{34}^4 & \dots \\ s_{41}^1 & s_{42}^2 & s_{43}^3 & s_{44}^4 & \dots \end{bmatrix} \quad (3.5)$$

where s_{jk}^i is the symbol transmitted from j_{th} antenna at k_{th} time slot of i_{th} code word. The received signal at the receiver with N_r receiving antennas, when i_{th} code word was transmitted from N_t transmitting antennas can be expressed as follows:

$$Rec = HX + \zeta \quad (3.6)$$

where X is an $N_t \times I$ vector, ζ is an $N_r \times I$ noise vector whose elements are complex Gaussian random variables with zero mean and variance N_o , and H is an $N_r \times N_t$ channel matrix. Different detection algorithms have been proposed for V-BLAST system architecture. In this chapter, we discuss the following three well-known detection algorithms.

A. Detection Algorithms

A.1 Zero-Forcing Detection Algorithm

The Zero-Forcing (ZF) detection algorithm is a low complexity but sub-optimal detection algorithm presented in [22]. At each symbol time, it first detects the “strongest” layer and then cancels the effect of this strongest layer from each of the received signals, and proceeds to detect the “strongest” of the remaining layers, and so on. This algorithm consists of the following steps with the assumption that channel response “ H ” is known at receiver side.

- Determine the optimal detection order that corresponds to choosing the row of G (also referred to as nulling matrix) with minimum Euclidian norm, where P is a column matrix whose entities correspond to Euclidian norm of each row of G matrix:

$$G = (H^*H)^{-1}H^*$$

$$P = \begin{bmatrix} \|G_{k=1}\|^2 \\ \vdots \\ \|G_{k=N_t}\|^2 \end{bmatrix}$$

- Choose the row $(\underline{G})_i$ and multiply it with Rec to obtain a “strongest” signal y_i where i is the index of row column vector P with minimum value:

$$y_i = (\underline{G})_i Rec$$

- The estimated value of the strongest transmitted signal is detected by slicing y_i to the nearest value in the signal constellation:

$$\hat{S}_i = Q(y_i)$$

- Since the strongest transmitted signal has been detected, its effect should be cancelled from the received signal vector to reduce the detection complexity for the remaining transmitted signals:

$$Rec = Rec - \hat{S}_i(H)_i$$

- Replace $(\underline{P})_i$ by ∞ , so that in the next cycle, the row $(\underline{G})_i$ with minimum value is chosen

A.2 MMSE Detection Algorithm

The minimum mean square error (MMSE) detection algorithm has almost the same computational complexity as ZF detection algorithm, but gives more reliable results even with a noisy estimation of channel due to the introduction of diagonal matrix $(\frac{1}{SNR} I_{N_r})$ in MMSE filter (G_{MMSE}) equation [37]. This algorithm consists of the following steps with the assumption that channel response “ H ” is known at receiver side:

- Calculate $G_{MMSE} = H^* \left[HH^* + \frac{1}{SNR} I_{N_r} \right]^{-1}$ where $\frac{1}{SNR}$ is noise power to signal power ratio, and I_{N_r} is the identity matrix of size N_r
- Select the i_{th} row of G_{MMSE} and multiply it with Rec to detect the signal y_i :

$$y_i = \left(\underline{G_{MMSE}} \right)_i Rec$$

- The estimated value of the signal is detected by slicing y_i to the nearest value in the signal constellation:

$$\hat{S}_i = Q(y_i)$$

A.3 QR Decomposition Detection Algorithm

The computational complexity of QR Decomposition detection algorithm is less as compared to the above mentioned detection algorithms [38], but with a slight performance degradation. This algorithm consists of the following steps with the assumption that channel response “ H ” is known at receiver side:

- Denoting channel response matrix $H = QR$, where Q is $N_r \times N_t$ unitary matrix composed of orthonormal columns with unit norm, and R is $N_r \times N_t$ upper triangular matrix
- The received signal expression in equation (3.6) can be modified to detect the transmitted signals by multiplying it with Q^t (transpose of Q) as follows:

$$\widetilde{R}ec = Q^t Rec = Q^t (HS + \zeta) = Q^t QRS + \eta \Rightarrow RS + \eta$$

where $Q^t Q = I$ (identity matrix), and $\eta = Q^t \zeta$ is statistically identical to ζ .

- Due to upper triangular structure of R , the i_{th} element of $\widetilde{R}ec$ is given by:

$$\widetilde{r}ec_i = r_{ii}s_i + d_i + \eta_i$$

where $d_i = \sum_{j=i+1}^{N_t} r_{ij} s_j$ is the interference term.

- The interference free signal element is given by:

$$z_i = \widetilde{r}ec_i - d_i$$

- Detected signal corresponding to each receiving antenna can be calculated using $\hat{y}_i = \frac{z_i}{r_{ii}}$

and sliced to the nearest value in the signal constellation to estimate the symbol \hat{S}_i

3.1.1.3 Turbo-BLAST

As mentioned above, this technique can be performed well even if the number of receiving antennas N_r is less than transmitting antennas N_t ($N_r < N_t$) but with more computational complexity on receiver side. In this technique, data sub-streams are interleaved using time inter-leavers and diagonal layering space inter-leavers. Similar to V-BLAST, there is no resource (space and time) wastage during initialisation phase of transmission as involved in D-BLAST, and similarly CSI is required at receiver side but not at transmitter side.

For N_t transmitting antennas and N_r receiving antennas, the i_{th} codeword is made up “diagonally” (as opposed to “vertically” in V-BLAST) with N_t transmitted signals. Assume that at time $t = t_1$, all transmitting antennas transmit their data, and at time $t = t_2$, again all

transmitting antennas transmit their data, and so on. The code block in time-space dimension for $N_t = 4$ is shown below:

$$S = \begin{bmatrix} s_{11}^1 & s_{12}^4 & s_{13}^3 & s_{14}^2 & \dots \\ s_{21}^2 & s_{22}^1 & s_{23}^4 & s_{24}^3 & \dots \\ s_{31}^3 & s_{32}^2 & s_{33}^1 & s_{34}^4 & \dots \\ s_{41}^4 & s_{42}^3 & s_{43}^2 & s_{44}^1 & \dots \end{bmatrix} \quad (3.7)$$

where s_{jk}^i is the symbol transmitted from j_{th} antenna at k_{th} time slot of i_{th} code word. The received signal at the receiver with N_r receiving and N_t transmitted antennas can be expressed as follows:

$$Rec = HX + \zeta \quad (3.8)$$

where X is an $N_t \times I$ vector, ζ is an $N_r \times I$ noise vector whose elements are complex Gaussian random variables with zero mean and variance N_o , and H is an $N_r \times N_t$ channel matrix. If x_i is the desired signal to be detected on receiver side, the above equation can be rewrite as:

$$Rec = \mathbf{h}_i x_i + H_i X_i + \zeta \quad (3.9)$$

where \mathbf{h}_i is the i_{th} column of channel matrix H , $H_i = [\mathbf{h}_1 \quad \mathbf{h}_2 \quad \dots \quad \mathbf{h}_{i-1} \quad \mathbf{h}_{i+1} \quad \dots \quad \mathbf{h}_{N_t}]$ is $N_r \times N_t - 1$ matrix and $X_i = [x_1 \quad x_2 \quad \dots \quad x_{i-1} \quad x_{i+1} \quad \dots \quad x_{N_t}]$. The following steps of the optimal MMSE algorithm [4] can be used to detect the signals:

- Calculate $G_{MMSE_i} = \mathbf{h}_i^* \left[\mathbf{h}_i^* \mathbf{h}_i + \frac{1}{SNR} \right]^{-1}$, where $\frac{1}{SNR}$ is the noise power to signal power ratio
- $y_i = G_{MMSE_i} (Rec - H_i E[X_i])$, where $E[X_i]$ is the expected value of x_i . For the first iteration, it can be assumed that $E[X_i] = 0$, and with the increase in the number of iterations, $E[X_i] \rightarrow X_i$.
- The estimated value of the signal is detected by slicing y_i to the nearest value in the signal constellation: $\hat{S}_i = Q(y_i)$

3.1.2 Space-Time Coding (STC) Techniques

By using space and time (two-dimensional) coding, multiple antenna setups can be used to attain coding gain and diversity gain for the same bit rate, transmission power and bandwidth as compared single antenna system. In STC techniques, information bits are transmitted according to some pre-defined transmission sequence. At the receiver, the received signals

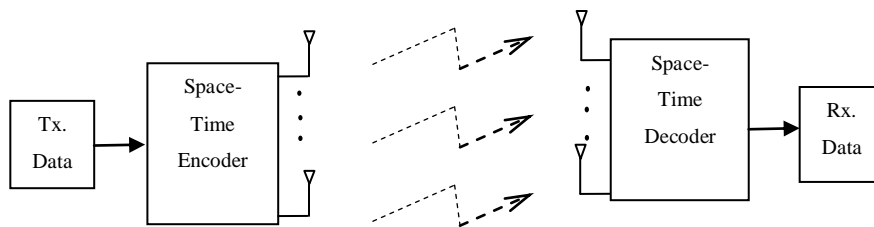


Figure 3.2: Space-time coding system architecture with N_t transmitting and N_r receiving antennas

are combined by using optimal combining scheme, followed by a decision rule for maximum likelihood detection. The basic spatial multiplexing system architecture is shown in Figure 3.2.

3.1.2.1 Alamouti Space-Time Coding Technique

As mentioned, STC improves the BER performance of the multi antenna setup by transmitting and/or receiving redundant copies of the information signals without decreasing the data rate as compared to single antenna system [29]. Consider a multiple antenna setup with two transmitting and one receiving antenna. At time t_1 , antenna a_1 transmits symbol s_1 and antenna a_2 transmits symbol s_2 . At time t_2 , antenna a_1 transmits symbol $-s_2^*$ and antenna a_2 transmits symbol s_1^* , where * denotes the complex conjugate. The received signals r_1 (corresponding to time t_1) and r_2 (corresponding to time t_2) can be expressed as:

$$\begin{bmatrix} r_1 & r_2 \end{bmatrix} = \begin{bmatrix} h_{11} & h_{12} \end{bmatrix} \begin{bmatrix} s_1 & -s_2^* \\ s_2 & s_1^* \end{bmatrix} + \begin{bmatrix} \zeta_1 \\ \zeta_2 \end{bmatrix} \quad (3.10)$$

where $h_{nm} = \alpha_{nm} e^{j\theta_{nm}}$ is the channel response between m_{th} transmitting and n_{th} receiving antenna and it is assumed that fading is constant across consecutive transmitting symbols. The received signals can be combined by using the following equation:

$$\begin{bmatrix} \widetilde{y}_1 \\ \widetilde{y}_2 \end{bmatrix} = \begin{bmatrix} h_{11}^* & h_{12} \\ h_{12}^* & -h_{11} \end{bmatrix} \begin{bmatrix} r_1 \\ r_2^* \end{bmatrix} \quad (3.11)$$

which is then divided by $(|h_{11}|^2 + |h_{12}|^2)$ such that:

$$\begin{bmatrix} \widetilde{s}_1 \\ \widetilde{s}_2 \end{bmatrix} = \frac{\begin{bmatrix} \widetilde{y}_1 \\ \widetilde{y}_2 \end{bmatrix}}{(|h_{11}|^2 + |h_{12}|^2)} \quad (3.12)$$

Finally, the signals are estimated by slicing \widetilde{s}_m to the nearest value in the signal constellation:

$$\widehat{s}_m = Q(\widetilde{s}_m) \quad (3.13)$$

3.1.2.2 Space-Time Trellis Coding (STTC) Technique

This technique was first proposed by Tarokh et al. [30], in which space and time are used to transmit encoded symbols (code words) to achieve coding gain and also diversity gain. Trellis coded modulation (TCM) [39] is used at transmitter side and Viterbi algorithm is used for decoding at receiver side. The computational complexity of this technique is higher as compared to Alamouti based technique, but STTC also provides more coding gain and diversity gain [40]. At time t , the signal received at n_{th} receiving antenna is given by:

$$r_t^n = \sum_{m=1}^{N_t} h_{nm} s_t^m + \zeta_t^n \quad (3.14)$$

where $h_{nm} = \alpha_{nm} e^{j\theta_{nm}}$ is the channel response between m_{th} transmitting and n_{th} receiving antenna, s_t^m is the signal transmitted at time t from m_{th} transmitting antenna and ζ_t^n is a complex Gaussian random noise variable with zero mean and variance N_o .

At transmitter side, encoder can produce different encoded signals depending on the encoder coefficient set [40]. 4-Phase shift keying (PSK) 4-state STT code with 2 transmitting antennas is shown in Figure 3.3. As an example, Table 1 shows the input signal sequence and the signal which are transmitted using two transmitting antennas system with time-delay diversity. It is clear from Table 1 that the first antenna (Tx 1) transmits the previous value of the second antenna (Tx 2), which in turn transmits the present value, and so on.

Input	0	1	2	1	1	3	2	3
Tx 1	0	0	1	2	1	2	3	2
Tx 2	0	1	2	1	2	3	2	3

Table 3.1: Time-delay diversity with 2 antennas

At time t , the branch metric at receiver side is given by:

$$\sum_{n=1}^{N_r} \left\| r_t^n - \sum_{m=1}^{N_t} h_{nm} \widehat{s}_t^m \right\|^2 \quad (3.15)$$

The Viterbi algorithm is used to calculate the trellis path with lowest metric.

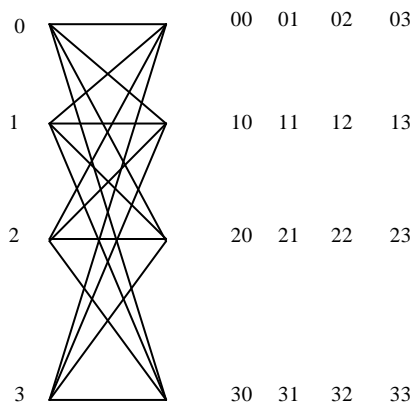


Figure 3.3: 4-PSK 4-state space-time code with two transmitting antennas

3.1.2.3 Orthogonal Space-Time Block Coding (OSTBC) Technique

The concept of OSTBC was introduced by Tarokh et al. [31]. In this technique, it can be observed that the columns of matrix “O” are pair-wise orthogonal:

- For real-valued 2×2 orthogonal set : $O = \begin{bmatrix} s_1 & -s_2 \\ s_2 & s_1 \end{bmatrix}$
- For complex-valued 2×2 orthogonal set : $O = \begin{bmatrix} s_1 & -s_2^* \\ s_2 & s_1^* \end{bmatrix}$

Again we consider a multiple antenna setup with two transmitting and one receiving antenna. At time t_1 , antenna a_1 transmits symbol s_1 and antenna a_2 transmits symbol s_2 . At time t_2 , a_1 transmits symbol $-s_2^*$ and a_2 transmits symbol s_1^* , where * represents the complex conjugate. The received signals r_1 (corresponding to time t_1) and r_2 (corresponding to time t_2) can be expressed as:

$$\begin{bmatrix} r_1 & r_2 \end{bmatrix} = \begin{bmatrix} h_{11} & h_{12} \end{bmatrix} S + \begin{bmatrix} \zeta_1 \\ \zeta_2 \end{bmatrix} \quad (3.16)$$

where $h_{nm} = \alpha_{nm} e^{j\theta_{nm}}$ is the channel response between m_{th} transmitting and n_{th} receiving antenna, $S = \begin{bmatrix} s_1 & -s_2^* \\ s_2 & s_1^* \end{bmatrix}$ and it is assumed that fading is constant across consecutive transmitting symbols. It can be seen that the columns of matrix “S” are pair-wise orthogonal. The received signals can be modified by using the following equation:

$$\begin{bmatrix} \widetilde{y}_1 \\ \widetilde{y}_2 \end{bmatrix} = H^* \begin{bmatrix} r_1 \\ r_2^* \end{bmatrix} \quad (3.17)$$

where $H = \begin{bmatrix} h_{11} & h_{12} \\ h_{12}^* & -h_{11}^* \end{bmatrix}$ is also orthogonal, and $H^*H = (|h_{11}|^2 + |h_{12}|^2) \begin{bmatrix} 1 & 0 \\ 0 & 1 \end{bmatrix}$. The above equation is then divided by $(|h_{11}|^2 + |h_{12}|^2)$ such that:

$$\begin{bmatrix} \widetilde{s}_1 \\ \widetilde{s}_2 \end{bmatrix} = \frac{\begin{bmatrix} \widetilde{y}_1 \\ \widetilde{y}_2 \end{bmatrix}}{(|h_{11}|^2 + |h_{12}|^2)} \quad (3.18)$$

Finally, the signals are estimated by slicing \widetilde{s}_m to the nearest value in the signal constellation:

$$\widehat{s}_m = Q(\widetilde{s}_m) \quad (3.19)$$

It is obvious from Section 3.1.2.1 that Alamouti coding scheme is OSTBC with complex encoded transmitted blocks. Generalised real and complex orthogonal designs are discussed in detail in [31]. For OSTBCs, simple linear processing is required at receiver side, thus the computational complexity is less as compared to STTCs.

3.1.2.4 Space-Time Vector Coding (STVC) Technique

In this technique, CSI is required at both transmitter and receiver side to achieve maximum channel capacity [32]. SVD method is used to convert MIMO channel matrix in to parallel SISO channels with non equal gains [41]. Consider a MIMO system with N_t transmitting and N_r receiving antennas, H is an $N_r \times N_t$ channel matrix. By using SVD, MIMO channel matrix H can be decomposed as:

$$(U, X, V) = SVD(H) \quad (3.20)$$

where U and V are unitary matrices ($UU^* = VV^* = I$) with $N_r \times N_r$, and $N_t \times N_t$ matrix order, respectively, and X is $N_r \times N_t$ diagonal matrix. Before transmitting the encoded signal vector S of order $N_t \times 1$, it is multiplied by matrix V such that $Z = VS$. At receiver, the received signal is first multiplied by U^* as follows:

$$Y = U^*(HZ + \eta) \quad (3.21)$$

H can be replaced by UXV^* and Z by VS , then the above equation will become:

$$Y = U^*(UXV^*VS + \eta) \quad (3.22)$$

$$Y = U^*UXV^*VS + U^*\eta \quad (3.23)$$

$$Y = XS + \zeta \quad (3.24)$$

where $\zeta = U^*\eta$ is statistically identical to η . By using the Zero- Forcing method:

$$G = (X^*X)^{-1}X^* \quad (3.25)$$

The i_{th} transmitted signal can be estimated as follows:

$$s_i = (\underline{G})_i Y \quad (3.26)$$

Finally, the estimated value of the signal is detected by slicing s_i to the nearest value in the signal constellation:

$$\hat{s}_i = Q(s_i) \quad (3.27)$$

3.1.3 Beam-Forming

Multiple antennas are capable of steering lobes and nulls of antenna beam for co-channel interference cancellation in multi-user setup to improve SNR and to reduce delay spread of the channel [33].

The basic principle of beamforming (BF) is shown in the Figure 3.4.

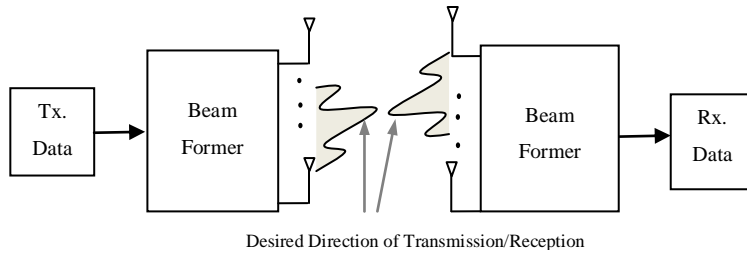


Figure 3.4: A beam-former with N_t transmitting and N_r receiving antennas

There are different types of BFs depending upon the system requirements. A simple delay-sum beam-former is shown in Figure 3.5.

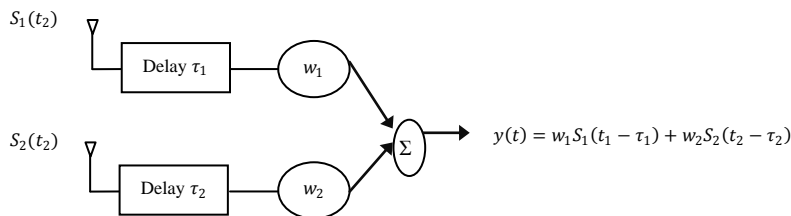


Figure 3.5: A simple delay-sum beamformer

By estimating the direction of arrival (DOA) of waves and by using BF techniques, high directivity can be obtained to improve SNR at the receiver, and in the same way the transmitter power can be concentrated within the desired region. The delay spread of the channel can also be reduced by steering nulls towards dominant reflectors in the signal propagation path.

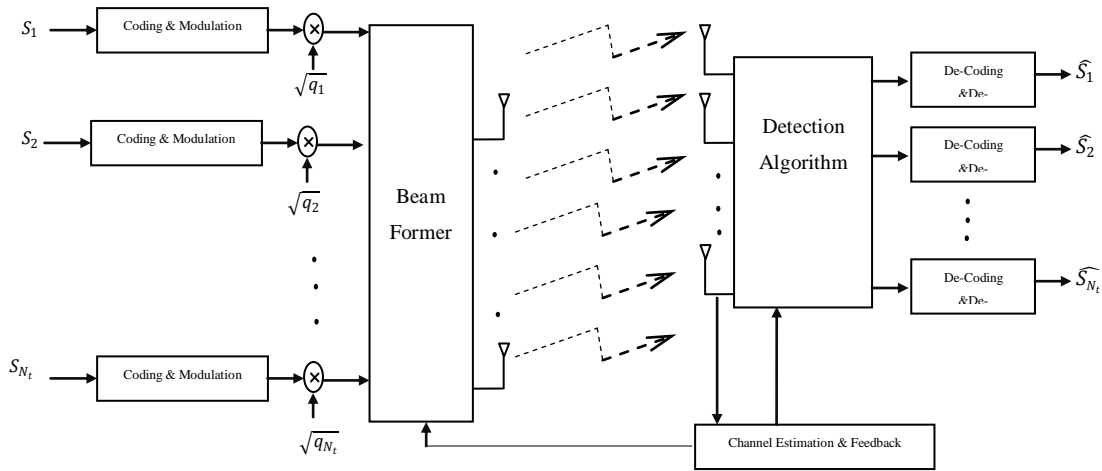


Figure 3.6: V-BLAST MIMO system with beamformer

A linear pre-coder with V-BLAST system architecture is used in [42] to achieve maximum spectrum efficiency. In the proposed scheme, the linear pre-coder is the combination of BF matrix and power allocation matrix. For BF matrix, CSI is required at transmitter side, which is sent to the transmitter using finite rate channel feedback method as shown in Figure 3.6.

A two-direction Eigen BF along with OSTBC was proposed by Zhou & Giannakis [43] to improve BER performance of the system without rate reduction. To reduce co-channel interference cancellation in multi user scenario where each user is equipped with multiple antennas, Alamouti coding scheme along with BF at receiver side is used in [44].

3.1.4 Multi-Functional MIMO Systems

As discussed in the above sections, MIMO techniques can be used for achieving multiplexing gain, diversity gain and beamforming gain. A technique combining STBC and V-BLAST was proposed to obtain diversity gain and multiplexing gain [45]. Another technique combining STBC and beamforming is discussed in [46] to achieve diversity gain and SNR gain due to beamforming. In [34], a multi-functional MIMO system is proposed to improve BER performance, throughput and beamforming (SNR) gain of conventional MIMO systems.

A general multi-functional MIMO system is shown in Figure 3.7 which is capable of combining the advantages of STC, BLAST and beamforming. The system has N_t transmit antenna arrays (AAs) which are sufficiently apart to experience independent fading. The L_{AA} numbers of elements of each AA are spaced at a distance of $\lambda/2$ for achieving beamforming gain. The receiver is equipped with N_r receiving antennas.

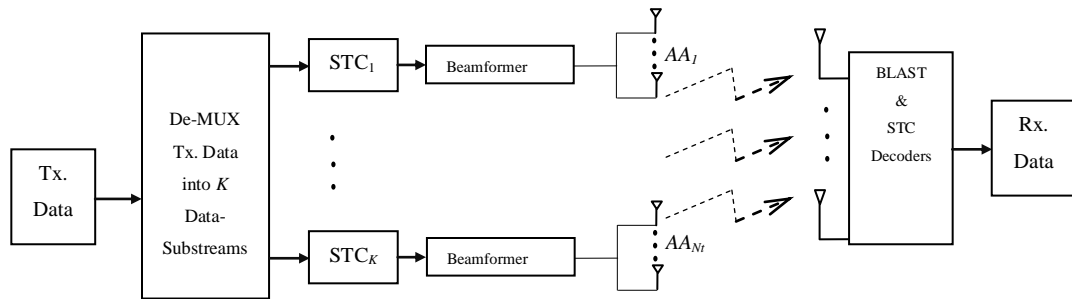


Figure 3.7: Multi-functional MIMO system

The data is transmitted independently from K transmitting nodes to obtain multiplexing gain (K). Before transmission, the data of each node is encoded by STC encoder to improve BER performance. The data is transmitted using the antenna arrays to achieve beamforming gain. At receiver, the combination of BLAST and STC decoders (depending on encoders at transmitter side) can be used to retrieve the transmitted signals.

3.1.5 Virtual MIMO Systems

As introduced in Section 2.2.2, virtual MIMO (V-MIMO) or cooperative/distributive MIMO systems was proposed for energy and physically constrained wireless nodes [21]. V-MIMO systems are distributed in nature because multiple nodes are placed at different physical locations to cooperate with each other. V-MIMO systems may also have problems such as time and frequency asynchronism. Each transmitting node is placed at a different distance from receiving nodes, thus the cooperative transmission may not be time synchronised. Every node also has its own oscillator with different frequency error, thus there are also chances of frequency asynchronism [21]. In addition, the time delay of the virtual MIMO system could be slightly longer than true MIMO system due to local communication involved among the nodes.

3.1.6 MIMO Techniques for WSNs

MIMO techniques have been proposed for WSNs where most nodes operate on batteries and are expected to work for a long period of time. To evaluate the performance of MIMO techniques in energy-limited WSNs, one must take into account of both the circuit and transmission power consumption. In [4], Alamouti coding technique was used for MIMO WSN and the performance

was compared with SISO for the same throughput and BER. The energy efficiency was also compared over different transmission distances with the consideration of circuit and transmission energy consumption. In this technique, local communication was involved among the sensor nodes, which was required for these nodes to cooperate with each other at transmitter as well as receiver side.

A V-BLAST based WSN was proposed in [47] with the concept of virtual MIMO without spatial encoding on transmitting side nodes, thus eradicating local communication on transmitting side as involved in Alamouti coding technique. Both Alamouti coding and V-BLAST based WSN systems mentioned above showed significant energy saving. To simplify the structure of MIMO WSN for energy consumption reduction, a nonlinear MIMO technique was proposed in [48], where real or imaginary part of the complex-valued received signal was considered for further processing which results in simpler receiver architecture at the cost of some information loss.

Another non cooperative STC technique based system with specially designed smart antennas for WSNs [49, 50] was proposed in [51]. By using 2-element switched antenna array, there is no requirement for local communication at transmitter and receiver side which makes the system more energy efficient.

3.2 FOFDM and MIMO-FOFDM

3.2.1 FOFDM

FOFDM is a multi-carrier modulation technique which has the ability to cope with severe channel conditions. The orthogonal sine/cosine bases are generated using IFFT/FFT to carry the

information data. In Section 2.3.1, the basic architecture of FOFDM has been discussed. This section further discusses the structure of FOFDM modulator/demodulator with filter bank structure [52] as shown in Figure 3.8.

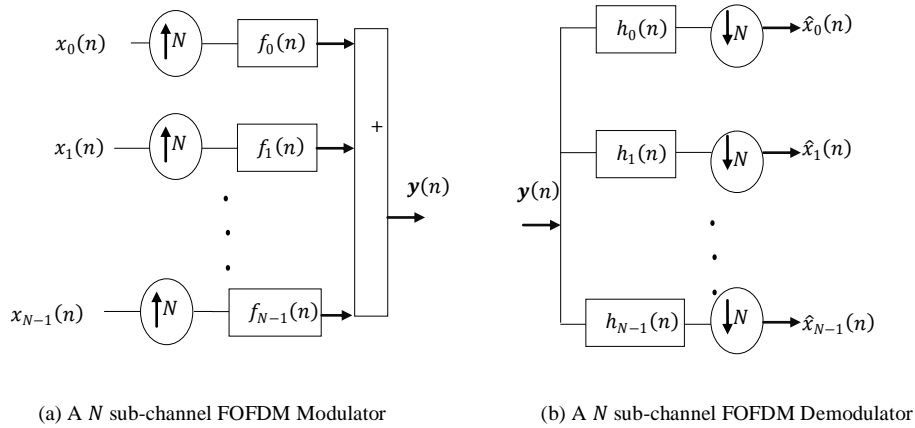


Figure 3.8: FOFDM modulator and demodulator with filter bank structure

The filter impulse can be expressed as:

$$f_i(n) = \sqrt{\frac{1}{N}} \cos\left(\frac{\pi(2n+1)(2i+1)}{4N}\right) \quad (3.28)$$

where $n = 0, 1, 2, 3, \dots, N-1$, and $i = 0, 1, 2, 3, \dots, N-1$.

Each sub-stream is first up sampled and then passes through the filter with impulse response $f_i(n)$. At receiver side, the signal passes through the filters with impulse response $h_i(n) = f_i^*(-n)$ and then down sampled. The training symbols, which are also called pilot tones, are sent using different subcarriers of FOFDM symbols to estimate the CSI associated with the pilot tones as well as sub-channels carrying the data via interpolation techniques [5].

FOFDM can also be used in multi-user cooperative communication systems by assigning subcarrier to different users for overall transmit power reduction [53]. It has been claimed that with two user scenario using FOFDM, the system (as shown in Figure 3.9) becomes 50% more energy efficient as compared to single user scenario.

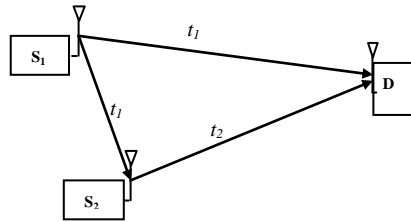


Figure 3.9: Co-operative communication in a multi user scenario using FOFDM

Assume that at time t_1 , source node S_1 transmits some of its data to the destination node D , and remaining data to source node S_2 . At time t_2 , S_2 transmits all of its data along with the remaining data of S_1 by assigning some of the FOFDM subcarriers (for data from S_1) to D . By doing so, the overall transmission power can be reduced significantly when S_1 and S_2 are very close to each other [53].

3.2.2 MIMO-FOFDM

In most of the multi-antenna systems, CSI is required for effective signal processing at the receiver side so that accurate channel estimation can be done using OFDM with an optimal training sequence. MIMO techniques are used with FOFDM (MIMO-FOFDM) to further enhance the system performance. MIMO-FOFDM systems are capable of increasing the channel capacity even under severe channel conditions [5]. The combination of MIMO and FOFDM can also provide two dimensional space-frequency coding (SFC) in space and frequency using individual

subcarriers of an FOFDM symbol [54], or three dimensional coding called space-time-frequency coding (STFC) to achieve larger diversity and coding gains [55, 56].

As already discussed, MIMO techniques can be used for diversity and multiplexing gain, but most of the MIMO techniques have been developed with the assumption of flat fading channel. For broadband frequency selective wireless channel, the combination of MIMO and FOFDM (MIMO-FOFDM) was proposed to mitigate the effect of ISI and ICI [5]. In MIMO techniques, CSI is usually required at transmitter and/or receive side, thus FOFDM is also used in MIMO systems to estimate CSI. A basic structure of MIMO- FOFDM with N_t transmitting antennas and N_r receiving antennas is shown in Figure3.10.

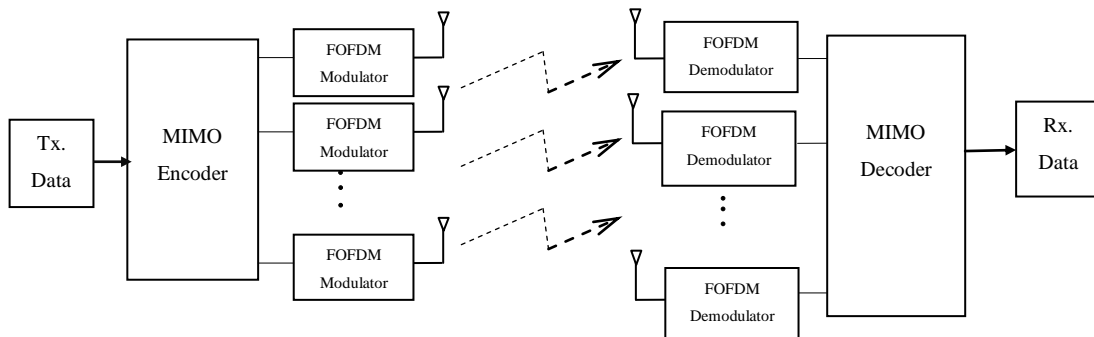


Figure 3.10: MIMO-FOFDM system with N_t transmitting and N_r receiving antennas

To achieve high data rate for broadband frequency selective channel, V-BLAST architecture with FOFDM was proposed in [57] with N_t transmitting antennas, N_r receiving antennas, and N subcarriers which can be represented as:

$$\mathbf{Rec} = \begin{bmatrix} \mathbf{H}_{11} & \mathbf{H}_{12} & \mathbf{H}_{13} & \cdots & \mathbf{H}_{1N_t} \\ \mathbf{H}_{21} & \mathbf{H}_{22} & \mathbf{H}_{23} & \cdots & \mathbf{H}_{2N_t} \\ \vdots & \vdots & \vdots & \cdots & \vdots \\ \mathbf{H}_{N_r,1} & \mathbf{H}_{N_r,1} & \mathbf{H}_{N_r,1} & \cdots & \mathbf{H}_{N_r,N_t} \end{bmatrix} \begin{bmatrix} \mathbf{X}_1 \\ \mathbf{X}_2 \\ \vdots \\ \mathbf{X}_{N_t} \end{bmatrix} + \begin{bmatrix} \boldsymbol{\zeta}_1 \\ \boldsymbol{\zeta}_2 \\ \vdots \\ \boldsymbol{\zeta}_{N_r} \end{bmatrix} \quad (3.29)$$

where \mathbf{H}_{nm} is a $N \times N$ diagonal matrix corresponding to SISO frequency response of all the subcarriers between m_{th} transmitting and j_{th} receiving antenna, \mathbf{X}_m is the OFDM symbol transmitted from m_{th} transmitting antenna, and $\boldsymbol{\zeta}_j$ is the additive white Gaussian noise (AWGN) vector. From the above equation, it can be observed that corresponding to each subcarrier, there is a narrow band $N_r \times N_t$ V-BLAST system. Hence, the detection of V-BLAST-FOFDM system can be done using V-BLAST detection algorithm (as discussed in Section 3.1.1.2) on each subcarrier individually.

In [54], STCs are used across FOFDM tones for developing SFC to achieve full diversity for broadband frequency selective channel. It is shown that Alamouti scheme fails to exploit the frequency diversity available in frequency selective channels. STFCs were proposed in which the system is converted into group STF (GSTF) systems. Both OSTBCs and orthogonal STTCs (OSTTCs) along with FOFDM are used to achieve maximum coding gain and low complexity decoding for frequency selective channels [54].

STFCs can achieve diversity gain equal to $(N_t N_r L \tau)$ where L is the number of propagation paths and τ is the rank of channel temporal correlation matrix [58]. With N OFDM subcarriers and K consecutive FOFDM blocks, the STF code word can be expressed as a $KN \times N_t$ matrix:

$$\mathbf{C} = [\mathbf{C}_1^T \quad \mathbf{C}_2^T \quad \cdots \quad \mathbf{C}_K^T]^T \quad (3.30)$$

where T is for transpose of matrix. The channel symbol matrix \mathbf{C}_k is given by:

$$\mathbf{C}_k = \begin{bmatrix} c_1^k(0) & c_2^k(0) & \cdots & c_{N_t}^k(0) \\ \vdots & \vdots & \vdots & \vdots \\ c_1^k(N-1) & c_2^k(N-1) & \cdots & c_{N_t}^k(N-1) \end{bmatrix} \quad (3.31)$$

where $c_m^k(i)$ is the channel symbol transmitted over i_{th} subcarrier by transmitting antenna m in the k_{th} FOFDM block. To obtain maximum coding gain, STFCs were proposed with combination of STTC and rotated constellation technique [56].

3.3 WOFDM and MIMO-WOFDM

3.3.1 WOFDM

WOFDM is another multi-carrier modulation with less computational complexity as compared to FOFDM [59]. WOFDM is also more bandwidth efficient because no cyclic prefix is used. This technique is a strong candidate for high data rate communication systems [6]. The orthogonal wavelet bases are generated using IDWT/DWT. WOFDM as an alternative to Fourier based OFDM (FOFDM) was first proposed by Lindsey [60] and theoretical discussions were carried out regarding power spectral density and bandwidth efficiency of WOFDM. The ISI and inter carrier interference (ICI) analysis of WOFDM and FOFDM has been carried out by Negash & Nikookar [61] with asymmetric multi-level QMF structure. The ISI and ICI of WOFDM were less as compared to FOFDM. These results were further verified by Jamin & Mahonen [62] who showed that WOFDM is a feasible alternative to FOFDM. BER performance of QPSK-WOFDM with standard wavelets and QPSK-FOFDM were also investigated in the presence of frequency offset and

phase noise. Both techniques were found to be equally affected by frequency offset and phase noise [63].

WOFDM provides flexibility for designer to design new waveforms according to the communication channel and/or communication system requirements. New wavelet bases were designed to reduce timing synchronization error and the performance was compared with other wavelet families. Simulation results have shown better BER performance with new optimal filter design even in the presence of timing offset [64]. By using time-frequency localisation property of wavelets, new optimal maximally frequency selective wavelet bases for reconfigurable communication system were also designed to utilise unoccupied time-frequency gap of licensed users efficiently [65].

The orthonormal wavelets can be generated using symmetric or asymmetric multi-stage tree structure of QMF bank. By using symmetric structure, the orthonormal wavelets are given by:

$$f_i(n) = \prod_{p=1}^P \sqrt{2} t_{i,p} \left(\frac{n}{2^{p-1}} \right) \quad (3.32)$$

where \prod represents the convolution operation, P is the number of levels of this structure, $i \in \{0, 1, 2, 3, \dots, 2^P - 1\}$, $t_{k,p}(n) \in \{f_l(n), f_h(n)\}$ is the filter impulse response corresponding to the i_{th} sub-channel at p_{th} level, and $f_l(n)$ and $f_h(n)$ are the impulse responses of lowpass, and highpass filters, respectively, for perfect reconstruction QMF bank. The highpass filter can be derived from the lowpass filter by the relation, $f_h(n) = (-1)^n f_l(U - 1 - n)$, where U is the length of the filter [66]. The multi-level symmetric synthesis and analysis side QMF bank structure is shown in

Figure 3.11. The equivalent structure using noble identities of WOFDM modulator and demodulator is shown in Figure 3.12. The output $y(n)$ of WOFDM modulator can be expressed as:

$$y(n) = \sum_{i=0}^{2^p-1} \sum_m x_i(m) f_i(n - 2^p m) \quad (3.33)$$

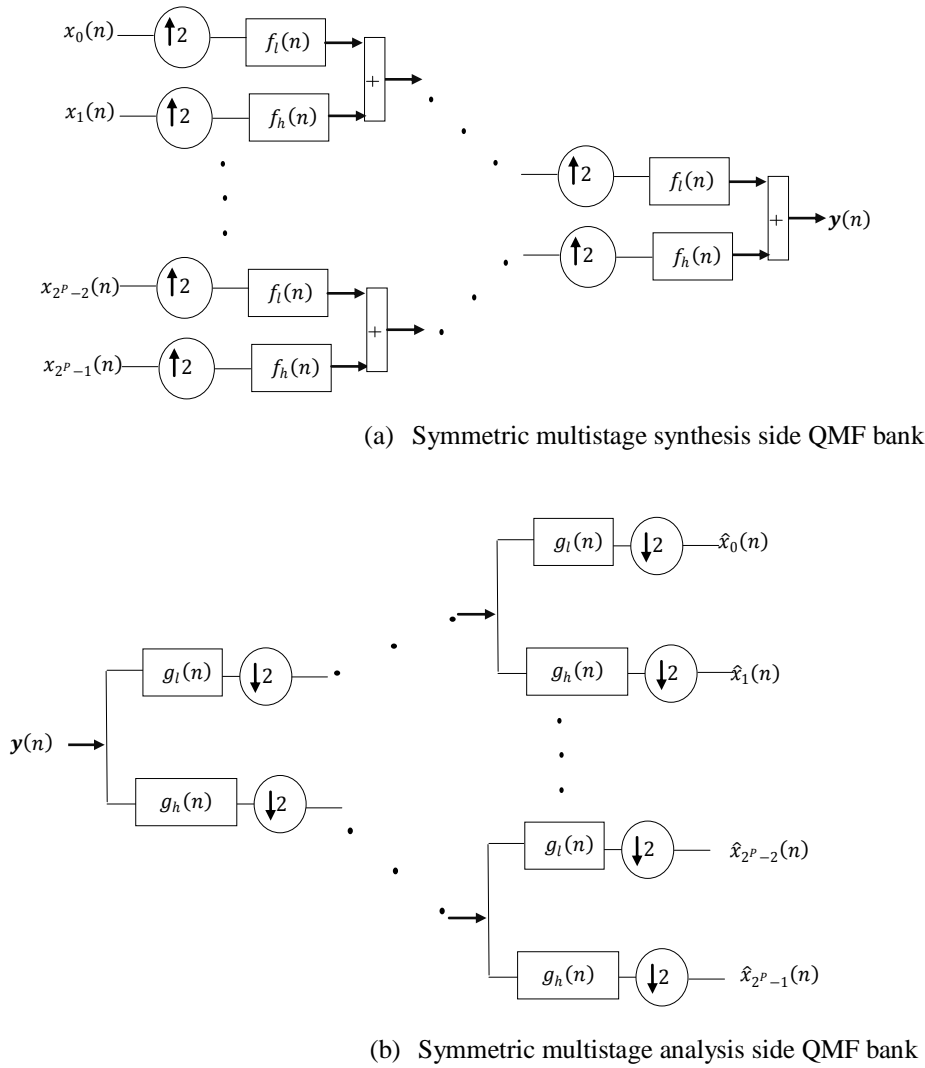


Figure 3.11: WOFDM modulator and demodulator using symmetric QMF filter bank structure

where $x_i(n)$ is i_{th} sub-channel input of WOFDM modulator. For WOFDM demodulation, the orthonormal wavelet bases are generated using symmetric analysis side QMF bank as follows:

$$h_i(n) = \prod_{p=1}^P \frac{1}{\sqrt{2}} u_{i,p} \left(\frac{n}{2^{p-1}} \right) \quad (3.34)$$

where $u_{i,p}(n) \in \{g_{l(n)}, g_{h(n)}\}$ is the filter impulse response corresponding to i_{th} sub-channel at p_{th} level, and $g_{l(n)}$ and $g_{h(n)}$ are time reversals of $f_{l(n)}$ and $f_{h(n)}$, respectively [23].

In the WOFDM demodulator, the detected signal stream is first filtered by sub-channel impulse response $h_k(n)$ and then down-sampled by 2^P .

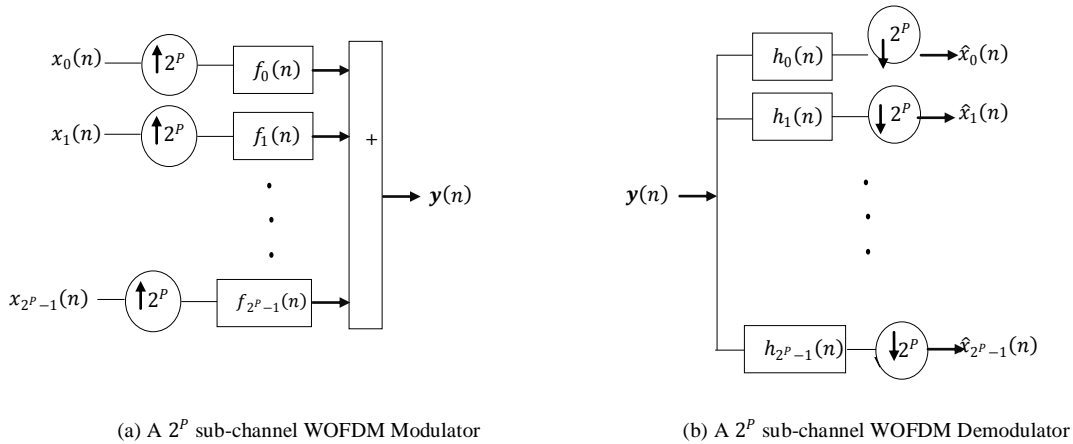


Figure 3.12: Equivalent structure of WOFDM modulator and demodulator using noble identities

3.3.2 MIMO-WOFDM

WOFDM is an attractive modulation technique for MIMO wireless networks. The BER performance of a WOFDM V-BLAST MIMO system was investigated in [23]. The performance of this system using different detection algorithms was also investigated in [67]. A basic

structure of MIMO-WOFDM with N_t transmitting antennas and N_r receiving antennas is shown in Figure 3.13.

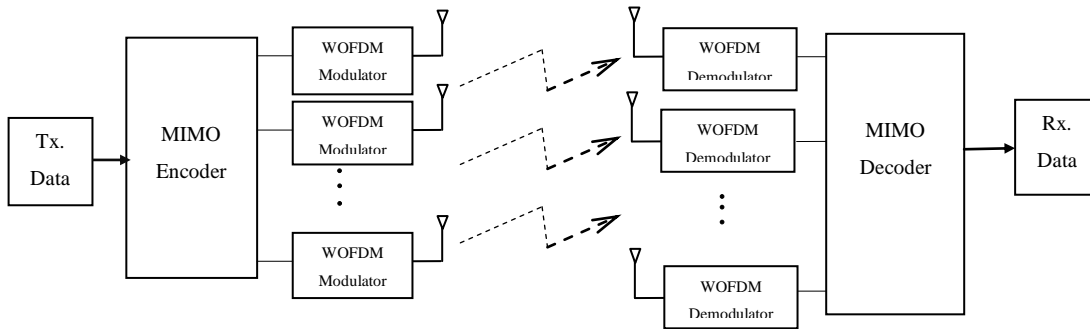


Figure 3.13. MIMO-WOFDM system with N_t transmitting and N_r receiving antennas

Further discussion about MIMO-WOFDM would follow in the next chapter.

Chapter 4

Virtual MIMO WSN

With the concept of Virtual MIMO using V-BLAST technique, there is no need for spatial encoding on transmitting side nodes, thus eradicating their needs for local communication. It also exploits the multi-antenna setup for effective signal processing at the receiver to estimate the transmitted signals. It can boost the channel capacity to improve the data rate of individual sensors, or increase the number of supported sensors in the system.

In this chapter, we analyse the performance of WSN with Virtual MIMO data sensing nodes (DSNs) at transmitting side, and a data gathering node (DGN) with either True or Virtual MIMO architecture using V-BLAST signal processing technique. BER, total energy efficiency (analogue and digital), and spectral efficiency of BPSK-WOFDM, BPSK-FOFDM, Amplitude Shift Keying (ASK)-WOFDM, ASK-FOFDM, M -ary Quadrature-Amplitude-Modulation (QAM), M -ary Differential Phase Shift Keying (DPSK) and M -ary Offset Phase Shift Keying (OPSK) are investigated. We have also considered the total time delay of the both systems.

4.1 True MIMO DGN

4.1.1 System Model

We consider a wireless communication link between N_t DSNs serving as one Virtual MIMO node, and one DGN with N_r antennas as shown in Figure 4.1.

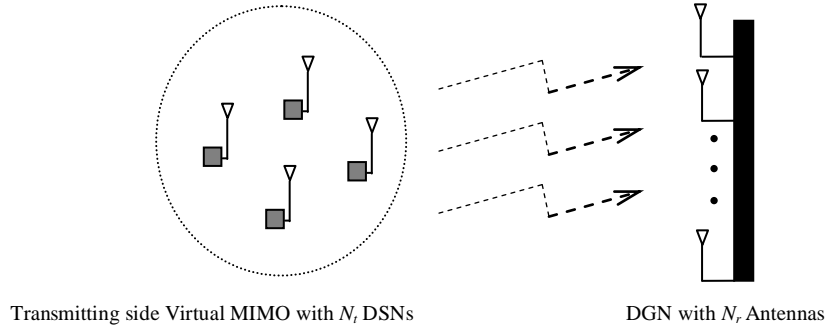


Figure 4.1: Communication between DSNs (Virtual MIMO node) and DGN

In this model, V-BLAST signal processing technique is used at the receiver side with the assumption that the DGN, typically a more powerful node serving as a data sink, has no resource (e.g. battery life, physical dimension) constraints, unlike the DSNs. Moreover, no local communication and processing are essential among DSNs.

The communication channel is assumed to be flat (non-frequency selective) fading channel. This assumption is reasonable since it is known that flat fading channel entails the delay spread of the channel to be smaller than the symbol period, or in other words, the channel bandwidth should be larger than the signal bandwidth, which is often the case in WSN. In IEEE 802.15.4 standard for WSN, the channel bandwidth is 2 MHz at 2.4 GHz, and the maximum bit rate is 250 kbps. Under a possibly worst-case signal-to-noise ratio of 0 dB, where signal power and noise power are equal, it can be found by Shannon's capacity theorem that the signal bandwidth is only 0.25 MHz, or 1/8 of the channel bandwidth. Therefore, a flat-fading channel can be a reasonable assumption.

Consider N_t DSNs transmitting their data simultaneously over a flat fading MIMO channel. The signal received at DGN with N_r antennas is then expressed as:

$$Rec_T = HS + \zeta \quad (4.1)$$

where Rec_T is an $N_r \times I$ vector, S is $N_t \times I$ vector, ζ is an $N_r \times I$ noise vector whose elements are complex Gaussian random variables with zero mean and variance N_o , and H is an $N_r \times N_t$ channel matrix. It is assumed in this thesis that $N_t \leq N_r$ [47].

At each DSN, a serial-to-parallel converter is used to form the input for WOFDM modulator. Every k_{th} input is first up-sampled by 2^P and then filtered by sub-channel impulse response $f_k(n)$. Received signals are detected using QR decomposition detection algorithm [38]. By using the steps outlined in Section A.3 of Chapter 3, the detected signal $\hat{s}_i = \frac{z_i}{r_{ii}}$, corresponding to each receiving antenna of DGN, is demodulated using WOFDM demodulator. In the WOFDM demodulator, the detected signal stream is first filtered by sub-channel impulse response $h_k(n)$ and then down-sampled by 2^P . For BPSK-WOFDM system, at each DSN, the bit stream is first modulated using BPSK modulator and then fed to a serial-to-parallel converter to form the input for WOFDM modulator. Similarly for BPSK-FOFDM system, at each DSN, the bit stream is first modulated using BPSK modulator and then fed to a serial-to-parallel converter to form the input for FOFDM modulator.

4.1.2 Energy Consumption Analysis

In [4] and [47], the energy consumed in baseband (Digital) blocks were neglected to keep the energy consumption model simple. In this work, however, we have also computed the energy

consumed by baseband (Digital) blocks. The DGN (often a more powerful node as mentioned in Section 4.1.1) is considered to have no energy constraints unlike the DSNs [47].

4.1.2.1 RF (Analogue) Energy Consumption

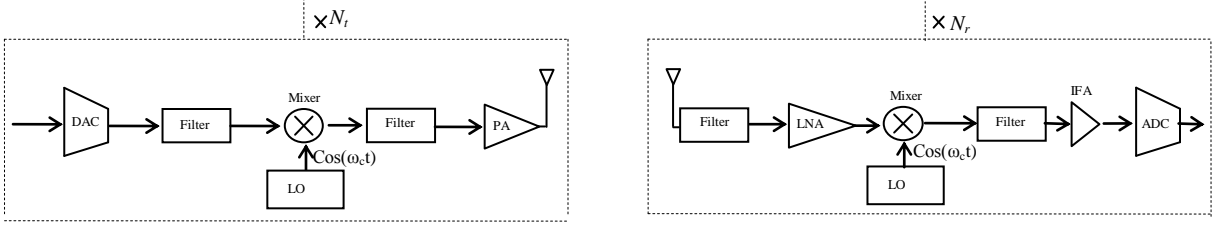
The total average power consumption along the signal path can be divided into two main components: power consumption of all power amplifiers P_{PA} , and power consumption of all other circuit blocks P_c [68]. As in [47], we assume that the energy consumed by power amplifiers is linearly dependant on the transmit power P_{out} :

$$P_{PA} = (1 + \alpha)P_{out} \quad (4.2)$$

where $\alpha = \beta/\zeta$ with ζ being the drain efficiency of the RF power amplifier and β being the PAPR [69, 70], which depends on the modulation scheme and associated constellation size [47]. P_{out} can be calculated according to link budget relationship [71, 72] as follows:

$$P_{out} = \bar{E}_b R_b \frac{(4\pi d)^2}{G_t G_r \lambda^2} M_l N_f \quad (4.3)$$

where \bar{E}_b is the required energy per bit for a given BER (\bar{P}_b) at DGN, R_b is the bit rate of the system, d is the distance between each DSN and DGN, G_t and G_r are the antenna gains of the transmitter, and receiver, respectively, λ is the carrier wavelength, M_l is the link margin compensating the hardware process variations and other additive background noise or interference, and N_f is the receiver noise figure.



(a) Transmitter circuit blocks (analogue)

(b) Receiver circuit blocks (analogue)

Figure 4.2: Transmitter and receiver architecture for ASK-WOFDM and BPSK-WOFDM

From Figure 2.10 in Chapter 2, it can be observed that WOFDM has only real value samples while FOFDM has both real and imaginary value samples. Due to this reason, RF section of ASK-FOFDM and BPSK-FOFDM as well as M -ary QAM, M -ary DPSK and M -ary OPSK which shares a similar transmitter and receiver architecture, is potentially more complex as compared to that of ASK-WOFDM and BPSK-WOFDM.

The total power consumption in all circuit blocks with N_t transmitter circuits and N_r receiver circuits having ASK-WOFDM or BPSK-WOFDM transmitter and receiver architecture as shown in Figure 4.2, can be calculated as:

$$P_c \approx N_t (P_{DAC} + P_{mix} + (2 \times P_{fil}) + P_{LO}) + N_r (P_{LNA} + P_{mix} + (2 \times P_{fil}) + P_{LO} + P_{IFA} + P_{ADC}) \quad (4.4)$$

where P_{DAC} , P_{mix} , P_{fil} , P_{LO} , P_{LNA} , P_{IFA} and P_{ADC} are the power consumption values for the digital-to-analogue convertor (DAC), mixer, filter, local oscillator, low-noise amplifier (LNA),

amplifier, and analogue-to-digital convertor (ADC), respectively. In addition, the energy models developed in [68] can be used to estimate the values for P_{DAC} and P_{ADC} .

The total power consumption in all circuit blocks with N_t transmitter circuits and N_r receiver circuits having In-Phase/Quadrature-Phase (ASK-FOFDM, BPSK-FOFDM, QAM, DPSK and OPSK) transmitter and receiver architecture as shown in Figure 4.3, can be calculated as:

$$P_c \approx N_t \left((2 \times P_{DAC}) + (3 \times P_{fil}) + P_{LO} + P_{PS} + P_{Add} \right) + N_r \left(P_{LNA} + (2 \times P_{mix}) + (3 \times P_{fil}) + P_{LO} + P_{PS} + (2 \times P_{IFA}) + (2 \times P_{ADC}) \right) \quad (4.5)$$

where P_{PS} and P_{Add} are the power consumption values for phase shifter, and adder respectively.

The total energy consumption per bit can then be obtained as follows:

$$E_b = \frac{P_{PA} + P_c}{R_b} \quad (4.6)$$

where R_b is the data rate in bits per second. The total energy per bit per node (RF section) can be calculated using the following equation:

$$E_{b_Analog} = \frac{E_b}{N_t + N_r} \quad (4.7)$$

The energy efficiency (EE) can be calculated by taking the inverse of equation (4.7). Compared to the transmitter and receiver architecture for ASK-WOFDM and BPSK-WOFDM in Figure 4.2, there is an additional DAC, filter, mixer, phase shifter, adder at transmitter side, and an

additional mixer, filter, IFA, ADC at receiver side for In-Phase/Quadrature-Phase modulation techniques.

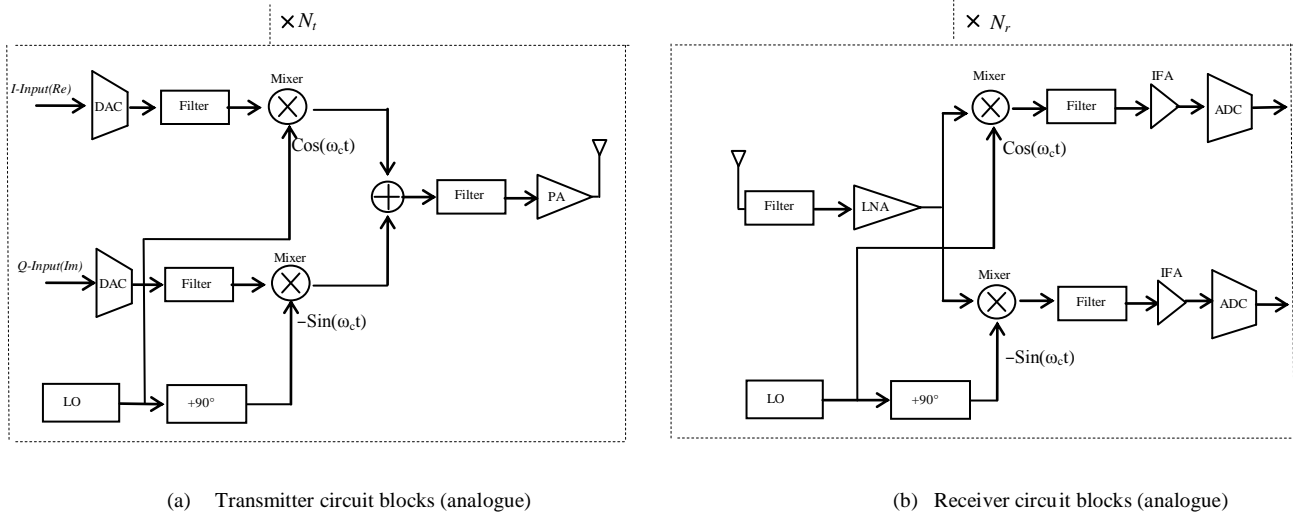


Figure 4.3: Transmitter and receiver architecture (In-Phase/Quadrature-Phase) for ASK-FOFDM, BPSK-FOFDM, QAM, DPSK, and OPSK (analogue)

4.1.2.2 Base Band (Digital) Energy Consumption

The number of required central processing unit (CPU) cycles for base band processing is estimated by using the Odyssey prediction model [72]. To calculate the base band energy consumption of a block, energy consumption per CPU cycle value is multiplied by the estimated number of CPU cycles. For DSN, the TelosB mote [73] energy consumption per CPU cycle value is used [74]. An FPGA (Xilinx XC2V6000-6) is used [75] for True MIMO DGN base band energy consumption. The total energy consumption per bit per antenna by base band (Digital) blocks can be calculated as:

$$E_{b_Digital} = \left(\frac{N_t E_{Mod} + N_r E_{Dmod} + E_{Det}}{N_t + N_r} \right) \quad (4.8)$$

where E_{Mod} , E_{Dmod} and E_{Det} are the energy consumption per bit values for modulator, demodulator and detection algorithm respectively.

4.1.3 Spectral Efficiency

The spectral efficiency (SE) of a MIMO system without the knowledge of the channel at the transmitter can be calculated as [76]:

$$S_E = \sum_{j=1}^{N_t} \log_2 \left(1 + \frac{E_b R \gamma_j}{N_o B N_t} \right) \quad (4.9)$$

where γ_j is the eigenvalue of $H_n H_n^H$, $H_n = \frac{\sqrt{N_r}}{\|H\|_{Forbenius}} H$ is the normalised channel matrix [77], and $(.)^H$ denotes Hermitian transpose.

4.1.4 Time Delay

The total time delay (T_{T-MIMO}) of MIMO system with N_t DSNs and one DGN with N_r antennas can be calculated as the sum of transmission delay (T_{tr_t}), propagation delay (T_{pr_t}) and processing delay (T_{pc_t}).

$$T_{T-MIMO} = T_{tr_t} + T_{pr_t} + T_{pc_t} \quad (4.10)$$

T_{tr_t} is given by:

$$T_{tr_t} = T_s \left(\frac{\sum_{i=1}^{N_t} M_i}{b_n} \right) \quad (4.11)$$

where M_i is the number of bits transmitted by each node i , b_n is the constellation size (bits per symbol) used at transmitter side, $T_s \approx \frac{1}{B}$ is the symbol duration, and B is the transmission bandwidth.

T_{pr_t} is given by:

$$T_{pr_t} = \frac{d}{c} \quad (4.12)$$

where c is the speed of light. T_{pc_t} is given by:

$$T_{pc_t} = T_{Mod} + T_{Dmod_t} + T_{Det_t} \quad (4.13)$$

where T_{Mod} , T_{Dmod_t} , and T_{Det_t} are the processing time values for modulator, demodulator, and detection algorithm respectively. Each block processing time is calculated by dividing the estimated CPU cycles (as mentioned in Section 4.1.2.2) with the processing speed of the hardware. The processing speed of TelosB mote [74] is used for T_{Mod} , while that of Xilinx XC2V6000-6 [76] is used for T_{Dmod_t} and T_{Det_t} .

4.2 Virtual MIMO DGN

4.2.1 System Model

We consider a wireless communication link between N_t DSNs serving as one Virtual MIMO transmitting side node, and one Virtual MIMO receiving side node which consists of one DGN and $N_r - 1$ data assisting nodes (DANs), each with one antenna as shown in Figure 4.4. The Virtual MIMO transmitter side architecture allows the WSN to enjoy the performance benefits brought by MIMO's spatial diversity without having the sensor nodes to carry multiple antennas, while potential applications of Virtual MIMO receiver side architecture may include cooperative cluster head [77] and virtual broker [78] for WSN-based publish/subscribe systems.

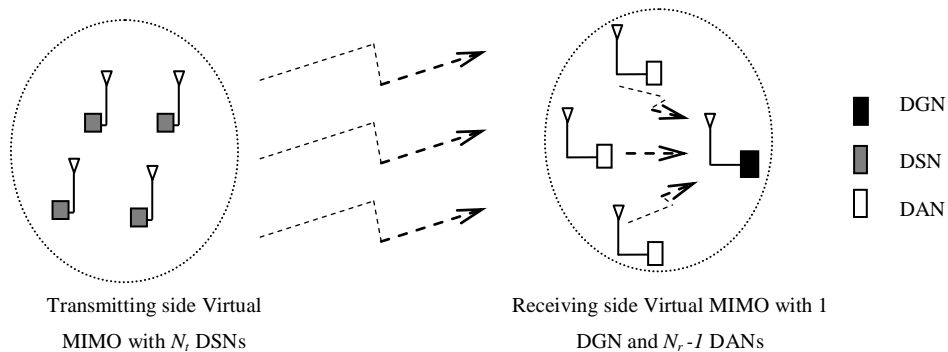


Figure 4.4: Communication between Transmitting and Receiving Side Virtual MIMO Nodes

V-BLAST signal processing is performed at the receiving side by only the DGN with the assumption that it can cope with more computational complexity than its DANs. Moreover, no local communication and processing are essential among the DSNs. It is assumed that N_t DSNs are transmitting their data simultaneously over a flat fading MIMO channel to DGN (referred to as long-haul communications [4, 47]). In addition, there are $N_r - 1$ DANs in close proximity of DGN to form one virtual receiving node of size N_r , including the DGN itself. All DANs transmit

their data using time-division-multiple access (TDMA) to DGN (referred to as receiver side local communication) to form received signal vector Rec_V as shown in the following:

$$Rec_V = HS + \zeta \quad (4.14)$$

where Rec_V is an $N_r \times 1$ vector, S is $N_t \times 1$ vector, ζ is an $N_r \times 1$ noise vector whose elements are complex Gaussian random variables with zero mean and variance N_o , and H is an $N_r \times N_t$ channel matrix.

At each DSN, a serial-to-parallel converter is used to form the input for WOFDM modulator. Every k_{th} input is first up-sampled by 2^P and then filtered by sub-channel impulse response $f_k(n)$. Received signal vectors at DGN are detected using QR decomposition detection algorithm [38]. By using the steps outlined in Section A.3 of Chapter 3, the detected signal $\hat{s}_i = \frac{z_i}{r_{ii}}$, corresponding to each receiving antenna of DGN, is demodulated using WOFDM demodulator. In the WOFDM demodulator, the detected signal stream is first filtered by sub-channel impulse response $h_k(n)$ and then down-sampled by 2^P . For BPSK-WOFDM system, at each DSN, the bit stream is first modulated using BPSK modulator and then fed to a serial-to-parallel converter to form the input for WOFDM modulator. Similarly for BPSK-FOFDM system, at each DSN, the bit stream is first modulated using BPSK modulator and then fed to a serial-to-parallel converter to form the input for FOFDM modulator.

4.2.2 Energy Consumption Analysis

4.2.2.1 RF (Analogue) Energy Consumption

The total energy consumption in RF section is due to long-haul communication (from DSNs to receiving side DANs and DGN itself) and receiver side local communication (from DANs to DGN). The total average power consumption along the signal path for long-haul can be divided into two main components: power consumption of all power amplifiers P_{PA}^L , and power consumption of all other circuit blocks P_c^L [4]. P_{PA}^L can be calculated by replacing P_{PA} , and P_{out} in Equation (4.2), with P_{PA}^L , and P_{out}^L , respectively.

$$P_{PA}^L = (1 + \alpha)P_{out}^L \quad (4.15)$$

P_{out}^L can be calculated by replacing \bar{E}_b , and d in Equation (4.3), with \bar{E}_b^L , and d^L , respectively.

$$P_{out}^L = \bar{E}_b^L R_b \frac{(4\pi d^L)^2}{G_t G_r \lambda^2} M_l N_f \quad (4.16)$$

where \bar{E}_b^L is the required energy per bit for a given BER \bar{P}_b^L at receiver side and d^L is the distance between the transmitting and receiving side clusters.

By modifying Equation (4.4), the power consumption in all circuit blocks for long-haul communication (P_c^L) with N_t transmitter circuits and N_r receiver circuits using ASK-WOFDM or BPSK-WOFDM transmitter and receiver architectures shown in Figure 4.2, can be calculated as:

$$P_c^L \approx N_t [P_{DAC} + P_{mix} + (2 \times P_{fil}) + P_{LO}] + N_r [P_{LNA} + P_{mix} + (2 \times P_{fil}) + P_{LO} + P_{IFA} + P_{ADC}] \quad (4.17)$$

By modifying Equation (4.5), the power consumption in all circuit blocks for long-haul communication (P_c^L) with N_t transmitter circuits and N_r receiver circuits using In-Phase/Quadrature-Phase (ASK-FOFDM, BPSK-FOFDM, QAM, DPSK and OPSK) transmitter and receiver architectures shown in Figure 4.3, can be calculated as:

$$P_c^L \approx N_t [(2 \times P_{DAC}) + (2 \times P_{mix}) + (3 \times P_{fil}) + P_{LO} + P_{PS} + P_{Add}] + N_r [P_{LNA} + (2 \times P_{mix}) + (3 \times P_{fil}) + P_{LO} + P_{PS} + (2 \times P_{IFA}) + (2 \times P_{ADC})] \quad (4.18)$$

The total energy consumption per bit for long-haul communication can then be obtained as follows:

$$E_b^L = \frac{P_{PA}^L + P_c^L}{R_b} \quad (4.19)$$

where R_b is the data rate in bits per second (bps). The total energy consumption per bit for local communication can be obtained as follows:

$$E_b^l = \frac{P_{PA}^l + P_c^l}{R_{bi}} \quad (4.20)$$

P_{PA}^l is the power of each amplifier of DAN during local communication and its value can be obtained by Equations (4.15) and (4.16) and substituting the parameters $\bar{E}_b^L, R_b, G_t, G_r, d^L$ with

\bar{E}_b^l , R_{bi} , G_{ti} , G_{ri} , d^l , respectively, where \bar{E}_b^l is the required energy per bit for a given BER \bar{P}_b^l at DGN side, R_{bi} is the bit rate of each individual node i , d^l ($\ll d^L$) is the distance between DAN and DGN, G_{ti} is the antenna gain of each DAN, and G_{ri} is the antenna gain of DGN. Circuit power consumption for local communication P_c^l can be calculated using Equations (4.17) and (4.18) by replacing $N_r = N_t = 1$. The total energy per bit per node (RF section) can be calculated as follows:

$$E_{b_Analog} = \frac{E_b^l + (N_r - 1)E_b^l}{N_t + N_r} \quad (4.21)$$

The energy efficiency (EE) can be calculated by taking the inverse of Equation (4.21).

4.2.2.2 Base Band (Digital) Energy Consumption

Similarly for this system model, CPU cycles are estimated with the Odyssey prediction model [72] as discussed in Section 4.1.2.2. To calculate the base band energy consumption of a DSN, DAN and DGN, the TelosB mote [73] energy consumption per CPU cycle value is used [74]. The total energy consumption per bit per node by base band signal processing blocks can be calculated using Equation (4.8).

4.2.3 Spectral Efficiency

The spectral efficiency (SE) of this system model is approximately the same as for True MIMO DGN system architecture because for local communication, TDMA is used and the upper bound for SE of TDMA based communication is unity [81].

4.2.4 Time Delay

The total time delay (T_{V-MIMO}) of virtual MIMO system with N_t DSNs, $N_r - 1$ DANs and one DGN each with one antenna, can be calculated as the sum of transmission delay (T_{tr}), propagation delay (T_{pr}) and processing delay (T_{pc}).

$$T_{V-MIMO} = T_{tr} + T_{pr} + T_{pc} \quad (4.22)$$

T_{tr} is given by:

$$T_{tr} = T_s \left(\frac{\sum_{i=1}^{N_t} M_i}{b_n} + \sum_{j=1}^{N_r-1} \frac{m_r M_s}{b_j^r} \right) \quad (4.23)$$

where M_i is the number of bits transmitted by each node i , $M_s = \sum_{i=1}^{N_t} \frac{M_i}{b_n}$ is the total number of symbols received, b_n , and b_j^r , are the constellation sizes (bits per symbol) used at transmitter side, and receiver side local communication, respectively, m_r represents the number of bits after quantisation of each symbol received at receiver side relay nodes, $T_s \approx \frac{1}{B}$ is the symbol duration, and B is the transmission bandwidth. T_{pr} is given by:

$$T_{pr} = \frac{d^L}{c} + \frac{d^l}{c} \quad (4.24)$$

where c is the speed of light, and d^L and d^l as defined for Equation (4.16), and Equation (4.20), respectively. T_{pc} is given by:

$$T_{pc} = T_{Mod} + T_{Dmod} + T_{Det} \quad (4.25)$$

where T_{Mod} , T_{Dmod} and T_{Det} are the processing time values for modulator, demodulator, and detection algorithm, respectively.

4.3 Evaluation Results

Simulations were carried out to investigate performances of 16-DPSK, 16-QAM, 16-OPSK, ASK-16FOFDM (without cyclic prefix), ASK-16WOFDM (4-level symmetric with Haar filter coefficients), BPSK-16FOFDM, and BPSK-16WOFDM with two system models as discussed in Sections 4.1.1 and 4.2.1. As mentioned in Section 2.3.3, since no cyclic prefix is used in WOFDM, FOFDM is similarly used without cyclic prefix for a fair comparison.

Matlab/Simulink is used as the simulation platform as it is one of the most widely used tools for physical layer modelling of wireless systems with many digital communication blocks and analysing tools available for evaluating system performance. In addition, C and high definition languages (HDL) can be generated directly from Matlab/Simulink code for real hardware implementation.

The information source of each DSN generates data at a rate of 250 kbps according to IEEE 802.15.4-2009 standard for WSNs. Such a data rate has been used for image transmission over WSN [82]. The typical transmission range of IEEE 802.15.4 based radio transceivers is 10–20 m, with a nominal maximum range of about 100 m in clear line-of-sight scenarios. At each DSN, information bits are modulated into a symbol stream using 16-DPSK, 16-QAM, 16-OPSK, ASK-16FOFDM, ASK-16WOFDM, BPSK-16FOFDM, and BPSK-16WOFDM. As in [81], the channel

response matrix H is assumed to be known at DGN to detect the received signals using QR decomposition detection algorithm. All performance graphs are plotted with their 95% confidence intervals.

BER performance vs. bit-energy to noise-spectral density ratio $\frac{E_b}{N_o}$ graphs of all above mentioned modulation techniques with two different system models are shown in Figure 4.5 and 4.6. The distance between the transmitting and receiving clusters is 20 m. The results show that OFDM (including ASK-FOFDM, ASK-WOFDM, BPSK-FOFDM, and BPSK-WOFDM) and OPSK based systems have better BER performance than QAM and DPSK because as an increase in dimension set size ($M = 2^b$ where b is the number of bits) decreases the probability of wrong detection at receiver side, which improves the M -ary signalling performance. BER performance between ASK-FOFDM and ASK-16WOFDM, and that between BPSK-16FOFDM and BPSK-16WOFDM are found to be comparable due to their equivalent filter bank structures. The pair BPSK-16FOFDM and BPSK-16WOFDM is also found to perform better than ASK-16FOFDM and ASK-16WOFDM. This is because by using BPSK before 16FOFDM and 16WOFDM, the Euclidean distance among the signal vectors in the signal space increases due to which the signal energy associated with that distance also increases. Due to the same reason, 16QAM performs better than 16DPSK.

In comparison of Figures 4.5 and 4.6, it can be observed that BER performance of both system models with all seven modulation techniques are similar. This is due to the fact that the distance between DANs and DGN is very small (1 m) as compared to transmission distance (20 m).

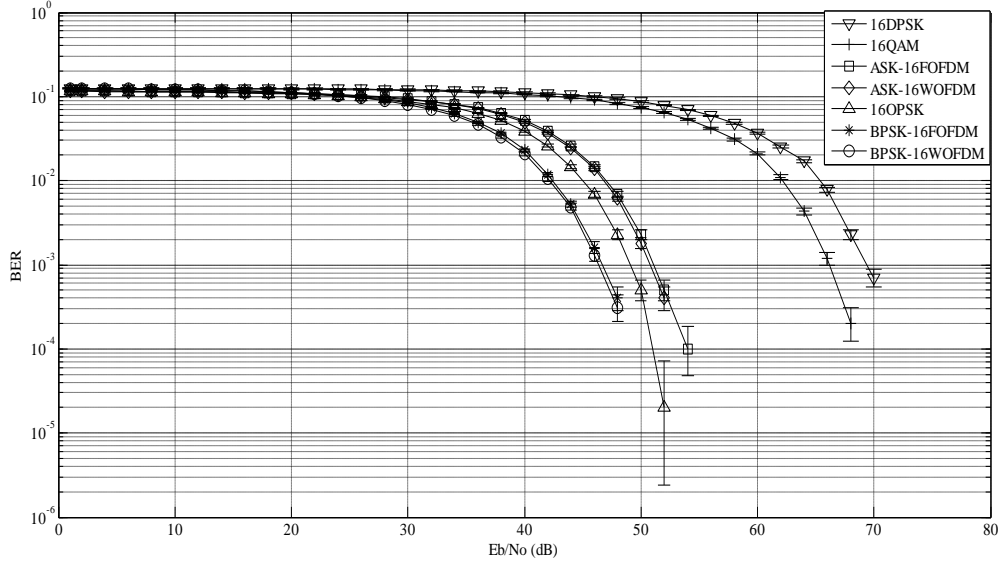


Figure 4.5: BER performance over transmission distance of 20 m with True MIMO DGN Architecture

The RF (Analogue) energy consumption per bit per antenna over a transmission distance of 1–100 m is shown in Figure 4.7 and 4.8 for both system models, using 16-DPSK, 16-QAM, ASK-16FOFDM, ASK-16WOFDM, 16-OPSK, BPSK-16FOFDM, and BPSK-16WOFDM with a PAPR of 0, 2.55, 3.01, 3.01, 0, 0 and 0 dB, respectively. The 16-DPSK, 16-OPSK, BPSK-16FOFDM, and BPSK-16WOFDM have 0 dB PAPR because the modulated symbols have constant power envelop.

In all the simulations, it is assumed $G_t = G_r = 8$ dBi, $f_c = 2.5$ GHz, $\bar{P}_b = \bar{P}_b^l = \bar{P}_b^l = 10^{-3}$, $M_l = 40$ dB, $N_f = 10$ dB, $\zeta = 0.35$, $\sigma^2 = -174$ dBm/Hz, $G_{ti} = G_{ri} = 2$ dBi, $d^l = 1$ m, $P_{DAC} = 15.5$ mW, $P_{ADC} = 9.8$ mW, $P_{fil} = 1.25$ mW, $P_{LO} = 50$ mW, $P_{LNA} = 20$ mW, $P_{IFA} = 3$ mW, $P_{mix} = 30.3$ mW, $P_{Add} = 10$ mW, and $P_{PS} = 5$ mW.

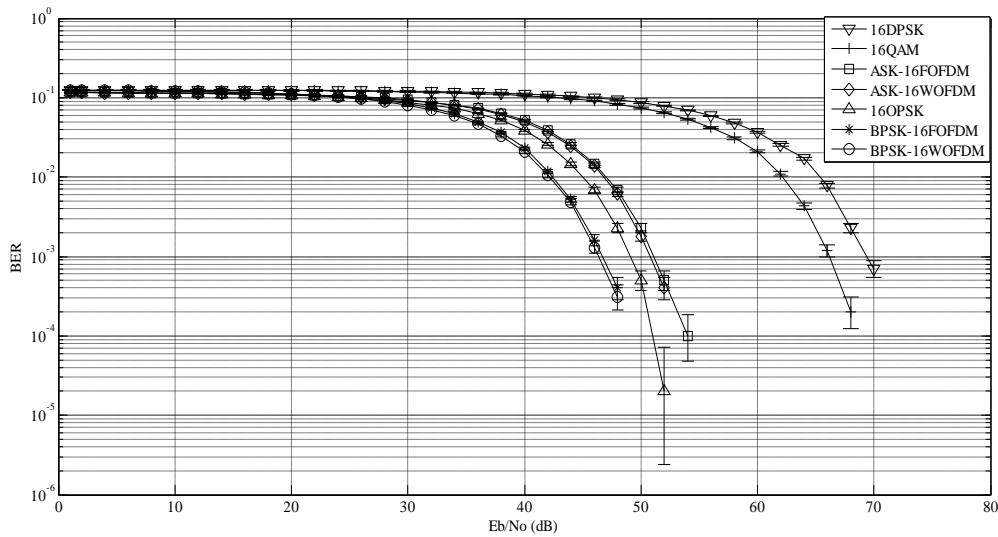


Figure 4.6: BER performance over transmission distance of 20 m with Virtual MIMO DGN Architecture

The RF (Analogue) energy per bit per node is calculated for every 5 m of distance to evaluate the effect of distance on energy consumption. It is observed that 16-QAM and 16-DPSK based systems are the least energy-efficient due to their poor BER performance and complex RF architecture, with the former being the more dominant factor. However, both techniques performed almost the same even though the BER performance of 16-DPSK is poorer as compared to 16-QAM. This is due to the lower PAPR of 16-DQPSK which resulted in the RF (Analogue) energy consumption performance of both techniques to be almost alike. 16-OPSK system with complex RF architecture performs better than ASK-16FOFDM and ASK-16WOFDM system due to its better BER performance and lower PAPR. ASK-16WOFDM based system consumes less energy as compared to ASK-16FOFDM by approximately 40% due to its simpler RF architecture. Almost half of the energy saving can be attributed to fewer mixers used in the RF architecture of ASK-16WOFDM, which reduces the amount of circuit energy it consumes.

For the same reason, BPSK-16WOFDM is also found to consume less energy than BPSK-16FOFDM by a similar margin. It is also observed that BPSK-16FOFDM, and BPSK-16WOFDM, are more energy efficient than ASK-16FOFDM and ASK-16WOFDM, respectively, mainly due to their lower PAPR. For transmission distance of less than 5 m, the system model with 4 DSNs, 3 DANs and 1 DGN each with single antenna is slightly less energy efficient as compared to system model with 4 DSN each with single and 1 DGN with 4 antennas because the latter system does not involve any local communication. For all other transmission distances, the RF (Analogue) energy consumption per bit per antenna of both systems is approximately the same. In calculating the RF (Analogue) energy consumption for all the modulation schemes, except the power consumption of power amplifier as discussed in sections 4.1.2.1 and 4.2.2.1, the PAPR value and power consumption of all circuit blocks for true MIMO DGN and virtual MIMO DGN system architectures remain the same for all transmission distances.

Note that for Virtual MIMO DGN, energy consumption is expressed in per bit per node, unlike in True MIMO DGN which is expressed in per bit per antenna. This is because in the latter, the receiver side consists of 1 DGN with 4 antennas, while the former consists of 1 DGN and 3 DANs, each with a single antenna.

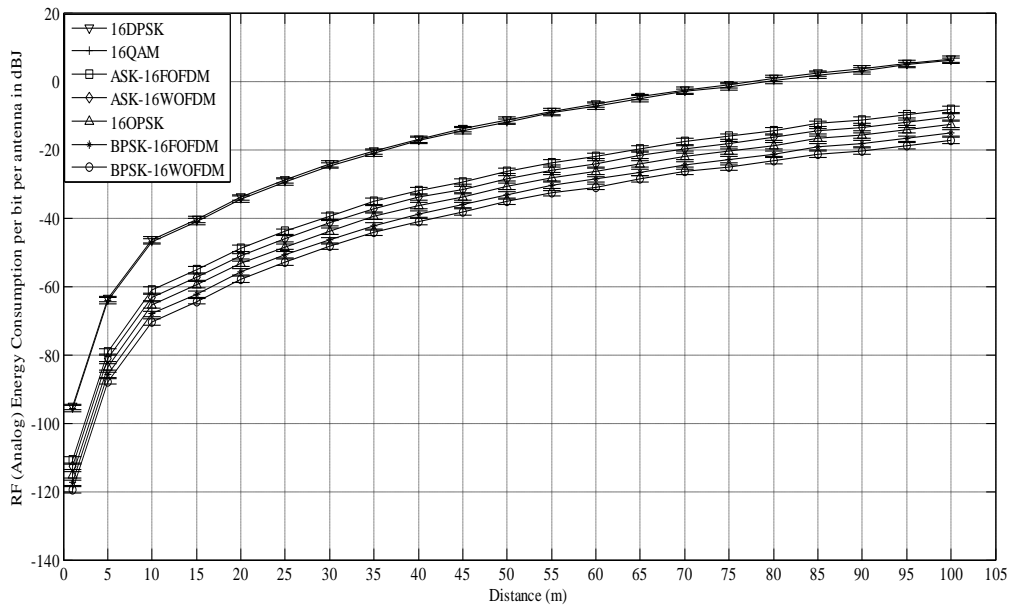


Figure 4.7: Total energy per bit per antenna over transmission distance of 1 to 100 m with True MIMO DGN Architecture

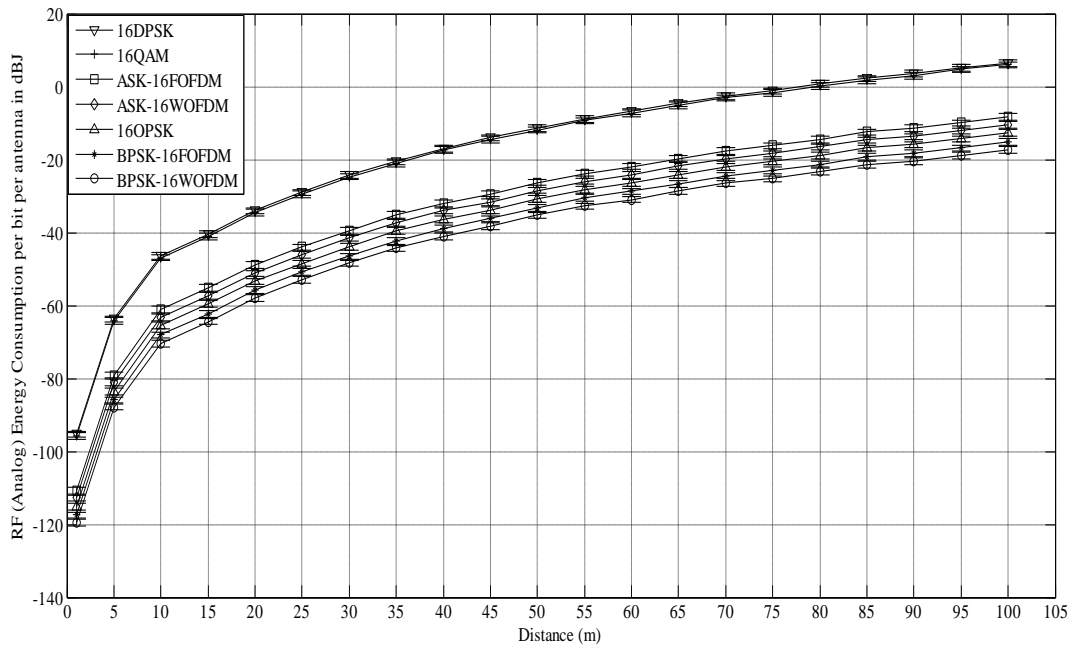


Figure 4.8: Total energy per bit per antenna over transmission distance of 1 to 100 m with Virtual MIMO DGN Architecture

The base band energy consumption per bit per antenna ($E_{b_Digital}$) for all modulation types along with their constituting energy consumed by individual modulator, demodulator, and detection algorithm for system with True MIMO DGN are shown in Table 4.1. It is observed that each modulator consumes more energy due to slow processing speed of MSP430F1611 (CPU model of TelosB mote) as compared to demodulator. The demodulator energy consumption is calculated based on Xilinx XC2V6000-6 FPGA which has high processing speed. Another reason for more energy consumption of modulator is its higher computational complexity (in terms of CPU cycles per bit). For similar reasons, 16-DPSK consumes less $E_{b_Digital}$ as compared to other modulation techniques.

<i>Modulation Type</i>	<i>E_{Mod} per bit in dBJ</i>	<i>E_{Dmod} per bit in dBJ</i>	<i>E_{Det} per bit in dBJ</i>	<i>$E_{b_Digital}$ per bit per antenna in dBJ</i>
16-DPSK	-31.7203	-33.4768	-32.0412	-31.9441
16-QAM	-31.2628	-33.3065	-32.0412	-31.6400
16-OPSK	-30.8951	-32.4582	-32.0412	-31.1414
ASK-16FOFDM	-30.0134	-32.0571	-32.0412	-30.5162
ASK-16WOFDM	-31.0294	-33.0582	-32.0412	-31.4275
BPSK-16FOFDM	-29.860	-31.9249	-32.0412	-30.3835
BPSK-16WOFDM	-30.8764	-32.6060	-32.0412	-31.1853

Table 4.1: Base Band (Digital) Energy Consumption with True MIMO DGN Architecture

Table 4.2 shows the base band energy consumption per bit per node ($E_{b_Digital}$) of all modulation techniques for the system with virtual MIMO DGN. It is observed that modulator consumes more energy as compared to demodulator due to more computational complexity.

<i>Modulation Type</i>	E_{Mod} <i>per bit in dBJ</i>	E_{Dmod} <i>per bit in dBJ</i>	E_{Det} <i>per bit in dBJ</i>	$E_{b_Digital}$ <i>per bit per node in dBJ</i>
16-DPSK	-31.7203	-32.1389	-30.7033	-31.2591
16-QAM	-31.2628	-31.9686	-30.7033	-30.9803
16-OPSK	-30.8951	-31.1203	-30.7033	-30.4600
ASK-16FOFDM	-30.0134	-30.7192	-30.7033	-29.8781
ASK-16WOFDM	-31.0294	-31.7203	-30.7033	-30.8009
BPSK-16FOFDM	-29.86	-30.587	-30.7033	-29.8167
BPSK-16WOFDM	-30.8764	-31.2681	-30.7033	-30.5142

Table 4.2: Base Band (Digital) Energy Consumption with Virtual MIMO DGN Architecture

Comparing Table 4.1 and Table 4.2, it is clear that modulator energy consumption for both system models is the same. The E_{Dmod} and E_{Det} value for the system with True MIMO DGN is less as compared to system model with Virtual MIMO DGN architecture. This is due to faster processing speed of the hardware (Xilinx XC2V6000-6 FPGA) that is used to calculate E_{Dmod} and E_{Det} of the True MIMO DGN system. On the other hand, the slower processing speed of MSP430F1611 (CPU model of TelosB mote) is contributing to the higher E_{Dmod} and E_{Det} value for the Virtual MIMO DGN system.

Table 4.3 and 4.4 show the RF (Analogue) energy consumption (E_{b_Analog}) at different transmission distances values and total energy consumption ($E_{b_Total} = E_{b_Analog} + E_{b_Digital}$) for true MIMO, and virtual MIMO DGN architecture, respectively. It is clear from Sections 4.1.22 and 4.2.2.2 that $E_{b_Digital}$ is independent of transmission distance. For short distance (d and $d^L \leq 25$ m), $E_{b_Digital}$ has significant effect on E_{b_Total} . However, as d and d^L increases, E_{b_Analog} increases, which reduces the effect of $E_{b_Digital}$. ASK-16WOFDM performs better for short distance

(d and $d^L \leq 25m$) as compared to BPSK-16FOFDM, ASK-16FOFDM, 16-OPSK and BPSK-16WOFDM as a result of a lower $E_{b_Digital}$. For larger distances, BPSK-16WOFDM performs better because of a lower E_{b_Analog} .

The time delays involved during the communication for true MIMO DGN system model are listed in Table 4.5. It is observed that T_{tr_t} is 1 μ s/bit for all modulation techniques. T_{pr_t} is calculated using Equation (4.12) for $d = 10 m$ and $d = 100 m$. It is also observed that the modulator incurred a higher processing time (T_{Mod}) than the demodulator (T_{Dmod_t}) because the processing speed of MSP430F1611 (CPU model of TelosB mote) is slower as compared to that of Xilinx XC2V6000-6 (FPGA). For this reason, the total processing delay T_{pc_t} is considerably high as compared to T_{tr_t} and T_{pr_t} . Thus, T_{pc_t} is the most dominant time delay factor for the total time delay of T_{T-MIMO} . 16-DPSK based system is found to incur the least total time delay due to its lower T_{pc_t} as compared to other six modulation techniques, followed by 16-QAM, ASK-16WOFDM, BPSK-16WOFDM, 16-OPSK, ASK-16FOFDM, and BPSK-16FOFDM.

The time delays for Virtual MIMO DGN architecture are shown in Table 4.6. It is observed that T_{tr} is 1.75 μ s/bit for all modulation techniques. T_{pr} is calculated using Equation 4.24 for $d^L = 10 m$ and $d^L = 100 m$. It is also observed that the modulator incurred a higher processing time (T_{Mod}) than the demodulator (T_{Dmod}). This is because more mathematical operations are involved in modulating the signal than demodulating. The total processing delay T_{pc} is significantly high as compared to T_{tr_MIMO} and T_{pr_MIMO} due to lower processing speed of

TelosB mote. Therefore, T_{pc} is the most dominant time delay factor for the total time delay of Virtual MIMO DGN system model (T_{V-MIMO}).

<i>Modulation Type</i>	E_{b_Analog} <i>per bit per antenna in dBJ</i>				$E_{b_Total} = E_{b_Analog} + E_{b_Digital}$ <i>per bit per antenna in dBJ</i>			
	$d = 25m$	$d = 50m$	$d = 75m$	$d = 100m$	$d = 25m$	$d = 50m$	$d = 75m$	$d = 100m$
16-DPSK	-29.0354	-11.4148	-1.1630	6.4758	-27.2403	-11.3765	-1.1593	6.4757
16-QAM	-29.5144	-11.8938	-1.6419	5.9967	-27.4381	-11.8479	-1.6375	5.9974
16-OPSK	-48.4654	-30.6948	-20.6230	-12.6442	-31.0617	-27.9020	-20.2537	-12.5832
ASK-16FOFDM	-44.0580	-26.2874	-16.2156	-8.2368	-30.3281	-24.8959	-16.0571	-8.2110
ASK-16WOFDM	-46.0988	-28.4682	-18.4363	-10.4776	-31.2818	-26.6902	-18.2234	-10.4428
BPSK-16FOFDM	-50.7654	-33.2648	-22.9930	-15.1242	-30.3439	-28.5791	-22.2654	-14.9967
BPSK-16WOFDM	-52.9461	-35.2855	-25.2637	-17.2949	-31.1564	-29.7581	-24.2746	-17.1211

Table 4.3: RF (Analogue) Energy Consumption and Total Energy Consumption with True MIMO DGN Architecture

<i>Modulation Type</i>	E_{b_Analog} <i>per bit per node in dBJ</i>				$E_{b_Total} = E_{b_Analog} + E_{b_Digital}$ <i>per bit per node in dBJ</i>			
	$d^L = 25m$	$d^L = 50m$	$d^L = 75m$	$d^L = 100m$	$d^L = 25m$	$d^L = 50m$	$d^L = 75m$	$d^L = 100m$
16-DPSK	-29.0354	-11.4148	-1.1630	6.4758	-26.9961	-11.3700	-1.1587	6.4765
16-QAM	-29.5144	-11.8938	-1.6419	5.9967	-27.1754	-11.8405	-1.6369	5.99766
16-OPSK	-48.4654	-30.6948	-20.6230	-12.6442	-30.3918	-27.5655	-20.1940	-12.5729
ASK-16FOFDM	-44.0580	-26.2874	-16.2156	-8.2368	-29.7153	-24.7115	-16.0327	-8.20722
ASK-16WOFDM	-46.0988	-28.4682	-18.4363	-10.4776	-30.6746	-26.4695	-18.1914	-10.4374
BPSK-16FOFDM	-50.7654	-33.2648	-22.9930	-15.1242	-29.7819	-28.1969	-22.1730	-14.9792
BPSK-16WOFDM	-52.9461	-35.2855	-25.2637	-17.2949	-30.4894	-29.2648	-24.1293	-17.09279

Table 4.4: RF (Analogue) Energy Consumption and Total Energy Consumption with Virtual MIMO DGN Architecture

T_{tr_t} value is less as compared to T_{tr} because no local communication is involved in true MIMO DGN system model. T_{pc_t} value is also less as compared to T_{pc} due to high processing speed of Xilinx XC2V6000-6 (FPGA). In both system models, processing time (T_{pc_t}, T_{pc}) is the most dominant factor.

Modulation Type	T_{tr_t} secs/bit	T_{pr_t} secs/bit		T_{pc_t} secs/bit				T_{T-MIMO} secs/bit	
		$d = 10m$	$d = 100m$	T_{Mod}	T_{Dmod_t}	T_{Det_t}	T_{pc_t}	$d = 10m$	$d = 100m$
		16-DPSK	1×10^{-6}	3.33×10^{-8}	3.33×10^{-7}	0.069230	1.1957×10^{-3}	1.66×10^{-3}	0.0720
16-QAM	1×10^{-6}	3.33×10^{-8}	3.33×10^{-7}	0.076925	1.2454×10^{-3}	1.66×10^{-3}	0.0798	0.0798	0.0798
16-OPSK	1×10^{-6}	3.33×10^{-8}	3.33×10^{-7}	0.083717	1.5140×10^{-3}	1.66×10^{-3}	0.0868	0.0868	0.0868
ASK-16FOFDM	1×10^{-6}	3.33×10^{-8}	3.33×10^{-7}	0.102575	1.6605×10^{-3}	1.66×10^{-3}	0.1059	0.1059	0.1059
ASK-16WOFDM	1×10^{-6}	3.33×10^{-8}	3.33×10^{-7}	0.0800	1.3186×10^{-3}	1.66×10^{-3}	0.0829	0.0829	0.0829
BPSK-16FOFDM	1×10^{-6}	3.33×10^{-8}	3.33×10^{-7}	0.10625	1.711×10^{-3}	1.66×10^{-3}	0.1096	0.1096	0.1096
BPSK-16WOFDM	1×10^{-6}	3.33×10^{-8}	3.33×10^{-7}	0.084075	1.4634×10^{-3}	1.66×10^{-3}	0.0872	0.0872	0.0872

Table 4.5: Total Time Delay for True MIMO DGN Architecture

Modulation Type	T_{tr} secs/bit	T_{pr} secs/bit		T_{pc} secs/bit				T_{V-MIMO} secs/bit	
		$d^L = 10m$	$d^L = 100m$	T_{Mod}	T_{Dmod}	T_{Det}	T_{pc}	$d^L = 10m$	$d^L = 100m$
		16-DPSK	1.75×10^{-6}	3.33×10^{-8}	3.33×10^{-7}	0.069230	0.06286	0.0875	0.21959
16-QAM	1.75×10^{-6}	3.33×10^{-8}	3.33×10^{-7}	0.076925	0.06537	0.0875	0.2298	0.2298	0.2298
16-OPSK	1.75×10^{-6}	3.33×10^{-8}	3.33×10^{-7}	0.083717	0.07948	0.0875	0.25070	0.25070	0.25070
ASK-16FOFDM	1.75×10^{-6}	3.33×10^{-8}	3.33×10^{-7}	0.102575	0.08717	0.0875	0.27725	0.27725	0.27725
ASK-16WOFDM	1.75×10^{-6}	3.33×10^{-8}	3.33×10^{-7}	0.0800	0.06922	0.0875	0.236725	0.236727	0.236727
BPSK-16FOFDM	1.75×10^{-6}	3.33×10^{-8}	3.33×10^{-7}	0.10625	0.08987	0.0875	0.28360	0.28360	0.28360
BPSK-16WOFDM	1.75×10^{-6}	3.33×10^{-8}	3.33×10^{-7}	0.084075	0.07682	0.0875	0.24840	0.24840	0.24840

Table 4.6: Total Time Delay for Virtual MIMO DGN Architecture

From a comparison of the results between Table 4.1 and Table 4.6, it can be observed that modulation techniques with less T_{pc} will also exhibit less $E_{b_Digital}$ value, and vice versa. For example, the T_{pc} and $E_{b_Digital}$ of 16-DPSK is 0.2195 seconds, and -31.2591 dBJ (or 0.7483×10^{-3} J), respectively, while it is 0.2836 seconds, and -29.8167 dBJ (or 1.0431×10^{-3} J), respectively, for BPSK-16FOFDM.

The spectral efficiency can be calculated using Equation (4.9) for various $\frac{E_b}{N_o}$ values. The four data points on each curve are obtained by setting the BER values to 10^{-1} , 10^{-2} , 10^{-3} , and 10^{-4} . It can be observed from Equation (4.9) that by increasing $\frac{E_b}{N_o}$, spectral efficiency will increase. For a given BER = 10^{-3} (third data point), BPSK-16WOFDM and BPSK-16FOFDM have a spectral efficiency of 27 bit/sec/Hz at $\frac{E_b}{N_o} = 46$ dB, ASK-16WOFDM and ASK-16FOFDM have a spectral efficiency of 30.7 bit/sec/Hz at $\frac{E_b}{N_o} = 51$ dB, and 16-QAM has a spectral efficiency of 45.5 bit/sec/Hz at $\frac{E_b}{N_o} = 66$ dB. The energy efficiency (EE) versus spectral efficiency (SE) graph for different modulation techniques is shown in Figure 4.9 and 4.10. The EE and SE values are obtained for transmission distance of 20 m. At this distance, the EE value for both system models is the same. The four data points on each curve are obtained by setting the BER values to 10^{-1} , 10^{-2} , 10^{-3} and 10^{-4} . From the graphs, it can be observed that there is a trade-off between EE and SE, where an increase in SE due to higher $\frac{E_b}{N_o}$ decreases the EE. For a given SE value, it is observed that BPSK-16WOFDM is the most energy efficient technique.

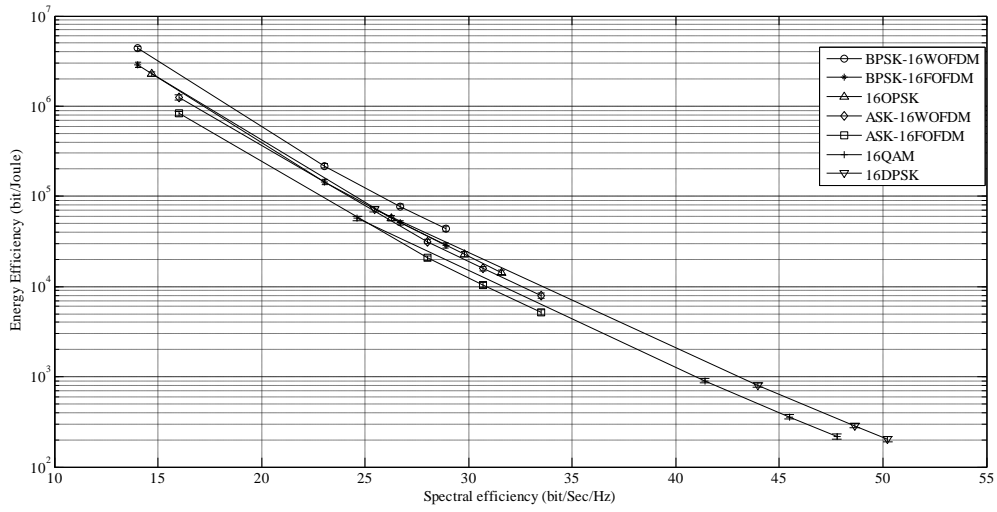


Figure 4.9: Energy Efficiency versus Spectral Efficiency for True MIMO DGN Architecture

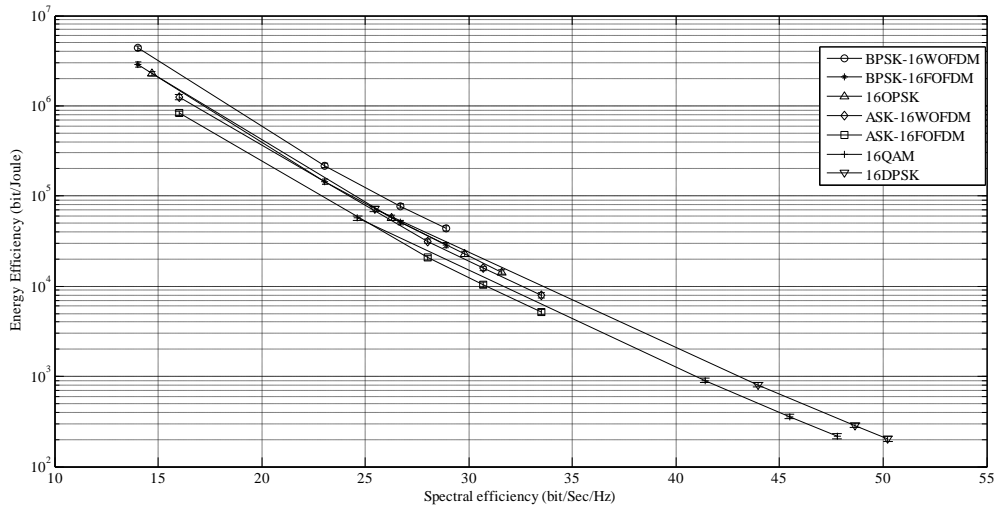


Figure 4.10: Energy Efficiency versus Spectral Efficiency for Virtual MIMO DGN Architecture

Chapter 5

MIMO Channel Equalisation

In communication systems, equalisation is performed to eliminate magnitude or frequency dependant phase distortion introduced by the channel [84]. Equalisation techniques are also used to minimise the effect of inter symbol interference (ISI) due to multipath propagation. When the transmitted signal passes through a channel, it may suffer from magnitude and/or phase distortion. To compensate the effect of channel on transmitted signal, channel equalisation is performed at the receiver side. Usually different types of filters are used to compensate the channel effects. To equalise a SISO channel, Zero-Forcing, MMSE or Decision Feedback equalising techniques [85] can be used.

MIMO wireless communication techniques have attracted much attention in recent years due to their high data rates capability. However, channel equalisation will be more challenging for MIMO channels than for SISO channels, as MIMO systems have to deal with not only ISI, but also the problem of spatial and co-channel interference [86]. Different detection algorithms are used to detect the transmitted signal at receiver side. It has been shown in [87] that performing detection is equivalent to undertaking channel equalisation. The purpose of equalisation is to eliminate the channel effects and retrieve the transmitted signals correctly, which are also the aims of detection algorithms. Different detection techniques have been discussed in detail for various MIMO systems in Section 3.1.

In this chapter, we propose a new MIMO channel equalisation technique which uses QMF bank architecture. As discussed in Section 3.3.1, the QMF bank architecture can also be used for WOFDM modulation/demodulation.

A wireless channel can be represented by a linear filter with frequency response $H(f) = |H(f)|e^{j\theta(f)}$ where $|H(f)|$ is the magnitude response, and $\theta(f)$ is the phase response of the channel. For distortion less transmission, $|H(f)|$ must be constant and $\theta(f)$ must be a linear function of frequency for a given transmission bandwidth [85]. The equalising filter frequency response can be related to channel frequency response as follows:

$$H_e(f) = \frac{1}{|H(f)|e^{j\theta(f)}} = \frac{1}{|H(f)|}e^{-j\theta(f)} \quad (5.1)$$

5.1 MIMO Channel Equalisation with QMF Bank Architecture

MIMO channel frequency response is shown in Section 3.1.1.1. MIMO channel (H) can be equalised by using optimised QMF synthesis side filter banks as shown in Figure 5.1. To the best of our knowledge, this is the first time that QMF bank architecture is used to equalise a MIMO channel. First of all, a modified channel matrix G can be defined as follows:

$$G = H + \frac{1}{SNR} I_{N_r} \quad (5.2)$$

where $\frac{1}{SNR}$ is the noise power to signal power ratio, and I_{N_r} is the identity matrix of size N_r . G can be decomposed into unitary matrices using Singular Value decomposition (SVD). For this technique, channel state information (CSI) is required at receiver side.

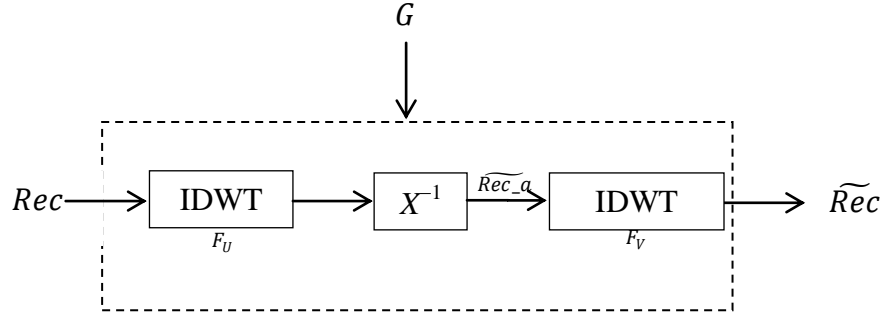


Figure 5.1: MIMO Channel Equalisation Block

Consider a MIMO system with N_t transmitting and N_r receiving antennas, the received signal vector (Rec) is represented as:

$$Rec = HS + \eta \quad (5.3)$$

where S is an $N_t \times I$ vector, η is an $N_r \times I$ noise vector whose elements are complex Gaussian random variables with zero mean and variance N_o , and H is an $N_r \times N_t$ channel matrix. By using SVD, modified MIMO channel matrix G can be decomposed as follows:

$$(U, X, V) = SVD(G) \quad (5.4)$$

where U and V are unitary matrices ($UU^T = VV^T = I$) with $N_r \times N_r$, and $N_t \times N_t$ matrix order, respectively, and X is $N_r \times N_t$ diagonal matrix.

The received signal vector Rec first passes through the filter bank (F_U). It is then multiplied by X^{-1} and will pass through the filter bank (F_V) as shown in Figure 5.1. X^{-1} can be calculated just by taking the reciprocals of diagonal elements of matrix X .

The structure of filter banks F_U and F_V are shown in Figure 5.2, and 5.3, respectively. The filter coefficients of F_U are set according to matrix U as shown in Equation (5.5), while that of F_V are set according to matrix V^T as shown in Equation (5.6).

$$\begin{aligned}
 f_{U0} &= (U_{11} \ U_{12} \ \dots \ U_{1N_r}) \\
 f_{U1} &= (U_{21} \ U_{22} \ \dots \ U_{2N_r}) \\
 &\vdots \\
 f_{UN_r-1} &= (U_{N_r1} \ U_{N_r2} \ \dots \ U_{N_rN_r})
 \end{aligned} \tag{5.5}$$

$$\begin{aligned}
 f_{V0} &= (V_{11} \ V_{21} \ \dots \ V_{N_t1}) \\
 f_{V1} &= (V_{12} \ V_{22} \ \dots \ V_{N_t2}) \\
 &\vdots \\
 f_{VN_t-1} &= (V_{1N_t} \ V_{2N_t} \ \dots \ V_{N_tN_t})
 \end{aligned} \tag{5.6}$$

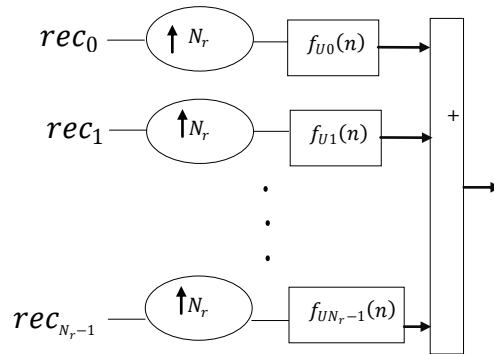


Figure 5.2. Filter Bank Structure (F_U)

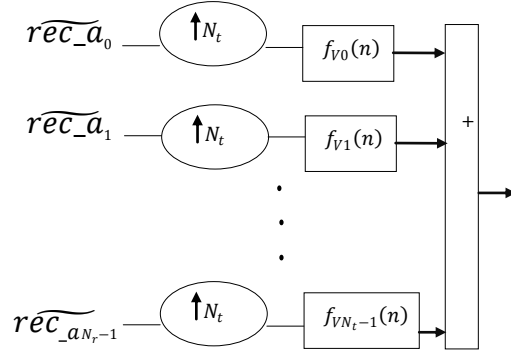


Fig. 5.3. Filter Bank Structure (F_V)

In Figure 5.2 and Figure 5.3, the input of each branch is first upsampled and then sent through a filter as discussed in Section C.1 of Chapter 2. The signal after MIMO channel equalisation block then becomes:

$$\widetilde{Rec} = F_V X^{-1} F_U Rec \quad (5.7)$$

$$\widetilde{Rec} = F_V X^{-1} F_U (HS + \eta) \quad (5.8)$$

Replacing H in Equation 5.8 by G :

$$\widetilde{Rec} = F_V X^{-1} F_U (GS + \eta) \quad (5.9)$$

Further replacing G by UXV^T , and F_V and F_U by V , and U^T , respectively, Equation(5.9) then becomes:

$$\widetilde{Rec} = VX^{-1}U^T(UXV^T S + \eta) \quad (5.10)$$

Let

$$\widetilde{Rec}_{-a} = V(V^T S + X^{-1}U^T \eta) \quad (5.12)$$

Then \widetilde{Rec} becomes:

$$\widetilde{Rec} = S + \zeta \quad (5.13)$$

where $\zeta = VX^{-1}U^T\eta$ is statistically identical to η .

The i_{th} transmitted signal value can be estimated by slicing it to the nearest value in the signal constellation. The SVD-ZF technique has been discussed with details in Section 3.1.2.4. In our proposed QMF bank detection process, filter bank structure is used after decomposition of modified channel matrix G .

5.2. Evaluation Results

Simulations are carried out to investigate the performances of system models mentioned in Section 4.1.1 and 4.1.2. Instead of using QR detection algorithm as outlined in sub-section A.3 of Section 3.1.1.2 in Chapter 3, the above mentioned MIMO channel equalisation technique is used to explore the performance of BPSK-16WOFDM. All simulation parameters are the same as mentioned in Section 4.3.

The BER performance with True MIMO DGN system model is shown in Figure 5.4 while that with Virtual MIMO DGN system model is shown in Figure 5.5. It can be observed from Figures 5.4 and 5.5 that BER performances of both system models are similar. This is due to the fact that the distance between DANs and DGN is very small (1 m) as compared to transmission distance (20 m). However, between using QR and QMF bank detection process, for $BER=10^{-3}$, the $\frac{E_b}{N_o}$ value is 43 dB for BPSK-16WOFDM with QMF bank detection process while that with QR detection process is 46 dB. This 3 dB improvement is due to the modification of channel matrix (H) by incorporating the term $\frac{1}{SNR}I_{N_r}$ with QMF bank architecture, which suppresses the noise effect. Instead of taking the inverse of G , filtering operation is done to detect the transmitted signals.

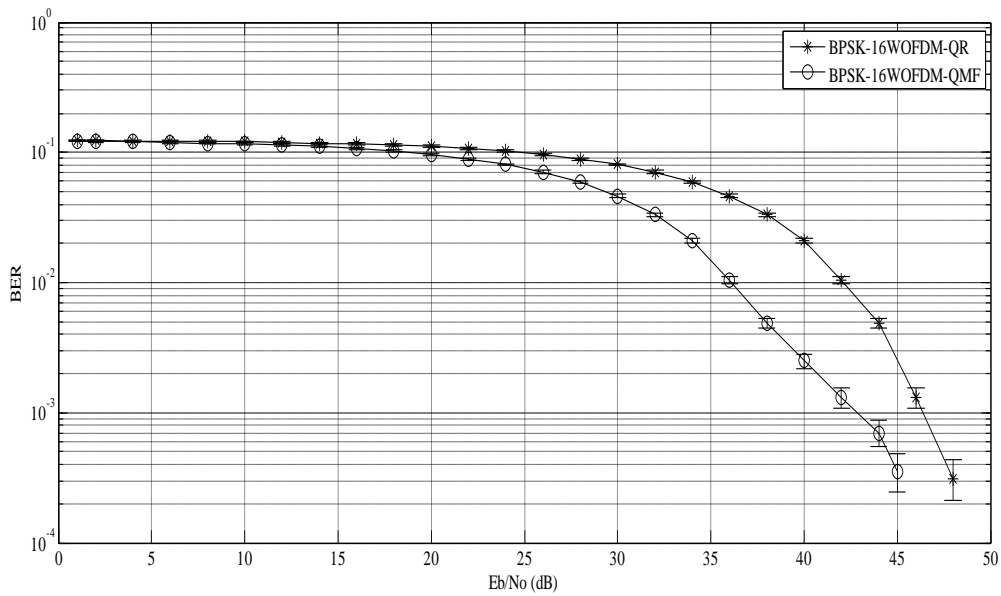


Figure 5.4: BER performance over transmission distance of 20 m with True MIMO DGN using QR and QMF Bank detection process

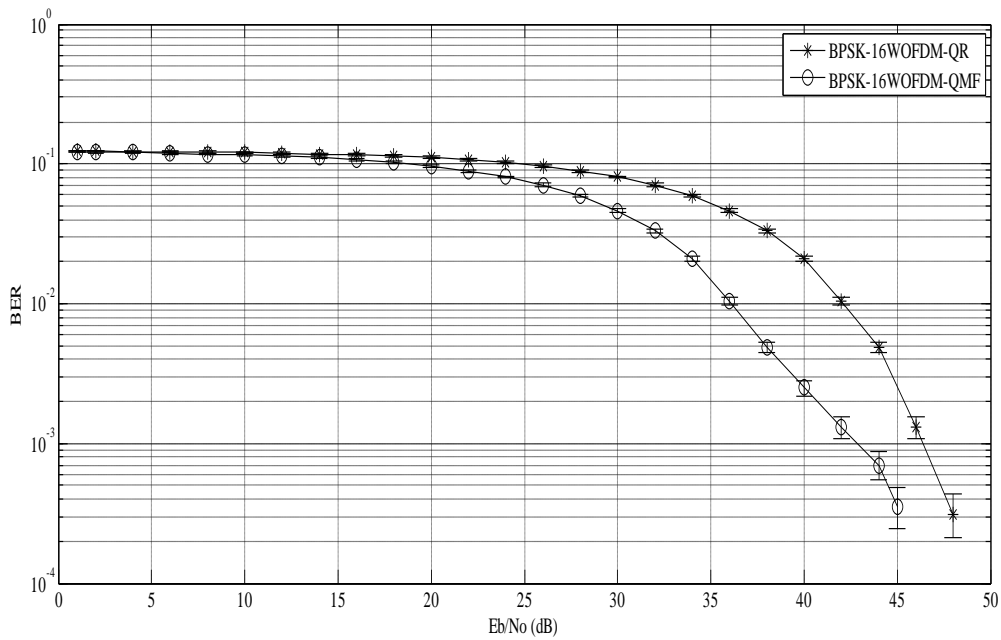


Figure 5.5: BER performance over transmission distance of 20 m with Virtual MIMO DGN using QR and QMF Bank detection process

Figures 5.6 and 5.7 show the RF (Analogue) energy consumption for both system models over a transmission distance of 1–100m. As in Figures 5.4 and 5.5, the energy performances of both system models are similar. However, the systems with BPSK-16WOFDM and QMF bank architecture are more energy efficient as compared to BPSK-16WOFDM with QR detection algorithm due to better BER performances. As observed from Equations (4.3) and (4.6), the transmit power is directly proportional to energy per bit for a given BER. Thus, the better the BER performance, the more energy efficient it will be for the system. For example, at transmission distance of 20m, the energy consumption by BPSK-16WOFDM with QMF bank architecture is -60.94 dBJ (8.046×10^{-7} joules), while for BPSK-16WOFDM with QR detection algorithm, it is -57.94 dBJ (16.05×10^{-7} joules).

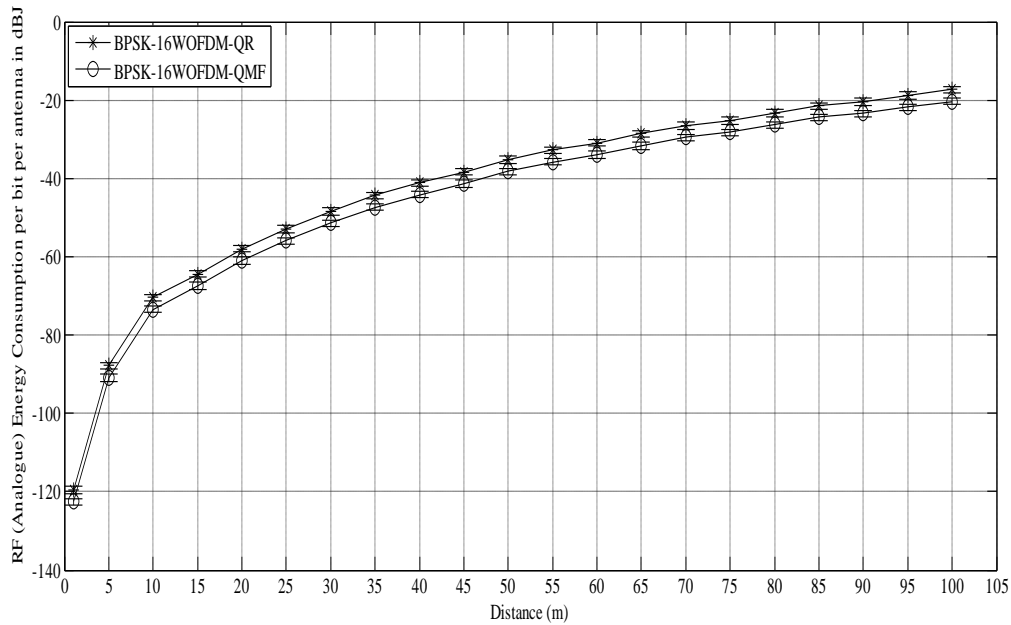


Figure 5.6: Total energy per bit per antenna over transmission distance of 1 to 100 m with True MIMO DGN using QR and QMF Bank detection process

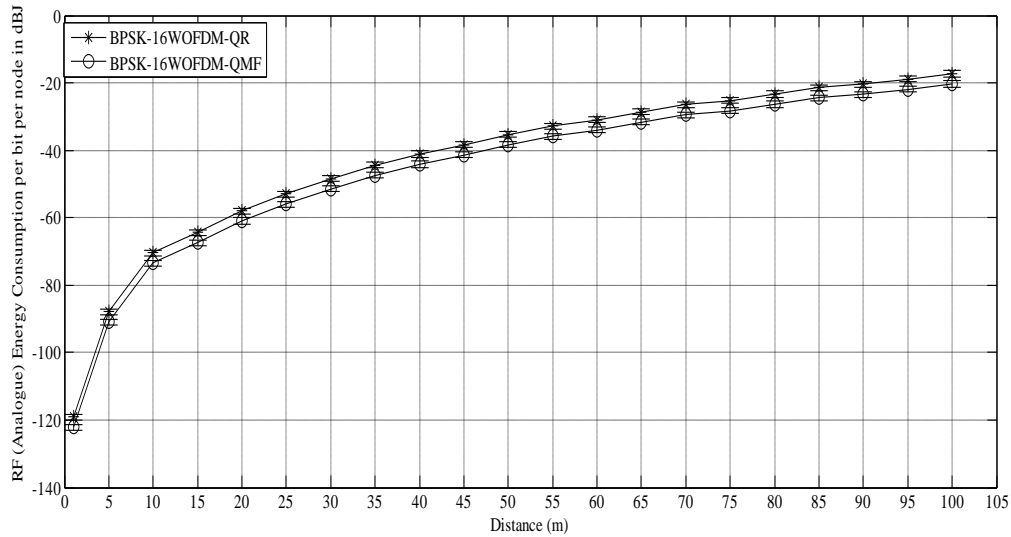


Figure 5.7: Total energy per bit per antenna over transmission distance of 1 to 100 m with Virtual MIMO DGN using QR and QMF Bank detection process

The base band energy consumption per bit per antenna ($E_{b_Digital}$) for BPSK-16WOFDM with QR detection algorithm and QMF bank architecture energy consumption values with True MIMO DGN are shown in Table 5.1, while that with Virtual MIMO DGN in Table 5.2. It is observed from both tables that energy consumption with QMF bank detection process is less as compared to QR detection process. This is due to the lower computation complexity of QMF bank detection process, which reduces the corresponding E_{Det} (energy consumption by detection algorithm) for both system models. Comparing the E_{Det} value of both system models, it can be observed that True MIMO DGN architecture consumes less energy as compared to Virtual MIMO DGN architecture. This is due to faster processing speed of the hardware (Xilinx XC2V6000-6 FPGA) that is used to calculate E_{Det} of the True MIMO DGN system. On the other hand, the slower processing speed of MSP430F1611 (CPU model of TelosB mote) is contributing to the higher E_{Det} value for the Virtual MIMO DGN system.

<i>Modulation Type</i>	E_{Mod} <i>per bit in dBJ</i>	E_{Dmod} <i>per bit in dBJ</i>	E_{Det} <i>per bit in dBJ</i>	$E_{b_Digital}$ <i>per bit per antenna in dBJ</i>
BPSK-16WOFDM-QR	-30.8764	-32.6060	-32.0412	-31.1853
BPSK-16WOFDM-QMF	-30.8764	-32.6060	-32.2168	-31.2030

Table 5.1: Base Band (Digital) Energy Consumption with True MIMO DGN Architecture

<i>Modulation Type</i>	E_{Mod} <i>per bit in dBJ</i>	E_{Dmod} <i>per bit in dBJ</i>	E_{Det} <i>per bit in dBJ</i>	$E_{b_Digital}$ <i>per bit per node in dBJ</i>
BPSK-16WOFDM-QR	-30.8764	-31.2681	-30.7033	-30.5142
BPSK-16WOFDM-QMF	-30.8764	-31.2681	-30.8788	-30.5349

Table 5.2: Base Band (Digital) Energy Consumption with Virtual MIMO DGN Architecture

Table 5.3 and 5.4 show the RF (Analogue) energy consumption (E_{b_Analog}) at different transmission distances values and total energy consumption ($E_{b_Total} = E_{b_Analog} + E_{b_Digital}$) for true MIMO, and virtual MIMO DGN architecture, respectively. It can be observed that for different values of transmission distances (d and d^L), E_{b_Total} value of QMF detection process is less than QR detection process for all transmission distances. This is due to the lower E_{b_Analog} and $E_{b_Digital}$ values of QMF. As mentioned in Chapter 4, $E_{b_Digital}$ is independent of transmission distance. For short distance (d and $d^L \leq 25$ m), $E_{b_Digital}$ has significant effect on E_{b_Total} . However, as d and d^L increases, E_{b_Analog} increases, which reduces the effect of $E_{b_Digital}$.

<i>Modulation Type</i>	<i>E_{b_Analog}</i> <i>per bit per antenna in dBJ</i>				<i>$E_{b_Total} = E_{b_Analog} + E_{b_Digital}$</i> <i>per bit per antenna in dBJ</i>			
	<i>d = 25m</i>	<i>d = 50m</i>	<i>d = 75m</i>	<i>d = 100m</i>	<i>d = 25m</i>	<i>d = 50m</i>	<i>d = 75m</i>	<i>d = 100m</i>
BPSK-16WOFDM- QR	-52.9461	-35.2855	-25.2637	-17.2949	-31.1564	-29.7581	-24.2746	-17.1211
BPSK-16WOFDM- QMF	-55.9462	-38.2856	-28.2637	-20.2950	-31.1884	-30.4265	-26.4789	-19.9562

Table 5.3: RF (Analog) Energy Consumption and Total Energy Consumption for True MIMO DGN Architecture

<i>Modulation Type</i>	<i>E_{b_Analog}</i> <i>per bit per antenna in dBJ</i>				<i>$E_{b_Total} = E_{b_Analog} + E_{b_Digital}$</i> <i>per bit per node in dBJ</i>			
	<i>d = 25m</i>	<i>d = 50m</i>	<i>d = 75m</i>	<i>d = 100m</i>	<i>d = 25m</i>	<i>d = 50m</i>	<i>d = 75m</i>	<i>d = 100m</i>
BPSK-16WOFDM- QR	-52.9461	-35.2855	-25.2637	-17.2949	-30.4894	-29.2648	-24.1293	-17.09279
BPSK-16WOFDM- QMF	-55.9462	-38.2856	-28.2637	-20.2950	-30.5224	-29.8610	-26.2421	-19.9023

Table 5.4: RF (Analog) Energy Consumption and Total Energy Consumption for Virtual MIMO DGN Architecture

The time delays involved during the communication for True MIMO DGN system with QR and QMF detection processes are listed in Table 5.5 while that for Virtual MIMO model in Table 5.6. The processing time of QMF detection process is less as compared to QR detection process due to its lower computational intensity for both system models. The processing time (T_{pc_t}) is the most dominating factor in total time delay. Hence, BPSK-16WOFDM with QMF detection process is a suitable choice for energy and time constrained WSNs.

Modulation Type	T_{tr_t} secs/bit	T_{pr_t} secs/bit		T_{pc_t} secs/bit				T_{T-MIMO} secs/bit	
		$d = 10m$	$d = 100m$	T_{Mod}	T_{Dmod_t}	T_{Det_t}	T_{pc_t}	$d = 10m$	$d = 100m$
BPSK-16WOFDM-QR	1×10^{-6}	3.33×10^{-8}	3.33×10^{-7}	0.084075	1.4634×10^{-3}	1.66×10^{-3}	0.0872	0.0872	0.0872
BPSK-16WOFDM-QMF	1×10^{-6}	3.33×10^{-8}	3.33×10^{-7}	0.084075	1.4634×10^{-3}	1.60×10^{-3}	0.0871	0.0871	0.0871

Table 5.5: Total Time Delay for True MIMO DGN Architecture

Modulation Type	T_{tr} secs/bit	T_{pr} secs/bit		T_{pc} secs/bit				T_{V-MIMO} secs/bit	
		$d^L = 10m$	$d^L = 100m$	T_{Mod}	T_{Dmod}	T_{Det}	T_{pc}	$d^L = 10m$	$d^L = 100m$
BPSK-16WOFDM-QR	1.75×10^{-6}	3.33×10^{-8}	3.33×10^{-7}	0.084075	0.07682	0.0875	0.24840	0.24840	0.24840
BPSK-16WOFDM-QMF	1.75×10^{-6}	3.33×10^{-8}	3.33×10^{-7}	0.084075	0.07682	0.0840	0.2249	0.2249	0.2249

Table 5.6: Total Time Delay for Virtual MIMO DGN Architecture

The spectral efficiency (SE) versus energy efficiency (EE) graphs are shown in Figures 5.8 and 5.9 for both system models. The graphs are obtained at a transmission distance of 20m with BPSK-16WOFDM using QR and QMF detection processes. The four point on each graphs are obtained for BER values of 10^{-1} , 10^{-2} , 10^{-3} and 10^{-4} . It is observed that for a given SE, EE is

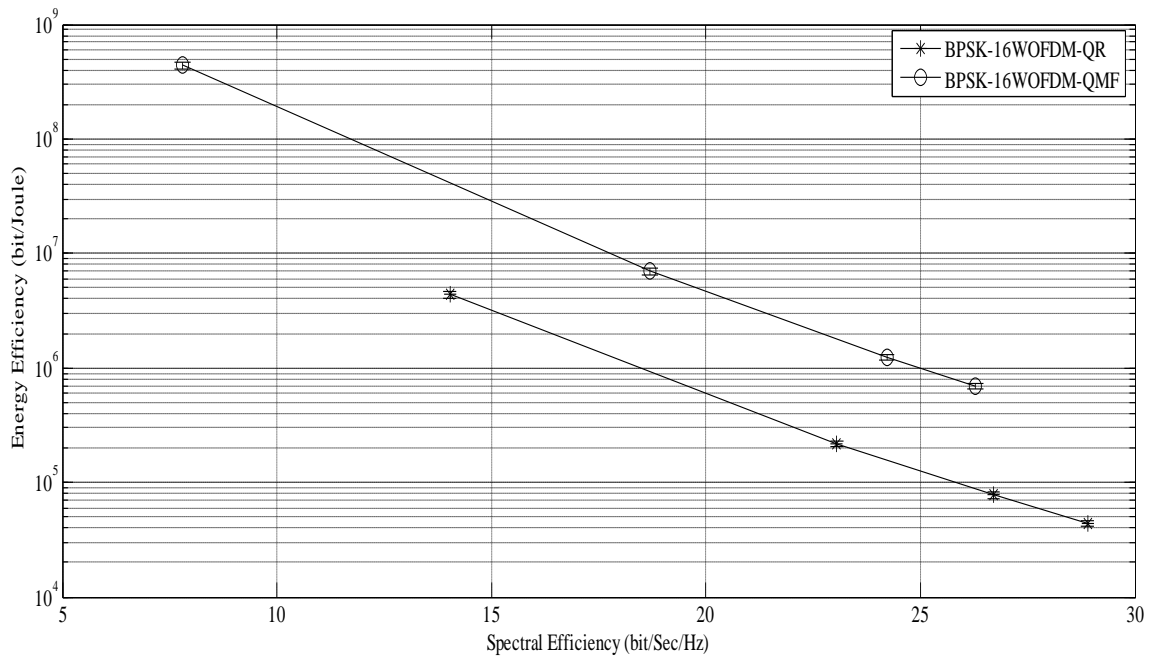


Figure 5.8: Energy Efficiency versus Spectral Efficiency over transmission distance of 20 m with True MIMO DGN using QR and QMF Bank detection process

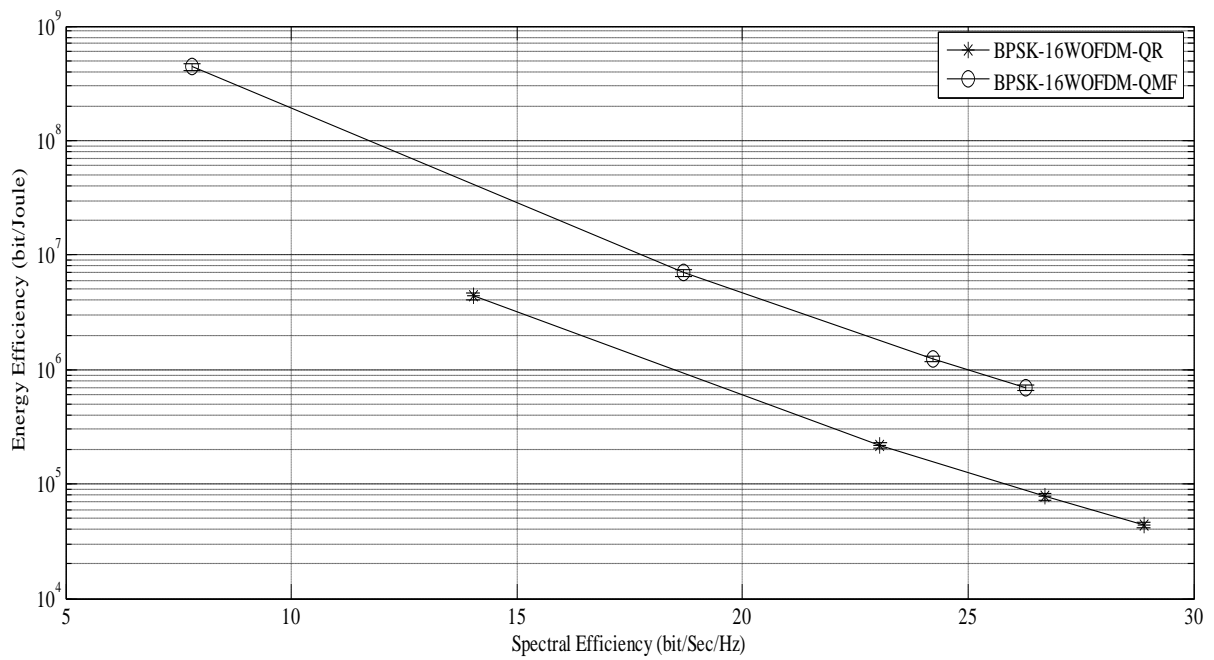


Figure 5.9: Energy Efficiency versus Spectral Efficiency BER over transmission distance of 20 m with Virtual MIMO DGN using QR and QMF Bank detection process

higher when QMF detection process is used. For example, for SE of 20 bit/Sec/Hz, the EE value with QMF detection process is 4.5×10^6 bit/Joule, while that with QR detection process is 5×10^5 bit/Joule.

Chapter 6

Phase Offset Compensation

As mentioned in Section 2.2, multiple antenna systems are considered spectrally efficient for a given bit error rate (BER) and transmission power [3]. For resource-limited wireless nodes, such as tiny battery-powered sensor nodes, it is often not possible to equip each node with multiple antennas. Thus, the concept of Virtual MIMO can be applied: a cluster of wireless nodes, each with single antenna can function as a Virtual MIMO node to realise the potential advantages of MIMO techniques [47, 86]. However, one of the major problems associated with Virtual MIMO systems is the phase offset of the signal, which can be due to different physical location of the nodes (inducing differences in signal time-of-arrival at the receiver) or phase error of the local oscillators [21].

The performance of FOFDM and WOFDM with AWGN channel in the presence of phase offset was explored in [63]. It was shown that both techniques are equally affected by the phase offset problem. Several techniques have been proposed in literature to compensate phase-offset of True MIMO systems with Fourier based OFDM (FOFDM) [89, 90]. New Wavelet bases were designed only with SISO AWGN channel in [91] with a trust region dogleg algorithm. In this technique, the distance among the carriers is increased to minimise the effect of phase offset. To best of our knowledge, this thesis investigated, for the first time, the performance of Virtual MIMO systems with BPSK-WOFDM and BPSK-FOFDM in the presence of phase-offset. It also proposed for the first time, the compensation of phase offset effect of Virtual MIMO system with

wavelet bases optimisation using GA. The wavelet bases of WOFDM demodulator are optimised to demodulate the signal as well as to compensate the effect of phase offset. In our proposed system model, DGN (receiver side node) is a more resourceful node. Hence, the wavelet bases should be optimised at receiver side DGN, not at transmitter side DSNs which are resource constrained. This approach of optimising the WOFDM demodulator's filter coefficients at DGN will also eliminate the need to replace phase offset local oscillators at DSNs, which can be difficult in certain deployments.

WOFDM is a multi-carrier energy efficient modulation technique, in which QMF bank structure is used to produce wavelet bases. This technique is generic in the sense that its filter bank coefficients can be optimised according to signal properties such as phase offset, frequency offset, and time asynchronism, unlike in FOFDM where the bases are static sine/cosine[64].

Wavelet bases can be optimised using genetic algorithm (GA) to enhance the overall system performance. GAs are appropriate for solving optimisation problems [92]. They are less complex and require less time to find optimal solutions for a given problem as compared to techniques such as particle swarm optimisation and simulated annealing. The Appendix section firstly overviews the concepts of GA and then discusses how it would be applied to obtain optimised wavelet bases for WOFDM.

6.1 System Model

Once again we consider a cluster of N_t data sensing nodes (DSNs) serving as one Virtual MIMO node at transmitter side, and a cluster of $N_r - 1$ data assisting nodes (DANs) along with one data gathering node (DGN) at receiver side to form a Virtual MIMO node as shown in Figure6.1. The

DGN, DANs, and DSNs are each equipped with a single antenna. All DSNs transmit their data simultaneously after modulation over a flat fading MIMO channel. By using symmetric structure, the orthonormal wavelets are given by:

$$f_k(n) = \prod_{p=1}^P \sqrt{2} t_{k,p} \left(\frac{n}{2^{p-1}} \right) \quad (6.1)$$

where \prod represents the convolution operation, P is the number of levels of this structure, $k \in \{0,1,2,3, \dots, 2^P - 1\}$, and $t_{k,p(n)} \in \{f_{l(n)}, f_{h(n)}\}$ is the filter impulse response corresponding to k_{th} sub-channel at p_{th} level. The $f_{l(n)}$ and $f_{h(n)}$ are impulse responses of the low-pass, and high-pass filters, respectively, at time n , for perfect reconstruction of QMF bank.

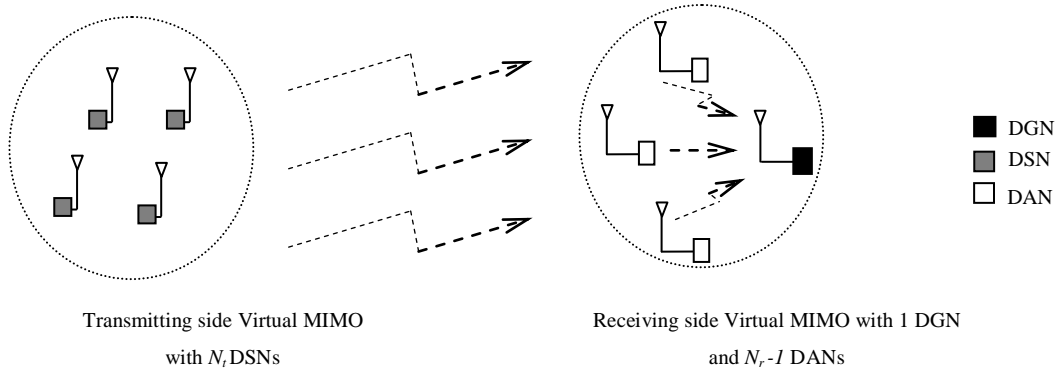


Figure 6.1: Communication between transmitting side and receiving side Virtual MIMO nodes.

The high pass filter can be derived from the low pass filter by the relation: $f_h(n) = (-1)^n f_l(U - 1 - n)$, where U is the length of the filter [66]. The output of WOFDM modulator can be given by:

$$s_i(n) = f_k(n) * x_k(n) \quad (6.2)$$

where $x_k(n)$ is the k_{th} sub-channel input of WOFDM modulator. At receiver side, all DANs and DGN itself receive the data, and then all DANs transmit their data to DGN using time-division-multiple access (TDMA) technique. The signal received through the j_{th} antenna at DGN can be represented as:

$$r_j(n) = \sum_{i=1}^{N_t} h_{ij}(n) * s_i(n) + \zeta_j(n) \quad (6.3)$$

where $h_{ij}(n)$ is the impulse response between j_{th} receiving and i_{th} transmitting antenna, $s_i(n)$ is the signal transmitted from i_{th} DSN, and $\zeta_j(n)$ is a Gaussian random noise variable with zero mean and some variance N_o .

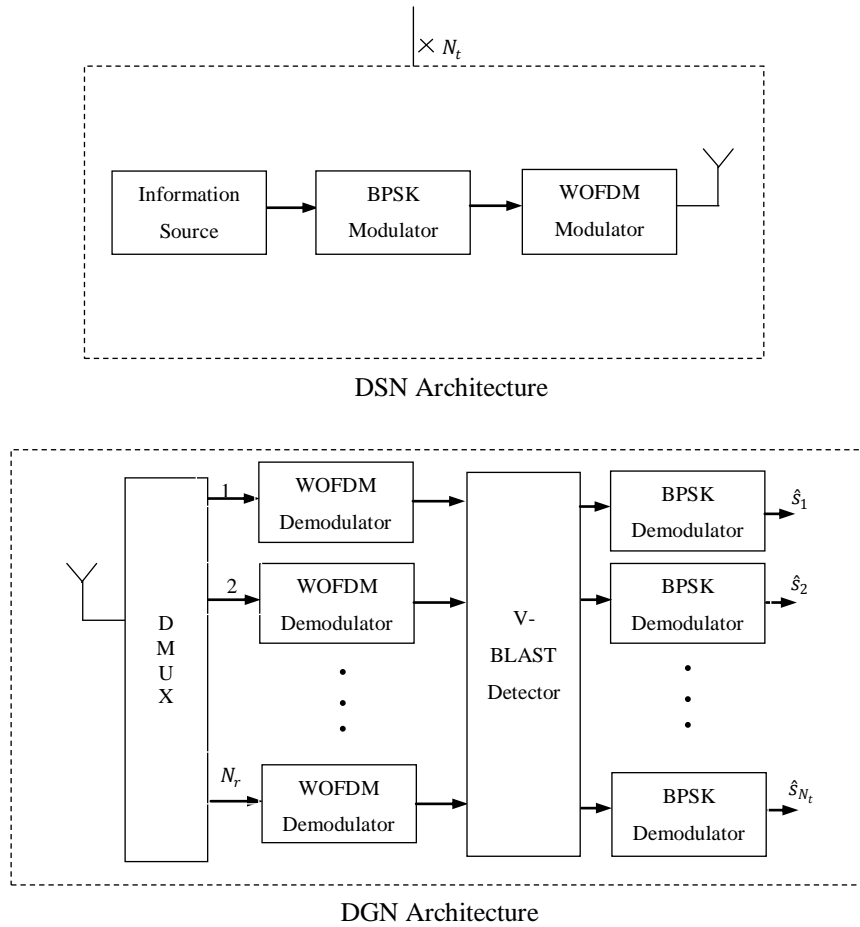


Figure 6.2: DSN and DGN architectures

The block diagram of DSN and DGN architectures with BPSK-WOFDM modulation technique is shown in Fig. 6.2. In each DSN, the information bit stream passes through BPSK modulator followed by WOFDM modulator. At DGN, the received signal vector is demultiplexed into N_r data streams, each passing through the WOFDM demodulator. Thereafter, the V-BLAST detector detects the signal, and is followed by BPSK demodulation to retrieve the transmitted signals.

6.2 Phase Offset Compensation

In the event of a phase offset at each receiver, the j_{th} received signal with phase offset becomes:

$$r_{j_{offset}}(n) = r_j(n)e^{j\phi(n)} \quad (6.4)$$

Similar to the assumption made in [93], the phase offset $\phi(n)$ is considered to be a normally distributed random variable known at DGN. This assumption is reasonable given the various techniques that exist for phase offset estimation, e.g. [94, 95]. After passing through WOFDM demodulator, the signal is given by:

$$\widetilde{r_{j_{offset}}}(n) = h_k(n) * r_{j_{offset}}(n) \quad (6.5)$$

where $h_k(n)$ represents orthonormal wavelet bases for WOFDM demodulator, generated using symmetric analysis side QMF bank as follows:

$$h_k(n) = \prod_{p=1}^P \frac{1}{\sqrt{2}} u_{k,p} \left(\frac{n}{2^{p-1}} \right) \quad (6.6)$$

The $u_{k,p(n)} \in \{g_{l(n)}, g_{h(n)}\}$ is the filter impulse response corresponding to k_{th} sub-channel at p_{th} level, while $g_{l(n)}$ and $g_{h(n)}$ are time reversals of $f_{l(n)}$, and $f_{h(n)}$, respectively [23].

The fitness function of GA is set to minimise the Euclidian distance between $\widetilde{r_{j_{offset}}}(n)$ and $r_j(n)$ such that:

$$\min \left\| \widetilde{r_{j_{offset}}}(n) - r_j(n) \right\| \quad (6.7)$$

$$\min \left\| h_k(n) * (r_j(n) e^{j\phi(n)}) - r_j(n) \right\| \quad (6.8)$$

The GA will determine the best filter coefficients for $g_{l(n)}$ and $g_{h(n)}$ to demodulate the signal as well as to minimise the effect of phase offset.

As mentioned in Appendix Section, GA solver is used to find the optimised filter coefficients. The default Uniform population creation function, Uniform selection function, and Scattered crossover function, are used since a preliminary test using other options in each of these functions did not show any notable difference in the results. For the Mutation function, the Adaptive Feasible Mutation option is selected as it can provide more consistent results than Gaussian or Uniform Mutation functions. This may be attributed to the advanced adaptive mechanism involved in this function.

In order to ensure convergence to a global minimum, the genetic algorithm needs to be run for a sufficiently long time [96]. A preliminary experiment was conducted which determined that 100

iterations of the algorithm provides a reasonable trade-off between speed of convergence and quality of the solutions, i.e. filter coefficients of the WOFDM demodulator.

6.3 Evaluation Results

Matlab/Simulink simulations are carried out to investigate the BER performance versus bit-energy to noise-spectral density ratio $\frac{E_b}{N_o}$ in the presence of phase offset for BPSK-16FOFDM, and BPSK-16WOFDM with four-level symmetric Haar filter coefficients, as shown in Figure 6.3, and 6.4, respectively using QR detection process. In addition, Figure 6.5 shows the results with QMF bank detection process. The phase offset is considered to have a mean value (μ) of either 0 or 2.356 rad, and variances (σ^2) of either 0 or 0.33 rad², similar to [91]. It should be noted that the phase offset is not the same for all DSNs. The normal distribution for the phase offset is determined in different DSN. For consistency with the evaluations conducted in Chapter 4 and 5, the distance between the transmitting and receiving clusters is similarly set to 20 m. Figure 6.4 also shows the performance of the system with optimised Wavelet bases in the presence of phase offset. QR decomposition detection algorithm [38] is used with V-BLAST architecture [22], and the system is comprised of 4 DTNs (as one transmitting Virtual MIMO node) and 1 DGN with 3 DANs (as one receiving Virtual-MIMO node), each equipped with a single antenna. All data points shown in the graph are plotted with their 95% confidence intervals.

It can be observed from Figures 6.3 and 6.4 that in the presence of phase offset with $\mu = 0$ rad and $\sigma^2 = 0.33$ rad², BPSK-16FOFDM and BPSK-16WOFDM with Haar wavelets based Virtual MIMO systems using QR detection process performs almost similarly to that of the case of no phase offset. However, for other values of phase offset, the system can perform very poorly, i.e. it

may become incapable of estimating the correct transmitted signal at DGN. Both modulation techniques also exhibited similar sensitivity to phase offset.

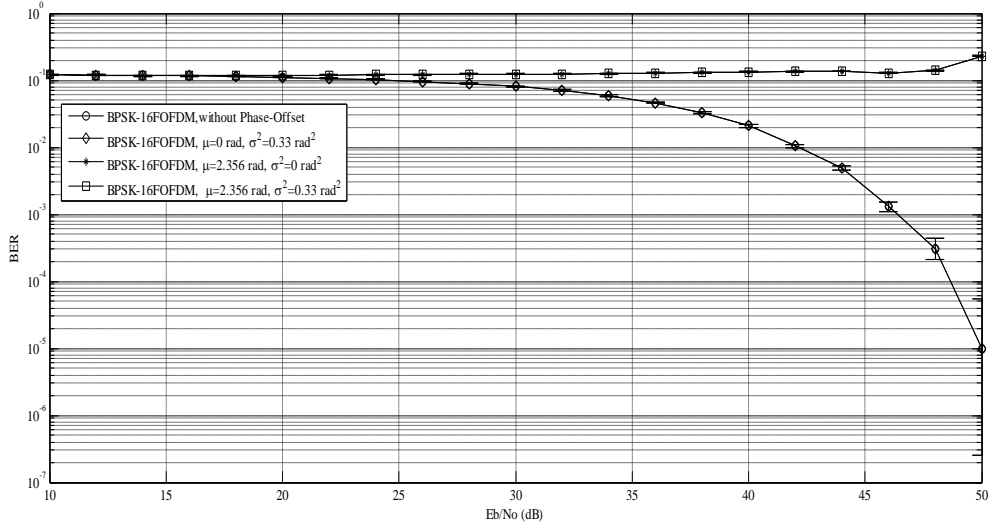


Figure 6.3: BER performance of BPSK-16FOFDM over transmission distance of $d = 20$ m in the presence of phase offset with Virtual MIMO DGN architecture using QR detection process

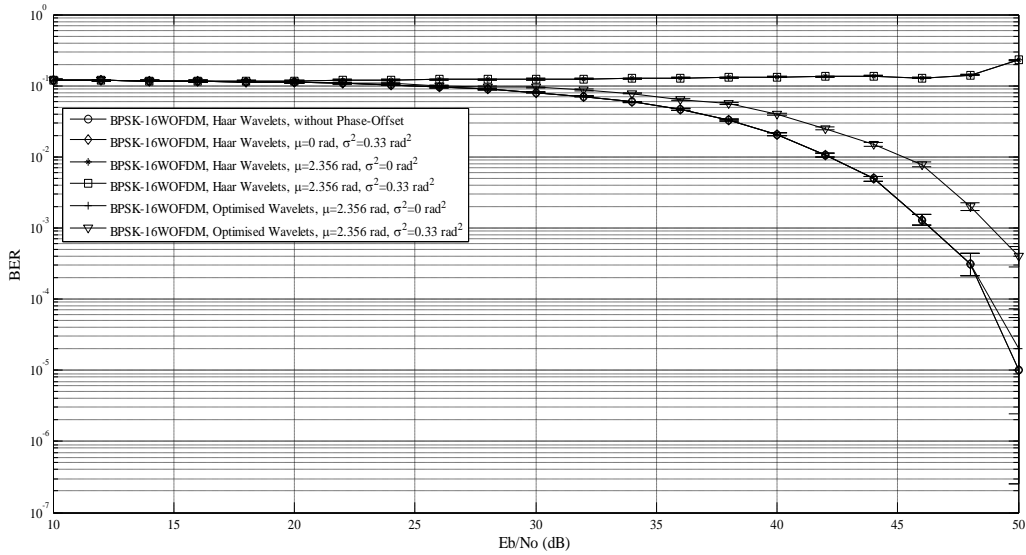


Figure 6.4: BER performance of BPSK-16WOFDM over transmission distance of $d = 20$ m with Haar and Optimised Wavelets in the presence of phase offset with Virtual MIMO DGN architecture using QR detection process

Figure 6.4 further shows the performance of the system with optimised Wavelets. The system performance with optimise Wavelets under a phase offset of $\mu = 2.356$ rad and $\sigma^2 = 0$ rad², can be

restored to the performance of a system without any phase offset. On the other hand, under a phase offset with the same mean but larger variance of $\sigma^2 = 0.33 \text{ rad}^2$, the system performance with optimised Wavelets is found to be significantly improved. This is because the Wavelet bases have been designed to minimise the phase-offset effect by decreasing the Euclidean distance between $\widetilde{r_{j_{offset}}}(n)$ and $r_j(n)$. The GA algorithm optimised the filter coefficients of QMF bank to obtain optimised Wavelet bases, which are used in WOFDM modulator and demodulator.

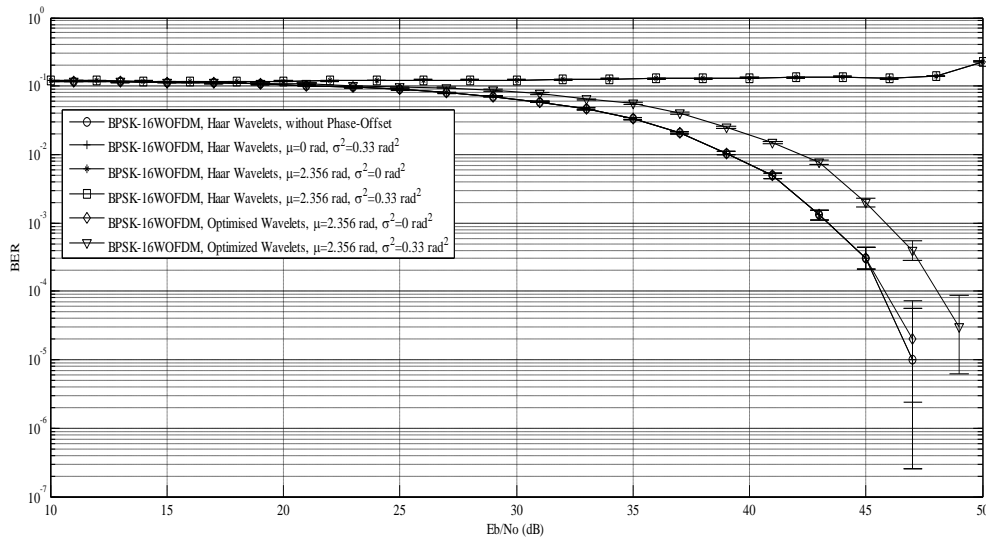
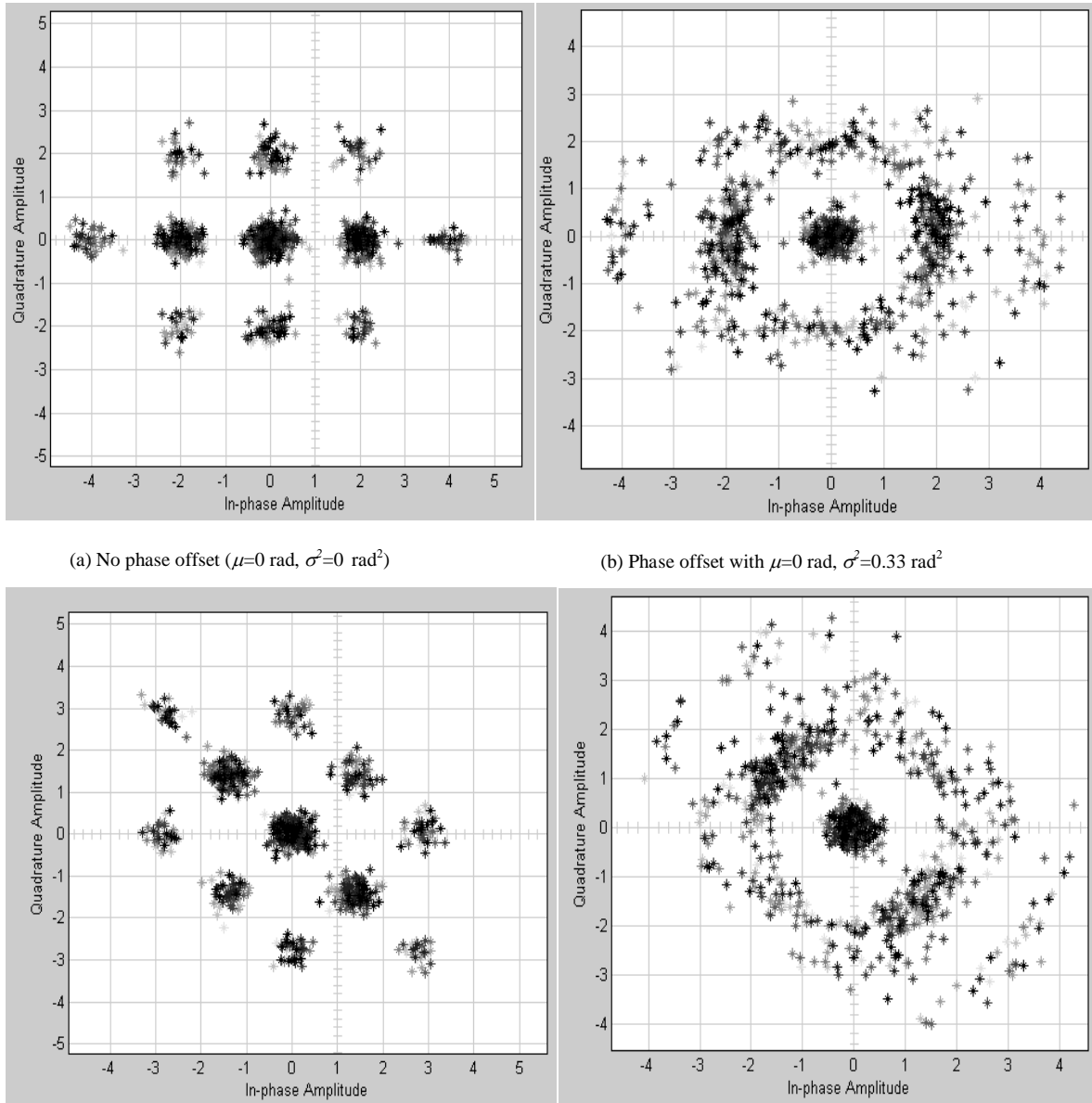


Figure 6.5: BER performance of BPSK-16WOFDM over transmission distance of $d = 20 \text{ m}$ with Haar and Optimised Wavelets in the presence of phase offset with Virtual MIMO DGN architecture using QMF bank detection process

Figure 6.5 shows the BER performance of BPSK-16WOFDM using Haar and optimised Wavelets with phase offset using QMF bank detection process. For $\text{BER} = 10^{-3}$, there is an improvement of almost 3 dB using Haar and optimised Wavelets for the phase offset values of $\mu = 0 \text{ rad}$, $\sigma^2 = 0.33 \text{ rad}^2$, $\mu = 2.356 \text{ rad}$, $\sigma^2 = 0 \text{ rad}^2$ and $\mu = 2.356 \text{ rad}$, $\sigma^2 = 0.33 \text{ rad}^2$. The system

performance is very poor for Haar Wavelets with phase offset values of $\mu = 2.356$ rad, $\sigma^2 = 0$ rad² and $\mu = 2.356$ rad, $\sigma^2 = 0.33$ rad².



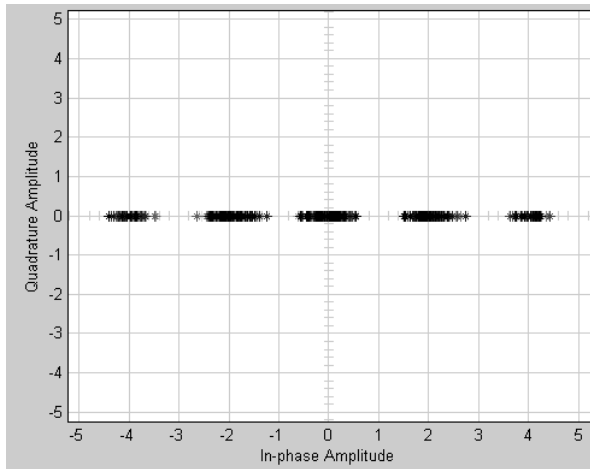
(a) No phase offset ($\mu=0$ rad, $\sigma^2=0$ rad²)

(b) Phase offset with $\mu=0$ rad, $\sigma^2=0.33$ rad²

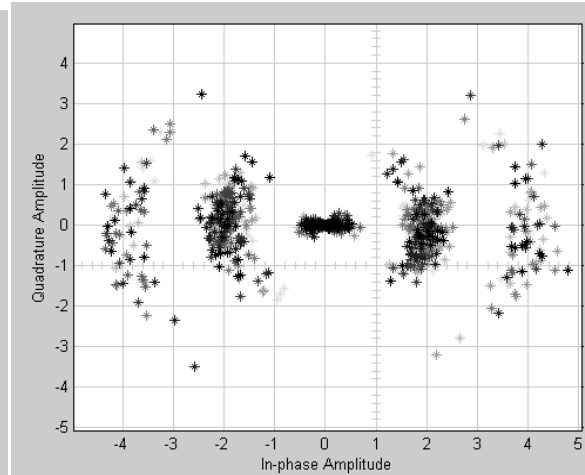
(c) Phase offset with $\mu=2.356$ rad, $\sigma^2=0$ rad²

(d) Phase offset with $\mu=2.356$ rad, $\sigma^2=0.33$ rad²

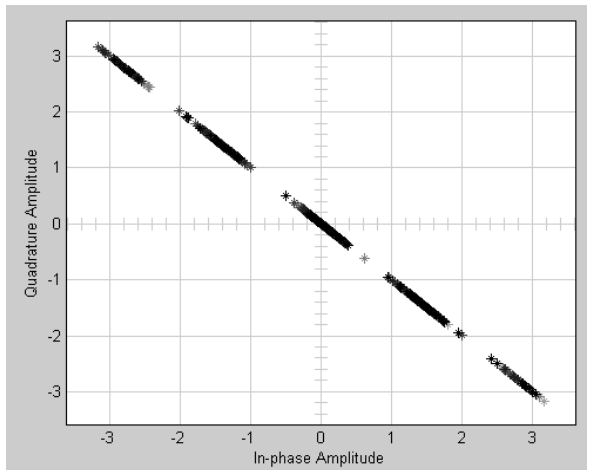
Figure 6.6: Polar Plots for BPSK-16FOFDM



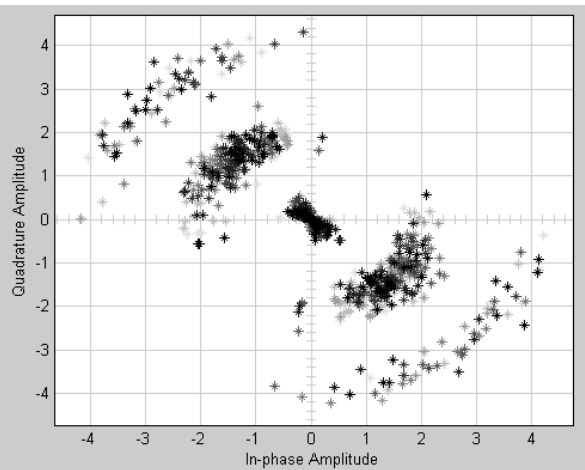
(a) Haar Wavelets, No phase offset ($\mu=0$ rad, $\sigma^2=0$ rad²)



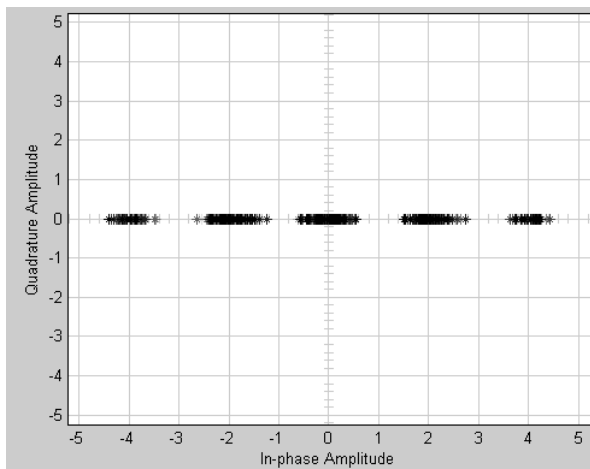
(b) Haar Wavelets, Phase offset with $\mu=0$ rad, $\sigma^2=0.33$ rad²



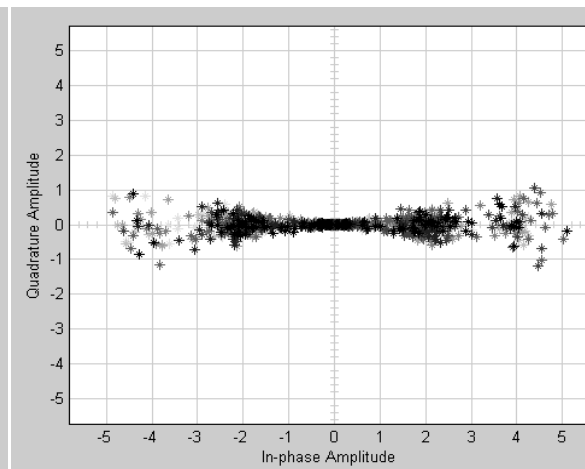
(c) Haar Wavelets, Phase offset with $\mu=2.356$ rad, $\sigma^2=0$ rad²



(d) Haar Wavelets, Phase offset with $\mu=2.356$ rad, $\sigma^2=0.33$ rad²



(e) Optimised Wavelets, Phase offset with $\mu=2.356$ rad, $\sigma^2=0$ rad²



(f) Optimised Wavelets, Phase offset with $\mu=2.356$ rad, $\sigma^2=0.33$ rad²

Figure 6.7. Polar Plots for BPSK-16WOFDM

Polar plots for BPSK-16FOFDM, and BPSK-16WOFDM with Haar and optimised Wavelets, are shown in Figure 6.6, and 6.7, respectively, under different levels of phase noise. Like BPSK-16FOFDM, BPSK-16WOFDM is sensitive to phase noise. For example, it can be seen that under phase offset of $\mu = 2.356$ rad and $\sigma^2 = 0$ rad², the entire signal constellation position changes significantly. Moreover, changing σ^2 value from 0 to 0.33 increases the scattering of data points in the polar plot. Thus, it is difficult to retrieve the transmitted signals at receiver side. However, due to generic nature of WOFDM modulation technique, the Wavelet bases can be optimised to cope with the effect of phase offset.

Chapter 7

7: Conclusion and Future Work

7.1 Conclusion

WSNs are finding their place in many real life applications due to the small size, low cost, and easy deployment of sensor nodes. WMSNs can further increase the scope of real life applications by using multimedia (audio and video) sensors along with conventional scalar sensors. To exploit the advantages of WMSNs, communication system architectures and techniques which are bandwidth efficient as well as energy efficient should be used.

MIMO systems are capable of achieving high data rate for a given BER and power. However, for nodes with resource and physical constraints such as WSN nodes, it is not possible to equip each node with multiple antennas. Thus, the concept of Virtual MIMO systems in which multiple nodes cooperate to form a VAA can be used. WOFDM is a promising multi-carrier modulation technique for enabling high data rate WSNs. In this thesis, the properties of WOFDM along with Virtual MIMO system architecture are explored to address the main issues of achieving high data rate and energy efficiency in WMSNs.

The performance of WMSNs with Virtual MIMO DSNs at transmitting side, and a DGN with either True or Virtual MIMO system architecture at receiver side has been analysed using different modulation techniques. For both system models, BPSK-16WOFDM is found to outperform other evaluated modulation techniques in terms of BER performance by up to 95%

for a given $\frac{E_b}{N_o}$, and in terms of energy efficiency by up to a factor of two for a transmission distance of 100 m. On the other hand, DQPSK based system performs better in terms of total time delay by up to almost 23%. Thus, DQPSK based system can be a suitable option for WMSN applications with less time delay requirement.

The BER performance and energy efficiency of both system models are generally similar. However, the system model with Virtual MIMO DGN performs better in terms of total time delay by up to 64%. Overall, BPSK-WOFDM when combined with Virtual MIMO system architecture shows great potential as a solution for WMSNs due to its simpler RF section, lower PAPR and better BER performance.

This thesis also explores the performance of system models with BPSK-16WOFDM using QMF bank detection process. Compared with a system using QR detection process, an improvement of 3 dB in BER and 47% in energy efficiency is achieved. There is also 9.5% reduction in total time delay. Using BPSK-WOFDM with QMF bank detection process can thus further make the system more energy efficient with less time delay.

This thesis further investigates the performance of Virtual MIMO system with BPSK-16FOFDM and BPSK-16WOFDM in the presence of phase offset. The results show that phase offset can significantly degrade the system BER performance with both modulation techniques. Even by increasing $\frac{E_b}{N_o}$ value, BER value is not decreasing. The system with BPSK-16WOFDM and phase offset ($\mu= 2.356$ rad, $\sigma^2= 0.33$ rad) at $\frac{E_b}{N_o}$ value of 50 dB, has its BER improved from 2×10^{-1} to 3×10^{-4} when Haar Wavelets are replaced with optimised Wavelet bases. This result also

highlights the ‘optimisability’ of BPSK-WOFDM due to the generic nature of WOFDM modulation technique in which its filter bank coefficients can be optimised according to system conditions, unlike FOFDM.

7.2 Future Work

A prototype WMSN platform can be designed and implemented with BPSK-16WOFDM. The system model performance can be checked with QR and QMF bank detection process. Phase offset compensation can also be demonstrated with this platform.

Different beam forming techniques which can steer the lobes and nulls to improve SNR and to cancel co-channel interference [33], can be explored with Virtual MIMO architecture using BPSK-WOFDM.

A Virtual multi-functional MIMO architecture which can provide multiplexing gain, diversity gain and beam-forming (SNR) gain altogether, can also be proposed and evaluated for WMSN. It is shown in [34] that True multi-functional MIMO architecture can better enhance the system performance as compared to conventional MIMO architecture. This is because in conventional MIMO systems, only SDM or STC and/or beam-forming techniques are used. Using SDM, STC, and beam-forming techniques can increase the data rate, improve BER performance, and improve SNR, respectively. In multi-functional MIMO architecture, SDM, STC and beam-forming techniques can be effectively integrated together to increase data rate, and improve BER performance and SNR, simultaneously.

Exact and approximate BER expressions for WOFDM can be derived for SISO system using different channel models. These expressions can be further modified for MIMO systems with different detection processes.

References

- [1] I. F. Akyildiz, W. Su, & Y. Sankarasubramaniam, “Wireless sensor networks: a survey,” *Computer Networks*, vol. 38, p. 393–422, 2002.
- [2] I. F. Akyildiz, T. Melodia, & K. R. Chawdury, “Wireless multimedia sensor networks: A survey,” *IEEE Wireless Comm.*, vol. 14, no. 6, pp. 32–39, Dec. 2007.
- [3] J. Mietzner *et al.*, “Multiple-Antenna Techniques for Wireless Communications – A Comprehensive Literature Survey,” *IEEE Comm. Surveys & Tutorials*, vol. 11, no. 2, pp. 87–105, 2009.
- [4] S. Cui, A. J. Goldsmith & A. Bahai, “Energy-Efficiency of MIMO and Cooperative MIMO Techniques in Sensor Networks”, *IEEE Journal on Selected Areas in Communication*, vol. 22, no. 6, pp. 1089–1098, 2004.
- [5] T. Hwang *et al.*, “OFDM and Its Wireless Applications: A Survey”, *IEEE Transactions on Vehicular Technology*, vol. 58, no. 4, pp. 1673–1694, 2009.
- [6] M. K. Lakshmanan, & H. Nikookar, “A Review of Wavelets for Digital Wireless Communication”, *Wireless Personal Communications*, vol. 37, no.3-4, pp. 387–420, 2006.
- [7] P. Vaidyanathan, “Quadrature mirror filter banks, M-band extensions and perfect-reconstruction techniques”, *IEEE ASSP Magazine*, vol.4, no.3, pp. 4–20, 1987.
- [8] http://en.wikipedia.org/wiki/IEEE_1901 [Accessed: January 28, 2013]
- [9] C. Buratti *et al.*, “An overview on Wireless Sensor Networks Technology and Evolution, *MPDI Sensors Journal*, vol. 9, pp. 6869–6896, 2009.
- [10] J. Yick, B. Mukherjee, & D. Ghosal, “Wireless sensor network survey”, *Computer Networks*, vol. 52, no. 12, pp. 2292–2330, 2008.
- [11] H. Guo, K.-S. Low, & H.-A. Nguyen, “Optimizing the Localization of a Wireless Sensor Network in Real Time Based on aLow-Cost Microcontroller”, *IEEE Transactions on Industrial Electronics*, vol. 58, no. 3, pp. 741–749,2011
- [12] M. Hefeeda, & M. Bagheri, “Forest Fire Modeling and Early Detectionusing Wireless Sensor Networks, *Ad Hoc & Sensor Wireless Networks*, vol. 7, pp. 169–224, 2009.
- [13] J. Lee, “RFMS: Real-time Flood Monitoring System with wireless sensor networks”, *IEEE International Conference on Mobile Adhoc and Sensor Systems (MASS)*, Atlanta, GA, USA, 2008.

- [14] W.-Y. Zhuang *et al.*, “Flood monitoring of distribution substation in low-lying areas using Wireless Sensor Network” *International Conference on System Science and Engineering*, Honolulu, HI, USA, 2011.
- [15] B. Weiss *et al.*, “A power-efficient wireless sensor network for continuously monitoring seismic vibrations, *Annual IEEE Communications Society Conference on Sensor, Mesh and Ad Hoc Communications and Networks*, Salt Lake City, UT, USA, 2011.
- [16] D. U. Ski, & M. Patan, “Sensor Network design for the estimation of Spatially distributed processes”, *International Journal of Applied mathematics & Computer Science*, vol. 20, no. 3, pp. 459–481, 2010.
- [17] C. Gezer, M. Niccoloni, & C. Buratti, “An IEEE 802.15.4/ZigBee based wireless sensor network for energy efficient buildings”, *IEEE Conference on Wireless and Mobile Computing*, Niagara Falls, Canada, 2010.
- [18] S. Misra, M. Reisslein, & G. Xue, “A Survey of Multimedia Streaming in Wireless Sensor Networks”, *IEEE Communication Surveys & Tutorial*, vol. 10, no. 4, pp. 18–39, 2008.
- [19] http://www2.ece.ohio-state.edu/~ekici/res_wmsn.html [Accessed: February 28, 2013]
- [20] I. F. Akyildiz, T. Melodia, & K. R. Chowdhury, “Wireless Multimedia Sensor Networks: Applications and Testbeds”, *Proceedings of IEEE*, vol. 96, no. 10, pp. 1588–1605, 2008.
- [21] H. Wang, & X. G. Xia, “Asynchronous cooperative communication systems: A survey on Signal Design”, *Science China Information Sciences*, vol. 54, no. 8, pp. 1547–1561, 2011.
- [22] P. W. Wolniansky *et al.*, “V-BLAST: An Architecture for Realizing Very High Data Rates Over the Rich-Scattering Wireless Channel”, *Proceedings of the International Symposium on Signals, Systems, and Electronics*, Pisa, Italy, September 1998.
- [23] Z. Rafique, N. D. Gohar, & M. J. Mughal, “Performance Comparison of OFDM and WOFDM based V-BLAST Wireless Systems”, *IEICE Transactions on Communication*, vol. E88-B, no. 5, 2005.
- [24] “RM Wavelet Based PHY Proposal for 802.16.3”, *IEEE802.16.3c-01/12*, Rainmaker Technologies, Inc.
- [25] G. Zelniker, & F. J. Taylor, “*Advanced Digital Signal Processing: Theory & Application*”, Marcel Dekker, Inc, New York, 1994.
- [26] Y. Chen, S. Zhang, & S. Xu, Fundamental Trade-offs on Green Wireless Networks, *IEEE Communications Magazine*, vol. 49, no. 6, pp. 30–37, 2011.

- [27] G. J. Foschini, “Layered Space-Time Architecture for Wireless Communication in a Fading Environment When Using Multi-Element Antennas”, *Bells Lab Technical Journal*, vol. 1, no. 2, pp. 41–59, 1996.
- [28] M. Sellathurai, & S. Haykin, “TURBO-BLAST for Wireless Communications: Theory and Experiments”, *IEEE Transaction on Signal Processing*, vol. 50, no. 10, pp. 2538–2546, 2002.
- [29] S. M. Alamouti, “A Simple Transmit Diversity Technique for Wireless Communications”, *IEEE Journal on Select Areas in Communications*, vol. 16, no. 8, pp. 1451–1458, 1998.
- [30] V. Tarokh, N. Seshadri, & A. R. Calderbank, “Space–Time Codes for High Data Rate Wireless Communication: Performance Criterion and Code Construction”, *IEEE Transactions on Information Theory*, vol. 44, no. 2, pp. 744–765, 1998.
- [31] V. Tarokh, N. Seshadri, & A. R. Calderbank, “Space–Time Block Codes for Orthogonal Designs”, *IEEE Transactions on Information Theory*, vol. 45, no. 5, pp. 1456–1467, 1999.
- [32] G. G. Raleigh, & J. M. Cioffi, “Spatio-Temporal Coding for Wireless Communication”, *IEEE Transactions on Communications*, vol. 46, no. 3, pp. 357–366, 1998.
- [33] L. C. Godara, “Application of antenna arrays to mobile communications– Part I: Performance improvement, feasibility, and system considerations; Part II: Beam-forming and direction-of-arrival considerations,” *Proceedings of IEEE*, vol. 85, no. 7/8, pp. 1031–1060, July/August 1997.
- [34] M. El-Hajjar, & L. Hanzo, “Multifunctional MIMO systems: A combined diversity and multiplexing design perspective”, *IEEE Wireless Communication Magazine*, vol. 17, no. 2, pp. 73–79, 2010.
- [35] C.-X. Wang *et al.*, “Cooperative MIMO Channel Models: A Survey”, *IEEE Communication Magazine*, pp. 80–87, 2010.
- [36] C. Z. W. H. Sweatman *et al.*, “A comparison of the MMSE detector and its BLAST versions for MIMO channels”, IEE seminar on MIMO communication systems from concept to implementation, pp. 1/19-6/19, December, 2001.
- [37] J. Benesty, A. Huang, & J. Chen, “ A fast recursive algorithm for optimum sequential signal detection in a BLAST system”, *IEEE Transaction on Signal Processing*, vol. 51, no. 7, pp. 1722–1730, 2003.

- [38] H. Lee *et al.*, “Signal detection using Log-Likelihood ratio based Sorting QR decomposition for V-BLAST Systems”, *IEEE Vehicular Technology Conference*, Dublin, Ireland, 22–27 April 2007.
- [39] C. Schlegel, & L. Perez, “Trellis and Turbo Coding”, *Wiley-IEEE Press Publication*, 2003.
- [40] L. Poo, “Space-Time Coding for Wireless Communications: A Survey”, *Report from Stanford University*, USA, 2002.
- [41] G. Leburn, J. Gao, & M. Faulkner, “MIMO transmission over a time-varying channel using SVD”, *IEEE Transaction on Communication*, vol.4, no. 2, pp. 757–764, 2005.
- [42] Q. Gao *et al.*, “Linear precoding and finite rate feedback design for V-BLAST Architecture”, *IEEE Transaction on Wireless Communication*, vol. 7, no. 12, pp. 4976–4986, 2008.
- [43] Z. Zhou, & G. B. Giannakis, “Optimal transmitter Eigen beam forming and Space-Time block coding based on channel mean feedback”, *IEEE Transaction on Signal Processing*, vol. 50, no. 10, pp. 2599–2613, 2002.
- [44] M. R. Bhatnagar, & A. Hjørungnes, “Improve interference cancellation scheme for two user detection of Alamouti code”, *IEEE Transaction on Signal Processing*, vol. 58, no. 8, pp. 4459–4465, 2010.
- [45] V. Tarokh, A. Naguib, N. Seshadri, A. R. Calderbank, “ Combined array processing and space-time coding”, *IEEE Transaction on Information Theory*, vol. 45, no.4, pp. 1121–1128, 1999.
- [46] G. Jongren, M. Skoglund, & B. Ottersten, “Combining ideal beamforming and orthogonal space-time block Coding”, *IEEE Transaction on Information Theory*, vol. 48, no.3, pp. 611–627, 2002.
- [47] S. K. Jayaweera, “V-BLAST-based virtual MIMO for distributed wireless sensor networks”, *IEEE Transaction on Communications*, vol. 55, no. 10, pp. 1867–1871, 2007.
- [48] G. K. Psaltopoulos, & A. Wittneben, “Nonlinear MIMO: Affordable MIMO Technology for Wireless Sensor Networks”, *IEEE Transactions on Wireless Communications*, vol. 9, no. 2, pp. 824–832, 2010.
- [49] D. Leang, & A. Kalis, “Smart Sensor DVB: sensor network development boards with smart antennas,” *International Conference on Communication, Circuits, System*, Chengdu, China, 27–29 June, 2004.

- [50] A. Kounoudes *et al.*, “Smart wireless sensor technology for continuous health monitoring of structures,” *International Conference on Bridge Maintenance, Safety, Management*, Philadelphia, 11–15 July, 2010.
- [51] E. P. Tsakalaki *et al.*, “Non Cooperative Space-Time Communication for Energy Efficiency in Sensor Networks”, *IEEE Transactions on Wireless Communications*, vol. 6, no. 1, pp. 48–54, 2012.
- [52] Y. Zhang, & S. Cheng, “A Novel Multicarrier Signal Transmission System Over Multipath Channel of Low-Voltage Power Line”, *IEEE Transaction on Power Delivery*, vol. 19, no. 4, pp. 1668–1672, 2004.
- [53] Z. Hanet *al.*, “Resource allocation for Multiuser Cooperative OFDM Networks: Who Helps Whom and How to Cooperate”, *IEEE Transactions on Vehicular Transactions*, vol. 58, no. 5, pp. 2378–2391, 2009.
- [54] H. Bolcskei, & A.J. Paulraj, “Space-frequency coded broadband OFDM systems”, *IEEE Conference on Wireless Communications and Networking (WCNC)*, vol. 1, pp. 1–6, Chicago, USA, 23–28 September, 2000.
- [55] Z. Liu, Y. Xin, & G. B. Giannakis, “Space-Time-Frequency Coded OFDM Over Frequency-Selective Fading Channels”, *IEEE Transaction on Signal Processing*, vol. 50, no. 10, pp. 2465–2476, 2002.
- [56] J. Flores, J. Sánchez, & H. Jafarkhani, “Quasi-Orthogonal Space-Time-Frequency Trellis Codes for Two Transmit Antennas”, *IEEE Transaction on Wireless Communication*, vol. 9, no. 7, pp. 2125–2129, 2010.
- [57] W. Yan, S. Sun, & Z. Lei, “A low complexity VBLAST OFDM detection algorithm for wireless LAN systems”, *IEEE Communications Letters*, vol. 8, no. 6, pp. 374–376, 2004.
- [58] W. Su, Z. Safar, & K. J. R. Liu, “Towards maximum achievable diversity in space, time and frequency: Performance analysis and code design”, *IEEE Transaction on Wireless Communications*, vol. 4, no. 4, pp. 1847–1857, 2005.
- [59] M. K. Gupta *et al.*, “Channel estimation for Wavelet based OFDM system”” *International Conference on Devices and Communication*, Mesra, India, 24–25 February, 2011.
- [60] A. R. Lindsey, “Wavelet Packet Modulation for Orthogonally Multiplexed Communication”, *IEEE Transactions on Signal Processing*, vol. 45, no. 5, pp. 1336–1339, 1997.

- [61] B.G. Negash, & H. Nikookar, “Wavelet Based OFDM for Wireless Channels”, 53rd *Vehicular Technology Conference*, Rhodes, Greece, 6–9 May, 2001.
- [62] A. Jamin, & P. Mahonen, “Wavelet Packet Modulation for Wireless Communications”, *Journal of Wireless Communication and Mobile Computing*, vol. 5, no. 21, pp. 1–18, 2005.
- [63] D. Karamehmedovic, M. K. Lakshmanan, & H. Nikookar, “Performance of Wavelet Packet Modulation and OFDM in the presence of carrier frequency and phase noise”, 1st *European Wireless Technology Conference*, Amsterdam, The Netherlands, 27–28 October, 2008.
- [64] D. Karamehmedovic, M.K. Lakshmanan, & H. Nikookar, “Optimal Wavelet Design for Multicarrier Modulation with Time Synchronization Error”, *IEEE Global Telecommunications Conference*, Honolulu, HI, USA, 30 November–4 December 2009.
- [65] M. K. Lakshmanan, & H. Nikookar, “Construction of Optimum Wavelet Packets for Multi-carrier based Spectrum Pooling Systems”, *Special Issue Wireless Personal Communications*, vol. 54, no. 1, pp. 95–121, 2010.
- [66] S. Gracias, & V. U. Reddy, “An Equalization Algorithm for Wavelet Packet Modulation”, *IEEE Transaction on Signal Processing*, vol. 46, no. 11, pp. 3082–3087, 1998.
- [67] M. Yasir *et al.*, “Performance Comparison of Wavelet based OFDM (WOFDM) V-BLAST MIMO Systems with Different Detection Algorithms”, *IEEE International Conference on Emerging Technologies*, Rawalpindi, Pakistan, 18–19 October 2008.
- [68] S. Cui, A. J. Goldsmith, & A. Bahai, “Energy-Constrained Modulation Optimization”, *IEEE Transactions on Wireless Communications*, vol. 4, no. 5, pp. 2349–2360, 2005.
- [69] J.-C. Chen, “Partial transmit sequences for Peak-to-Average Power Ratio Reduction of OFDM Signals with the Cross-entropy Method”, *IEEE Signal Processing Letters*, vol. 16, no. 6, pp. 545–548, 2009.
- [70] N. T. Le, S. D. Muruganthan, & A. B. Sesay, “An efficient PAPR reduction method for wavelet packet modulation schemes”, 69th *IEEE Vehicular Technology Conference*, Barcelona, Spain, 26–29 April 2009.
- [71] T. S. Rappaport, “Wireless Communications, Principle and Practice”, *Prentice Hall*, 2nd edition, 2001.

- [72] G. R. MacCartney *et al.*, “Path Loss Model for 5G millimeter Wave Propagation Channels in Urban Microcells”, *IEEE Global Communication Conference*, Atlanta, USA, 9–13 Dec. 2013.
- [73] S. Gurun, C. Krintz, & R. Wolski, “NWSLite: A General-purpose Nonparametric Prediction Utility for Embedded Systems”, *ACM Transaction on Embedded Computer System*, vol. 3, no. 7, pp. 1–36, 2008.
- [74] <http://www.memsic.com> [Accessed: 13 August 2012]
- [75] J. J. Ahmad, H. A. Khan, & S. A. Khayam, “Energy Efficient Video Compression for Wireless Sensor Networks”, *Annual Conference on Information Sciences & Systems*, Baltimore, MD, USA, 18–20 March 2009.
- [76] S. Haene, D. Perels, & A. Burg, “A Real-Time 4-Stream MIMO-OFDM Transceiver: System Design, FPGA Implementation, and Characterization”, *IEEE Transaction on Selected Areas in Communications*, vol. 26, no. 7, pp. 877–889, 2008.
- [77] M. A. Mamun, N. Nakaya, Y. Koi, and Y. Hagihara, "An Energy Efficient Cooperative Clustering Protocol for Heterogeneous Wireless Sensor Networks", *Journal of Computing*, vol. 3, no. 12, 2011.
- [78] Y. Liu, B.-C. Seet, and A. Al-Anbuky, "Virtual Brokers for Large-Scale Publish/Subscribe in Wireless Sensor Networks", *Proceedings of IEEE/IFIP 8th International Conference on Embedded and Ubiquitous Computing (EUC)*, Hong Kong SAR, China, December 2010.
- [79] J. D. Gupta, H. Suzuki, & K. Ziri-Castro, “Effect of Pedestrian Movement on MIMO-OFDM Channel Capacity in an Indoor Environment”, *IEEE Antennas and Wireless Propagation Letters*, vol. 8, pp. 682–685, 2009.
- [80] S. Simon, & A. Aragon-Zavala, “Antennas and Propagation for Wireless Communication Systems”, *Wiley*, 2nd edition, 2007.
- [81] V. K. Garg, “Wireless Communication and Networking”, Morgan Kaufmann, 2007.
- [82] G. Pekhteryev *et al.*, “Image transmission over IEEE 802.15.4 and ZigBee Networks”, *IEEE International Symposium on Circuits and Systems*, Kobe, Japan, 23–26 May, 2005.

- [83] W. Zha, & S. Blostein, “Modified Decorrelating Decision-Feedback Detection of BLAST Space-Time System”, *IEEE International Conference on Communication*, Helsinki, Finland, 28 April–2 May 2002.
- [84] P. Sharma, “Performance Analysis of Zero-Forcing Equaliser for ISI Reduction in Wireless Channels”, *IJERT*, vol. 1, no. 8, pp. 1–6, 2012.
- [85] B. Sklar, “Digital Communications: Fundamentals and Applications”, 2nd Edition, Prentice Hall, 2002.
- [86] A. Rafati, H. Lou, & C. Xiao, “Low Complexity Soft-Decision Feedback Turbo Equalisation for MIMO systems with Multilevel Modulations”, *IEEE Transaction on Vehicular Technology*, vol. 60, no. 7, pp. 3218–3227, 2011.
- [87] G. Ginis, & J. M. Cioffi, “On the Relation between V-BLAST and the GDFE”, *IEEE Communication Letters*, vol. 5, no. 9, pp. 364–366, 2001.
- [88] A. Hekkala *et al.*, “Analysis of and Compensation for Non-Ideal ROF Links in DAS”, *IEEE Wireless Communication Magazine*, vol. 17, no. 3, pp. 52–59, 2010.
- [89] K. Nikitopolous and A. Polydoros, “Decision-Directed Compensation of Phase Noise and Residual Frequency Offset in a Space-Time OFDM Receiver”, *IEEE Communications Letters*, vol. 8, no. 9, pp. 573–575, 2004.
- [90] P. Rabiei, W. Namgoong and N. Al-Dahir, “Reduced Complexity Joint Baseband Compensation of Phase Noise and I/Q Imbalance for MIMO-OFDM Systems”, *IEEE Transactions on Wireless Communications*, vol. 9, no. 11, pp. 3450–3460, 2010.
- [91] M. K. Lakshmanan, & H. Nikookar, “Construction of Optimal bases for Wavelet Packet Modulation under phase offset errors”, *3rd European Wireless Technology Conference*, Paris, France, 27–28 September, 2010.
- [92] A. E. Eiben, & J. E. Smith, “Introduction to Evolutionary Computing”, Springer-Verlag, Berlin, Heidelberg, 2003, 300 pages.
- [93] A. G. Armada, “Understanding the Effects of Phase Noise in OFDM”, *IEEE Transactions on Broadcasting*, vol. 7, no. 2, pp. 153–159, 2001.
- [94] H. Mehrpouyan *et al.*, “Joint Estimation of Channel and Oscillator Phase Noise in MIMO Systems”, *IEEE Transactions on Signal Processing*, vol. 60, no. 9, pp. 4790–4807, 2012.

- [95] A. A. Nasir *et al.*, “Phase Noise in MIMO System: Bayesian Cramer-Rao Bounds and Soft-Input”, *IEEE Transactions on Signal Processing*, vol. 61, no. 10, pp. 2675–2692, 2013.
- [96] D. Greenhalgh and S. Marshall, “Convergence Criteria for Genetic Algorithms”, *SIAM Journal on Computing*, vol. 30, no. 1, pp. 269-282, 2000.

Appendix

A.1 Genetic Algorithm

The fundamental GA process is illustrated in Figure 1. Initial population is created using a creation function with specified initial population size. The creation function is usually a random process. The fitness function then evaluates the population to find the best solution. If the best solution is found, the algorithm will end. Otherwise, the selection function will select the parents for the next generation. Different genetic operations (Mutation/Crossover) can be used. The mutation

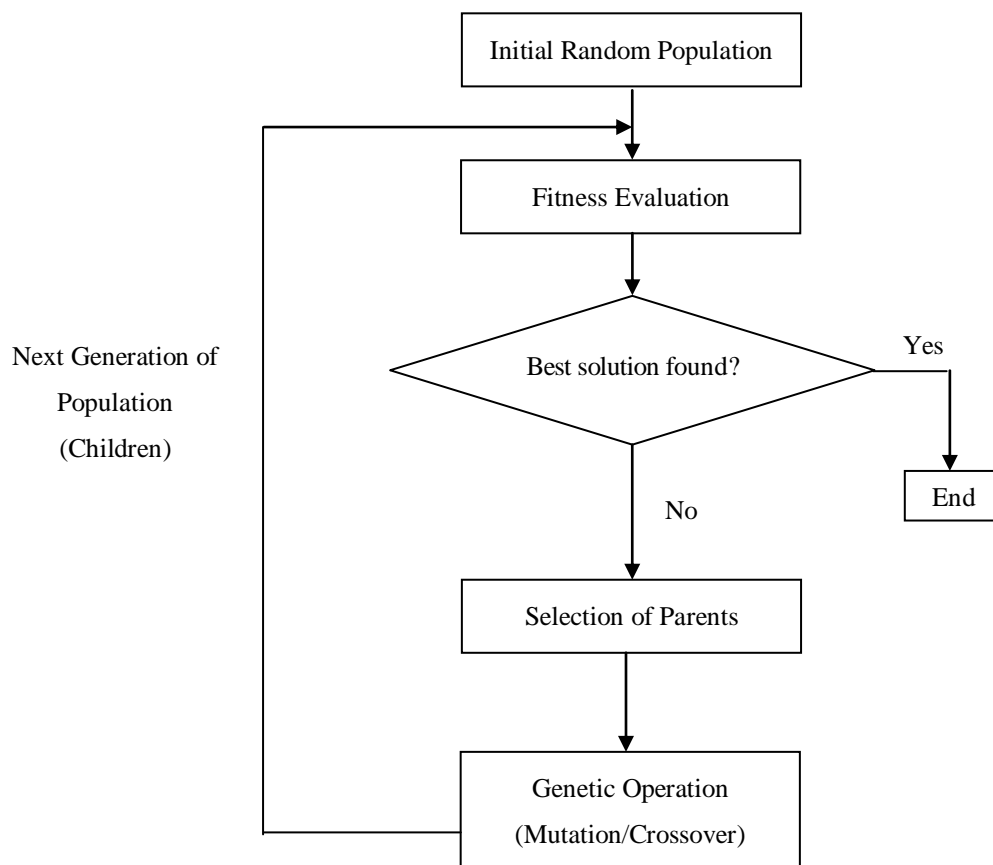


Figure A.1: GA process

function can make small random changes in an individual, and crossover function combines two individuals to form a new child for the next generation.

A.2 Genetic Algorithm Matlab Solver

The GA solver available in the Matlab optimisation tool box is used. The initial population can be created using Uniform or Feasible population creation functions. In the context of this work, the population consists of filter coefficient values of WOFDM demodulator. Uniform creation function creates initial population with uniform distribution while Feasible creation function creates initial population that is well dispersed within a feasible region defined by bound constraints. The fitness function for our given problem (Phase offset Compensation) is discussed in Section 6.2. Selection function selects parents for next generation. The available selection functions are Uniform, Stochastic Uniform, Roulette and Tournament. Uniform selection function selects parents using expectations and number of parents. In Stochastic Uniform function, each parent corresponds to a section of line with length proportional to its value. In Roulette selection function, parents are chosen by simulating a Roulette wheel, in which the area of the selection of the wheel corresponds to an individual and that area is proportional to an individual's expectations. Tournament selection function selects parent using tournament size players at random and select best individual out of the set to be a parent. The mutation functions available in the GA solver are Gaussian, Uniform and Adaptive Feasible. Gaussian mutation function adds a random number from Gaussian distribution while Uniform mutation function adds a random number from Uniform distribution to the parent vector. Adaptive Feasible mutation function randomly generates directions that are adaptive with respect to the last successful or unsuccessful generation. Scattered, Single-point, Two points, Heuristic and

Arithmetic crossover functions are available in GA solver. For example, Scattered crossover function creates a random crossover binary vector. For each value of '1' in the random vector, a gene is selected from the first parent. For each value of '0', a gene is selected from the second parent. The selected genes are then combined to form the child.